Heinrich Heine Universität Düsseldorf

Frequency metrology of HD^+ by ultra-high resolution rotational spectroscopy

Inaugural dissertation

for the attainment of the title of doctor

in the Faculty of Mathematics and Natural Sciences

at the Heinrich Heine University Düsseldorf

presented by

Soroosh Alighanbari

from Shiraz - Iran

Düsseldorf, October 2020

from the Institut für Experimentalphysik
at the Heinrich Heine University Düsseldorf

Published by permission of the

Faculty of Mathematics and Natural Sciences at
Heinrich Heine University Düsseldorf

Supervisor: Prof. Stephan Schiller, PhD
Date of the oral examination: 14.10.2020

Affidavit

I declare under oath that I have compiled my dissertation independently and without any undue assistance by third parties under consideration of the “Principles for the Safeguarding of Good Scientific Practice at Heinrich Heine University Düsseldorf”.

Düsseldorf, 14/10/2020

Soroosh Alighanbari

Contents

Abstract

The hydrogen molecular ion (MHI) is the simplest three-body bound quantum mechanical system, and therefore, it is an interesting system for advanced atomic and molecular physics studies. The rotational and vibrational energy levels of the MHIs depend on fundamental constants of atomic and nuclear physics, and measurement of transition frequencies between these levels enables determination of: Rydberg constant, electron-proton mass ratio, proton-deuteron mass ratio, proton radius, deuteron radius, and quadrupole moment of the deuteron. Spectroscopy of the MHIs is a complementary independent approach to link between hydrogen spectroscopy and mass spectrometry of fundamental particles. Besides, precision spectroscopy of the MHIs can be used to search for new physics beyond the standard model of particle physics, through search for a hypothetical fifth force between the nuclei.

The *ab initio* theory of the MHIs has been improved significantly in last two decades, through a highly precise calculation of the energies and wave functions of the three-body Schrödinger problem together with perturbation calculation of the relativistic and QED corrections. Currently, the uncertainty of the *ab initio* theory of the MHIs is 13×10^{-12} for rotational and 7.5×10^{-12} for vibrational transitions [1].

On the experimental side, laser spectroscopy of trapped and sympathetically cooled molecular ions enhanced spectroscopic resolution and accuracy. However, residual Doppler broadening in ion clusters limits the achievable resolution. Besides, unresolved hyperfine structure complicates interpretation of observed experimental transitions.

Here, we invented and demonstrated a novel approach that enables sub-Doppler rotational spectroscopy. The strong radial spatial confinement of molecular ions in a linear Paul trap, with excitation direction transverse to the axis of trap, provides the Lamb-Dicke regime. This approach enables Doppler-free spectroscopy of transitions with wavelength larger than motional amplitude of the molecular ions.

We measured the rotational transition of the HD^+ ions at 1.3 THz, where we achieved a fractional uncertainty of 1.3×10^{-11}. Compared to previous experiments using the sympathetic cooling method, we achieve a 100 times higher precision [2, 3]. This enormous improvement has led to the most accurate verification of the three-body quantum problem to date. Theory and experiment agree within an uncertainty of 5×10^{-11}, where the agreement is limited by the uncertainty of the fundamental constants, required to specify the

theoretical energy values. Our result confirms the most recent (CODATA 2018) values of the relevant fundamental constants.

The experimental results and theory also allow to precisely determine the combination of fundamental constants $R_\infty m_\mathrm{e}\left(1/m_\mathrm{p}+1/m_\mathrm{d}\right)$, with fractional uncertainty of 1.9×10^{-11}, which is in agreement but 2.4 times more precise than CODATA 2018. Alternatively, we use the Rydberg constant, electron mass, deuteron mass, and charge radii from CODATA 2018, and obtain the proton mass. We also deduce the value for the electric quadrupole moment of the deuteron by comparison of the theoretical and experimental spin averaged frequencies.

We used the experiment-theory agreement to set an upper limit on a hypothetical spin-independent fifth force between proton and deuteron, with a factor of 21 improvement compared to previous bounds from MHI spectroscopy.

1. Introduction

1.1. Limitations of the standard model of particle physics

Today's known physics asserts that everything in the universe is made of a few fundamental particles (6 quarks, 6 leptons, and 5 bosons), governed by four known fundamental forces (see Tab. 1.1). The Standard Model (SM) of particle physics is an overall framework to explain how these particles and three of the forces (namely the electromagnetic, the weak, and the strong forces) are related, and successfully predicts and describes numerous physical phenomena [4].

Table 1.1. The four types of interaction fields distinguished in nature, their mediating particles, and their spin.

Interaction field	Boson (force carrier)	Spin
Gravitational field	"Graviton" (postulated)	2
Weak field	W^+, W^-, Z bosons	1
Electromagnetic field	Photon	1
Strong field	Gluon	1

Although physicists have tested the SM extensively, it is still not considered as the ultimate description of nature, because it fails to explain a number of experimental observations. First, in spite of the recent discovery of the Higgs boson, which completes the SM's predicted list of particles, 95% of the Universe's content is still unknown (dark matter and dark energy). Second, the discovery of Higgs boson proves that its mass is much lighter than the Planck mass, while the SM suggests that the effective mass should be closer to the Planck scale. This problem, which is called the electroweak hierarchy problem, is essentially the question of why the electroweak interaction should be so much stronger than gravity. Third, the SM cannot explain the imbalance of the matter and antimatter in the aftermath of the big bang (baryogenesis problem). In addition, all attempts to unify the gravity and the other three fundamental interactions have been unsuccessful, because gravity cannot be described using quantum field theory. This gives a strong motivation to search for new particles and forces beyond the SM.

1.2. Search for new physics beyond the SM

The search for new physics beyond the SM is currently one of the most challenging and exciting research topics of fundamental physics. There are extensive searches, including, but not limited to: parity violation, searches for permanent electric dipole moments, tests of the combined charge conjugation, parity, and time-reversal (CPT) invariance theorem and Lorentz symmetry, searches for *spatio-temporal variation of fundamental constants*, *tests of quantum electrodynamics*, tests of general relativity and the equivalence principle, searches for dark matter, dark energy and *extra forces*, and tests of the spin-statistics theorem.

1.2.1. Exotic interactions

One way to find new physics beyond the SM is to try to detect the signature of new spin-dependent or spin-independent interactions in experiments. On one hand, one can search for exotic interactions where elementary particles possess new dipole couplings to known fields, e.g. search for electron's electric dipole moment [5]. On the other hand, there could be undiscovered fields generating dipole couplings between elementary particles. An interesting example of spin-independent hypothetical fields is a Yukawa-like modification of the gravitational interaction, which in literature is referred to as a fifth force. Since in quantum field theory each fundamental interaction is mediated through gauge bosons (see Tab. 1.1), any force can be phenomenologically parameterized by a Yukawa-like potential of the form

$$V_5(r) = \alpha m_1 m_2 \frac{e^{-r/\lambda}}{r}, \tag{1.1}$$

where the parameters α and λ characterize the strength and the range of the modified interaction, respectively, and m_1 and m_2 are masses of the interacting particles. Any experimental search for the fifth force will establish a limit or constraint for the coupling constant α given an assumed range range λ.

1.2.2. Spatio-temporal variation of fundamental constants

Number of theories beyond the SM and general relativity (GR) imply variation of fundamental constants in time and space. For instance, string theories propose existence of a massless, gauge neutral, scalar field that couples directly to matter. Detailed form of the scalar field couplings defines four-dimensional coupling constants, which are determined in terms of various dynamical fields. Consequently, these constants become dynamic fields. A detailed review of theories in which fundamental constants become dynamic fields can be found in reference [6].

Essentially, fundamental constants of physics can only be measured experimentally and they cannot be determined theoretically [7]. Since the currently known physics is described by the GR and the SM, the Newtonian constant of gravitation G of the GR must be combined with the SM parameters [6] to produce a list of fundamental physical constants. This list does not include any description of either dark matter or dark energy and contains no information about cosmological model of the universe. The Committee of Data for Science and Technology (CODATA) and the Particle Data Group (PDG) compile measurement techniques and analyze the relevant published data, and continuously revise and improve values of the fundamental constants [4, 8]. Recently, CODATA provided the values of fundamental constants based on all of the data available until 31 December 2018. The 2018 CODATA recommended values of the fundamental constants and their uncertainties are listed on the website of the National Institute of Standard and Technology[1] (NIST).

Among all of the fundamental constants, the dimensionless ones play a special role in the precision tests of physical laws. The units of measurement are arbitrary conventions that may eventually change in the future [9]. Basically, experimental measurements are comparison of two physical systems, one of which defines the unit of measurement and its fractional uncertainty sets the lower limit for any absolute values of all other measurements. For example, the SI unit of time is defined based on the transition between the two hyperfine levels of the ground state of the caesium (^{133}Cs) atom at rest at a temperature of 0 K. The fractional uncertainty of the Cs frequency standard is presently on the order of 10^{-16} [10]. Therefore, no absolute frequency measurement can be performed with fractional frequency uncertainty smaller than that of the best Cs frequency standard. Thus, the focus of modern physics studies of the variation of fundamental constants is on dimensionless constants, especially the fine-structure constant α and proton-electron mass ratio $m_{\mathrm{p}}/m_{\mathrm{e}}$.

1.3. Search for new physics with atoms and molecules

Besides direct search for new interactions and new particles with experiments at TeV energy scales, precision measurements using table top atomic, molecular, and optical (AMO) experiments can also be employed as a complimentary approach to search for physics beyond the SM. In the past thirty years, several extraordinary milestones have been achieved in experimental AMO physics Laser cooling, trapping, and quantum control of atoms and ions, together with invention of optical frequency comb allow for precise interrogation of ultracold atoms, ions, molecules, and molecular ions. These advances improve time and frequency metrology and measurement techniques, that can be used to probe the fundamental laws of physics.

[1] http://physics.nist.gov/constants

An early example of discovering new physics using precision AMO experiments dates back to the 1940s, when the observation of the Lamb shift [11] and the anomalous magnetic moment of the electron [12] spurred the development of quantum electrodynamics (QED).

Modern high precision spectroscopic achievements can be used to inspect minute effects expected from new physics, which opens the possibility of probing physics beyond the SM in tabletop experiments. For instance, the unprecedented precision of atomic clocks (fractional frequency uncertainty of 9.4×10^{-19} [13]) allows to search for possible time variations of α and m_p/m_e [14, 15]. Another example is search for time-reversal symmetry violation via search for permanent electric dipole moment (EDM) of a particle or nucleus, through high precision spectroscopy of molecules and molecular ions [5]. A permanent EDM would violate time-reversal symmetry and thus requires charge conjugation and parity violation in order to preserve the CPT symmetry, and is a signature of physics beyond the SM [16].

1.4. Probing QED with atoms and molecules

In addition to the search for new physics, AMO experiments can be used for precision tests of the existing theories. An early example of using AMO experiment to test the electroweak part of the SM is based on investigation of optical transitions of Cs atom to measure atomic parity non-conservation [17]. QED is the first relativistic quantum field theory [18], and it is the most precisely tested part of the SM [19]. Comparison of highly accurate theoretical QED predictions and high precision AMO experiments for simple atoms and molecules tests the accuracy of theory and is crucial for determination of fundamental constants.

Simple quantum systems are the best candidates for accurate tests of QED for bound states and determination of fundamental constants, since, strong field, strong coupling, nuclear structure, and hadronic effects are not significant. Especially, light hydrogen-like atoms (hydrogen, anti-hydrogen, deuterium, muonium, positronium) and simple three-body quantum systems (helium atom, lithium ion, helium-like ions, antiprotonic helium atom, **molecular hydrogen ions** (MHIs), antihydrogen molecular ion) are good candidates for test of QED theory of bound systems with high-order contributions.

An eminent application of high precision AMO experiment in probing QED and determination of fundamental constants is measurement of the proton radius r_p. Different approaches and quantum systems can be used to determine the proton radius. The CODATA 2014 determination of r_p is based on adjustment of the input parameters from the 1S$\rightarrow$2S and 2S$\rightarrow$nℓ (n = 2, 3, ...and ℓ = S, P, D) transition frequencies of hydrogen atom (which is indicated as the H world data point in Fig. 1.1), the electron-proton scattering [20], and the 2S$\rightarrow$2P transition frequency of muonic hydrogen μH [21] (an exotic form of hydrogen with a muon instead of an electron).

The proton radius deduced from measuring 2S→4P transition frequency of hydrogen atom [22] and, the muonic hydrogen transition frequency, and the recent Lamb shift measurement of hydrogen [23], disagrees with the CODATA 2014 value. However there is a good agreement between the CODATA 2014 and the 1S→3S transition frequency of hydrogen [24] (see Fig. 1.1). So far there is no explanation for this challenging conundrum,

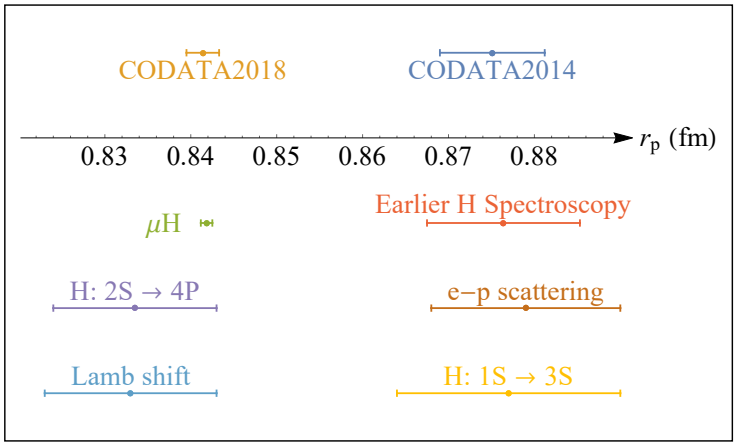

Figure 1.1. The proton radius measured by various techniques and CODATA adjusted values. The earlier H spectroscopy corresponds to 15 individual optical and microwave measurements of $1S \rightarrow 2S$ and $2S \rightarrow n\ell$ transitions (see adjustment 8, table XXIX of [8]).

thus perhaps high precision measurements of other bound quantum systems can shed light on this so called "proton radius puzzle".

1.5. Search for new physics and probing QED with molecular Hydrogen ions

The MHIs (H_2^+, HD^+, D_2^+, etc.) are composed of only two nuclei and an electron. Therefore, their energy level structure calculations are simpler than neutral hydrogen molecule H_2. Currently, the precision of these calculations lies at the high-10^{-12} level [1]. In chapter 2 an overview of *ab initio* calculations of energies of the MHIs are presented. The MHIs have rich energy spectra with hundreds of metastable levels in their ground electronic states.

The HD^+ ion is a heteronuclear MHI that consists of a proton, a deuteron and an electron. It has an electric dipole moment, which allows to induce electric dipole transitions between rotational and vibrational states. The vibrational and rotational transition fre-

quencies of HD^+, f_{vib} and f_{rot}, approximately scale as

$$f_{vib} \approx R_\infty \sqrt{m_e \left(\frac{1}{m_p} + \frac{1}{m_d}\right)}, \tag{1.2}$$

$$f_{rot} \approx R_\infty m_e \left(\frac{1}{m_p} + \frac{1}{m_d}\right), \tag{1.3}$$

where m_d is the deuteron mass.

The hyperfine structure adds a variety of dependence on the fundamental constants, like electric quadrupole moment of the deuteron Q_d. Moreover, radiative and relativistic corrections of the energy levels, which should be considered for high precision energy calculations, depend on nuclear properties such as proton and deuteron nuclear radii. Therefore, high precision spectroscopy of the HD^+ ion is a complementary approach, from which variety of fundamental constants are determined and the QED theory of three-body quantum systems are tested. Since transition frequencies depend on the Rydberg constant and the proton radius, measurements in HD^+ can help to decipher the proton radius puzzle.

Besides testing existing theories, HD^+ spectroscopy can provide constraints on new physical theories. HD^+ has been proposed as a suitable candidate for precise optical clock with achievable uncertainty of 10^{-18} [25], and its frequency metrology can be used to put new constraints on time variation of fundamental constants. Moreover, measuring the rovibrational transitions of HD^+ can put new constraints on the existence of hypothetical fifth force between proton and deuteron, through search for deviations between experiment and theory.

2. *ab initio* theory of the MHIs

2.1. Historical overview

In 1913 Niels Bohr published three seminal papers – now called the Bohr's trilogy – where he introduced a hypothesis to determine quantized energy orbits of bound electron. The Bohr's model for hydrogen atom is a pedagogically powerful tool to understand electronic structure in atoms, despite it is proved to be incompatible with modern quantum theory. In the third part of his trilogy, Bohr chose a simple model to explain and calculate hydrogen molecule's energy levels in its ground state. Since the Bohr's model suggests that the ground state of H_2 is paramagnetic, while it is weakly diamagnetic [26], soon its faulty concept revealed and it did not even gain a pedagogical application. However, it is the first theoretical effort to calculate electronic energy levels of molecules.

Having only one electron, the MHIs are simpler quantum systems compared to the hydrogen molecule. Wolfgang Pauli in his doctoral dissertation in 1922 used the Bohr-Sommerfeld quantization approach and found stable energy levels for H_2^+, but his calculations gave rise to incorrect equilibrium nuclear distance [27].

The first successful quantum mechanical treatment of H_2^+ was carried out by Øjvind Burrau in 1927 [28]. Burrau solved numerically the Schrödinger equation for an electron in the field of two protons, considering the clamped nuclei approximation. Fig. 2.1 shows Burrau's result for the ground electronic state of H_2^+ as a function of internuclear distance. Burrau's pioneering results can be arguably regarded as the birth of *ab initio* quantum chemistry.

Burrau's success motivated physicists in early 1930s to solve the Schrödinger equation analytically using power series expansion within the Born-Oppenheimer (BO) approximation. The BO approximation is based on treating the electronic and nuclear motions separately [29]. Jaffé in 1934 solved the problem for H_2^+ [30] and the heteronuclear diatomic molecular ions problem was solved in 1935 [31].

Instead of the BO approximation, where electronic and nuclear motions are separated into fast and slow components, one can consider that the electronic wave function depends on the nuclear coordinate, but motion of electron and nuclei are still separable. In this so-called *adiabatic approximation* [32], the electron's agility allows it to adjust to the motion of the nuclei almost instantly, hence the electronic wave function is independent

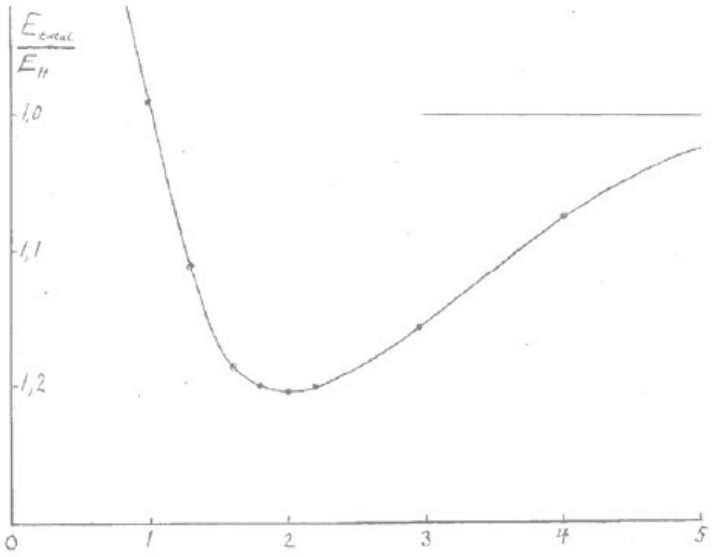

Figure 2.1. The stable ground electronic energy diagram of H_2^+ calculated by Ø. Burrau [28]. The horizontal axis is the internuclear distance in units of Bohr radius, and E_H is the Hartree energy.

of the nuclear momenta and mixing of the electronic states are neglected. This will allow to solve the full nonrelativistic Hamiltonian via expansion in terms of the BO solutions and to calculate a complete set of rovibrational wave functions for a given electronic state. Energies of rotational and vibrational levels and expectation values of internuclear separations in the adiabatic approximation for the MHIs are calculated in reference [33].

In order to achieve higher accuracy, nonadiabatic corrections should be considered. An important part of nonadiabatic correction is to consider that the nuclear momenta affect the electronic motion. In the heteronuclear MHIs, like HD^+, the nuclear mass asymmetry mixes the ground and the first excited electronic states. The nuclear mass asymmetry contributes to non-adiabatic correction of the Hamiltonian. Moss and Sadler proposed an approach to solve the Hamiltonian, including the symmetry breaking term, by transforming the Hamiltonian to a homonuclear case, e.g. H_2^+ [34].

More accurate calculations require variational method. Quantum variational calculation is a powerful method to solve approximately the Coulomb three-body bound state problem. Hylleraas in 1931 used variational method to calculate the eigenfunctions and eigenvalues of electronic terms in H_2^+ and H_2 [35]. Several decades later, Bishop and Cheung used variational method to accurately calculate the low-lying vibrational transition frequencies for the MHIs, taking into account radiative, relativistic, and nonadiabatic corrections [36]. In 1990s new calculations based on the variational exponential expansion with the basis sets up to 2200 functions appeared [37], which provided 18 significant digits for the ground state energy of the MHIs. Since then, theoretical calculation of transition frequencies of the MHIs reached an unprecedented accuracy. Tab. 2.1 shows progress of

theoretical solution of the nonrelativistic problem for the fundamental rotational transition frequency of HD^+, over the last five decades.

Table 2.1. Progress of theoretical nonrelativistic rotational frequency in atomic units ($a.u.$) examined in this thesis [38]. The penultimate frequency in the list is calculated using CODATA 2014 values of fundamental constants, but the last frequency is calculated using the updated values of CODATA 2018.

Year	Method	$f_{\mathrm{rot}}^{(\mathrm{theor})}(\times 10^{-4}\, a.u.)$	Reference
1967	Multichannel BO	1.997 5	[39]
1977	Adiabatic	1.998 508	[36]
1977	Variational	1.998 39	[36]
1989	Adiabatic	1.998 5	[34]
1989	Transformed H, adiabatic	1.998 5	[34]
1989	Variational Σ	1.998 5	[40]
1989	Variational Σ, Π	1.998 4	[40]
1990	Transformed H, scattering	1.998 41	[41]
1999	Variational	1.998 404 167	[42]
1999	Transformed H, scattering	1.998 404 167	[42]
2005	Variational	1.998 404 167 20	[43]
2006	Variational	1.998 404 166 8	[44]
2006	Variational	1.998 404 166 8	[45]
2014	Variational	1.998 404 166 806 9	[46]
2018	Variational	1.998 404 166 825 29	chapter 4
2020	Variational	1.998 404 167 149 47	chapter 5

2.2. Overview of QED theory of the MHIs

Details of *ab initio* theory of the MHIs are beyond the context of this dissertation, hence only a brief overview of the topic is presented here. The total energy of a MHI's state can be written as

$$E = E_{\mathrm{nr}} + E_{\mathrm{rel}} + E_{\mathrm{QED}} + E_{\mathrm{spin}}, \tag{2.1}$$

where E_{nr} is the nonrelativistic energy and E_{rel}, E_{QED}, and E_{spin} are relativistic, QED, and spin interaction corrections, respectively.

E_{nr} can be calculated by solving the Schrödinger equation for a three-body system with Coulomb interaction. Solutions of the nonrelativistic Hamiltonian determine the electronic and rovibrational energies, where the rovibrational states are labeled with the vibrational quantum number and the quantum number of the total orbital angular momentum as (v, L) (see Fig. 2.2).

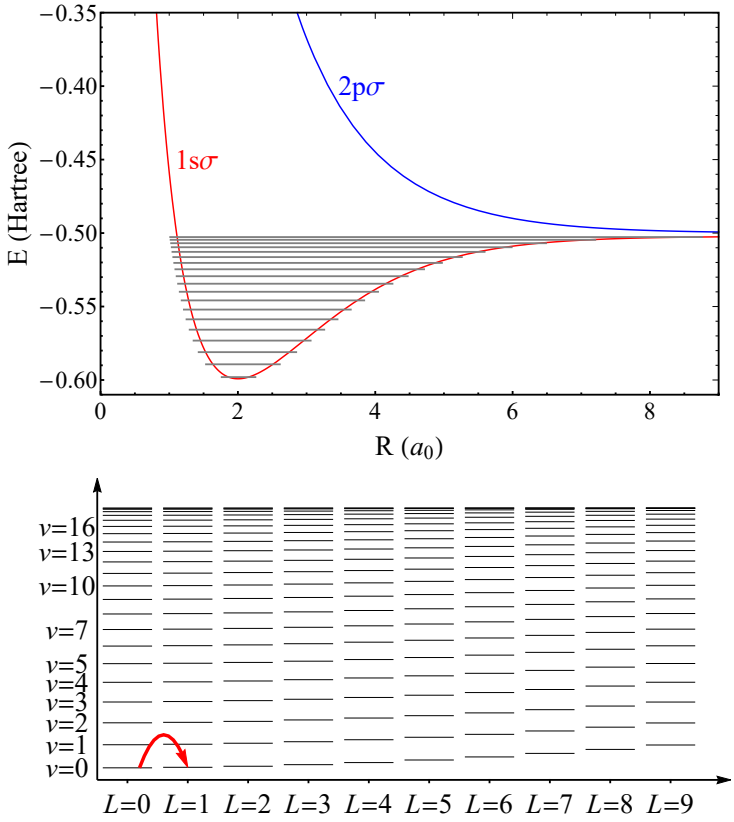

Figure 2.2. Energy levels of the HD^+ molecular ion. Top: the ground ($1s\sigma$) and first excited ($2p\sigma$) electronic states. The horizontal lines are the vibrational levels in the ground electronic state. Bottom: all of the vibrational states and first nine rotational states in the $1s\sigma$ level. The energy values of the rovibrational states are taken from [47]. The curved red arrow indicates the rotational transition (with energy difference of ∼1.3 THz) investigated in this thesis.

According to the theory of nonrelativistic QED (NRQED) [48], relativistic and QED energy corrections for a bound state problem can be expressed in powers of the fine structure constant α. For high-precision theoretical calculations and to determine the fundamental constants, relativistic and radiative corrections up to $O(\alpha^7)$ are considered. These corrections are evaluated using the nonrelativistic Rayleigh-Schrödinger perturbation theory starting from the nonrelativistic wavefunction as the unperturbed zero-order state.

Different relativistic and radiative correction terms corresponding to different orders of α are considered and evaluated for the MHIs. The corrections considered are:

- Leading-order relativistic corrections of order $R_\infty\alpha^2$ [1]:
  - The major contribution is the relativistic correction for the bound electron.
  - Retardation term, due to the finite nuclear masses (also called recoil corrections).

  - Kinetic energy term, due to dependence of the relativistic mass on velocity.
  - Nuclear-size correction, due to finite size of the nuclei.
- Leading-order radiative corrections of order $R_\infty\alpha^3$ [1]:
  - One-loop self-energy.
  - Anomalous magnetic moment.
  - One-loop vacuum polarization.
  - Transverse photon exchange.
- $R_\infty\alpha^4$ order corrections [49]:
  - Two-loop self-energy.
  - Two-loop vacuum polarization.
- $R_\infty\alpha^5$ order corrections[49]:
  - Wichman-Kroll contribution.
  - Three-loop Feynman contribution.

Theoretical evaluation of the rovibrational energies for the MHIs reached accuracy of 13 ppt for rotational and 7.5 ppt for vibrational transitions [1]. These energies are evaluated for spin-independent or more precisely spin-averaged frequencies. Tab. 2 of chapter 5 shows the theoretical spin-averaged transition frequency of the fundamental rotational transition of HD^+, and contributions of relativistic and radiative corrections.

Precise comparison of theory and experiment requires an accurate calculation of hyperfine structure of rovibrational states. The Breit-Pauli Hamiltonian describes interaction of spins of the particles with the spatial wave function of a state via orbital angular momentum operator. The Hamiltonian includes the electron-nuclear spin-spin interactions, the electron-spin-rotation interactions, the nuclear spin-orbit couplings and the deuteron electric quadrupole interaction. The effective Hamiltonian, after averaging over spatial degrees of freedom, can be written as [50]

$$\begin{aligned} H_{\text{eff}}^{\text{hfs}} =& \mathcal{E}_1 \left(\mathbf{L}\cdot\mathbf{S}_\text{e}\right) + \mathcal{E}_2 \left(\mathbf{L}\cdot\mathbf{S}_\text{p}\right) + \mathcal{E}_3 \left(\mathbf{L}\cdot\mathbf{S}_\text{d}\right) + \mathcal{E}_4 \left(\mathbf{S}_\text{p}\cdot\mathbf{S}_\text{e}\right) + \mathcal{E}_5 \left(\mathbf{S}_\text{d}\cdot\mathbf{S}_\text{e}\right) \\ &+ \mathcal{E}_6 \left\{2\mathbf{L}^2 \left(\mathbf{S}_\text{p}\cdot\mathbf{S}_\text{e}\right) - 3\left[\left(\mathbf{L}\cdot\mathbf{S}_\text{p}\right)\left(\mathbf{L}\cdot\mathbf{S}_\text{e}\right) + \left(\mathbf{L}\cdot\mathbf{S}_\text{e}\right)\left(\mathbf{L}\cdot\mathbf{S}_\text{p}\right)\right]\right\} \\ &+ \mathcal{E}_7 \left\{2\mathbf{L}^2 \left(\mathbf{S}_\text{d}\cdot\mathbf{S}_\text{e}\right) - 3\left[\left(\mathbf{L}\cdot\mathbf{S}_\text{d}\right)\left(\mathbf{L}\cdot\mathbf{S}_\text{e}\right) + \left(\mathbf{L}\cdot\mathbf{S}_\text{e}\right)\left(\mathbf{L}\cdot\mathbf{S}_\text{d}\right)\right]\right\} \\ &+ \mathcal{E}_8 \left\{2\mathbf{L}^2 \left(\mathbf{S}_\text{p}\cdot\mathbf{S}_\text{d}\right) - 3\left[\left(\mathbf{L}\cdot\mathbf{S}_\text{p}\right)\left(\mathbf{L}\cdot\mathbf{S}_\text{d}\right) + \left(\mathbf{L}\cdot\mathbf{S}_\text{d}\right)\left(\mathbf{L}\cdot\mathbf{S}_\text{p}\right)\right]\right\} \\ &+ \mathcal{E}_9 \left\{\mathbf{L}^2\mathbf{S}_\text{d}^2 - \frac{3}{2}\left(\mathbf{L}\cdot\mathbf{S}_\text{d}\right) - 3\left(\mathbf{L}\cdot\mathbf{S}_\text{d}\right)^2\right\}, \end{aligned} \tag{2.2}$$

where $\mathcal{E}_i$'s are the spin Hamiltonian coefficients. $\mathbf{L}$ is the orbital angular momentum, and $\mathbf{S}_\mathrm{d}$, $\mathbf{S}_\mathrm{p}$, and $\mathbf{S}_\mathrm{e}$ are the spins of deuteron, proton, and electron, respectively. Note that, for vibrational states of zero orbital angular momentum ($L = 0$), all the terms in equation 2.2, except electron-nucleus spin-spin interactions (terms with $\mathcal{E}_4$ and $\mathcal{E}_5$ coefficients), vanish. Extended Data Tab. 1 of of chapter 5 shows spin Hamiltonian coefficients for the transitions investigated in our experiment. Since the strongest coupling is due to the $\mathcal{E}_4 \left(\mathbf{S}_\mathrm{p} \cdot \mathbf{S}_\mathrm{e}\right)$ interaction, the coupling scheme of angular momentum operators is

$$\mathbf{G}_1 = \mathbf{S}_\mathrm{p} + \mathbf{S}_\mathrm{e}, \qquad \mathbf{G}_2 = \mathbf{G}_1 + \mathbf{S}_\mathrm{d}, \qquad \mathbf{F} = \mathbf{L} + \mathbf{G}_2, \tag{2.3}$$

and an appropriate basis set are the vectors of the so-called "pure" states labeled by $|v, L, G_1, G_2, F\rangle$. Fig. 1 of chapter 5 shows the energy diagram of the hyperfine states for $|0, 0, G_1, G_2, F\rangle$ and $|0, 1, G_1, G_2, F\rangle$ levels. Note that a hyperfine state in chapter 4 is labled with $|v, L, F, S, J\rangle$, where G_1, G_2, and F are replaced with F, S, and J, respectively.

When the magnetic field is zero $\mathbf{F}^2$ commutes with $H_\mathrm{eff}^\mathrm{hfs}$, which means each hyperfine state has degenerate Zeeman components. Projection of the angular momentum $\mathbf{F}$ on the quantization axis m_F is a good quantum number to indicate these Zeeman components $|v, L, G_1, G_2, F, m_F\rangle$. Presence of magnetic field lifts the degeneracy and splits the Zeeman components. In addition, time-dependent magnetic fields caused by alternating currents in the ion trap can cause an AC Zeeman shift [51]. Precise comparison of theory and experiment requires careful consideration of the Zeeman shifts. The interaction potential of HD^+ in an external magnetic field $\mathbf{B}$ has the form [52]

$$V^\mathrm{mag} = -\mathbf{M} \cdot \mathbf{B}, \qquad \mathbf{M} = \sum_i \frac{eZ_i}{2m_i c} \left(\mathbf{L}_i + \frac{\mu_i}{S_i}\mathbf{S}_i\right), \tag{2.4}$$

where the summation is over the constituents of HD^+ (i = e, p, d), Z_i is the electric charge of particle i in unit of e, m_i is its mass, μ_i is the magnetic moment in unit of $e\hbar/2m_i c$, and S_i is the spin. For small external magnetic fields, V^mag contains only the leading-order terms, and corrections of relative order $O(\alpha^2)$ and higher are ignored. By averaging over spatial degrees of freedom the total Hamiltonian is

$$H_\mathrm{eff}^\mathrm{total} = H_\mathrm{eff}^\mathrm{hfs} + \mathcal{E}_{10} \left(\mathbf{L} \cdot \mathbf{B}\right) + \mathcal{E}_{11} \left(\mathbf{S}_\mathrm{p} \cdot \mathbf{B}\right) + \mathcal{E}_{12} \left(\mathbf{S}_\mathrm{d} \cdot \mathbf{B}\right) + \mathcal{E}_{13} \left(\mathbf{S}_\mathrm{e} \cdot \mathbf{B}\right). \tag{2.5}$$

The values of $\mathcal{E}_{10}$ can be calculated from the nonrelativistic wave function, while $\mathcal{E}_{11}$, $\mathcal{E}_{12}$, and $\mathcal{E}_{13}$ are obtained from the fundamental constants [52]. Fig. 3 of chapter 4 shows the Zeeman splitting of the $|0, 0, 1, 2, 3\rangle$ and $|0, 1, 1, 2, 2\rangle$ states at 0.04 mT.

Besides the Zeeman effect, the DC and AC Stark effects should be considered in spectroscopy of the MHIs. Therefore, analysis of the DC Stark effect, light shift due to electric field of lasers, and the black body radiation shift, is essential for high precision measurements. Theoretical analyses of these systematic shifts requires accurate calculations of

static and dynamic polarizabilities of the MHIs. Polarizabilities of HD^+, considering the hyperfine structure, are calculated, and therefrom the DC Stark shift and black body radiation shift are evaluated [53]. Since the precise frequency dependence of the polarizability is considered, the results can be used to find the light shift induced by the electric fields of the lasers.

3. High precision spectroscopy of the MHIs

3.1. Progress of precision spectroscopy of the MHIs

First indirect determination of vibrational frequencies of H_2^+, via measurement of heat of dissociation, was carried out by R. T. Birge in 1927 [54]. Direct experimental spectroscopy of rovibrational and hyperfine structures of the MHIs took place in 1960s. One of the first notable achievements in spectroscopy of H_2^+ was performed in Hans G. Dehmelt's laboratory at the University of Washington, where radio-frequency (RF) spectroscopy between the Zeeman sublevels of different hyperfine states were performed [55]. In this experiment, the hydrogen molecule was ionized by electron bombardment and trapped in an RF quadrupole trap and detection was based on dissociation of the molecular ions. K. B. Jefferts for the first time in 1969 observed the complete hyperfine structure of H_2^+, where he measured the effective photo-dissociation rate of the molecule and compared the population of the molecular ion to the dissociation products (here H^+). The experiment achieved resolution of $\simeq$1.5 kHz for a transition at 1.243 GHz [56]. In 1976 infrared spectrum of rovibrational transition of HD^+ at $5.3 - 6.0$ μm range was observed using ion-beam laser spectroscopy [57], where the hyperfine structure of HD^+ was partially resolved with experimental resolution of 60 MHz (1823.533 ± 0.002 cm^{-1}). The fractional uncertainty of 1 ppm for the last two experiments remained unchallenged for three decades.

Development of new laser systems and application of advanced experimental techniques, like laser cooling and trapping of ions, facilitated the high resolution spectroscopy of the MHIs. In a pioneering work at the Institut für Experimentalphysik in Düsseldorf, HD^+ ions were simultaneously trapped with Be^+ ions in a linear Paul trap, where laser cooling of the atomic ions, and Coulomb interaction between HD^+ and Be^+, led to cooling of molecular ions. Since sympathetically cooled molecular ions are stored for long time at temperatures as low as 10 mK, laser spectroscopy with higher resolution is achievable. Rovibrational transitions between $(0,2) \rightarrow (4,1)$ and $(0,2) \rightarrow (4,3)$ with wavelength of $\simeq$1.4 μm and spectral resolution of 40 MHz were observed for the first time [58]. Application of this technique drastically improved precision spectroscopy of the MHIs. Fig. 3.1 shows a time evolution of some important measurements of the MHIs.

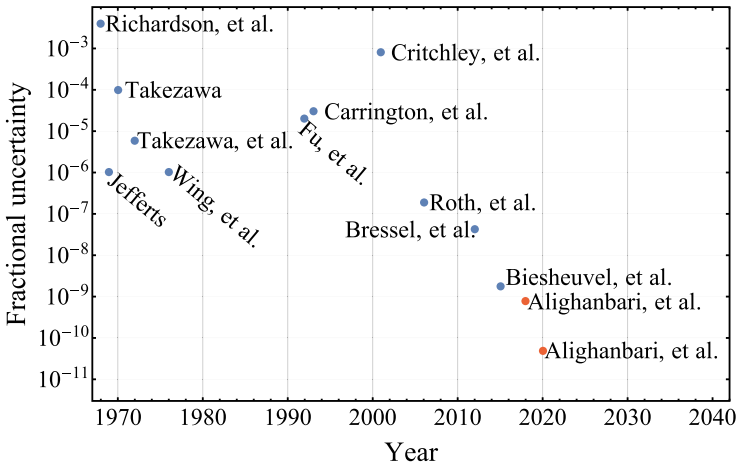

Figure 3.1. Experimental fractional uncertainty of different measurements on the spectroscopy of the MHIs. The two measurements indicated with red dots are the results of the present dissertation.

Resolution of the MHI spectroscopy prior to this thesis were limited by Doppler effect, except for the RF spectroscopy of H_2^+ [56]. Even those spectroscopy where the molecular ions are sympathetically cooled to $\simeq$10 mK suffered from residual Doppler broadening and unresolved hyperfine structure complicated the results. In this thesis, we invented a novel technique to perform Doppler-free spectroscopy of the MHIs.

3.2. Doppler-free spectroscopy of the MHIs

For atoms or molecules in gas phase Doppler broadening seems inevitable. In 1953, R. H. Dicke proposed a model which shows that Doppler-free spectroscopy of atomic and molecular samples is possible under special circumstances [59]. He calculated the spectral lineshape of an atom confined in a one dimensional box. If the dimension of the box a is a fraction of the transition wavelength λ, then the spectrum will be a normal Doppler distribution plus a sharp Doppler-free line. For a gas confined in a large volume, Doppler free spectrum can only be achieved if the mean free path of particle (in one dimension δx) is a fraction of the wavelength,

$$\delta x \ll \lambda/2\pi. \tag{3.1}$$

One experimental approach to fulfill the Lamb-Dicke condition (Eq. 3.1) is to employ resolved sideband laser cooling technique for few trapped ions [60]. A single ion or a few ion Coulomb crystal can be cooled to temperatures as low as 100 μK, where the extent of ion's motion is smaller than the wavelength of the interrogating laser [61]. The

resolved sideband cooling technique is an essential tool for quantum optics and quantum computing with ions.

The MHIs do not have suitable transitions for direct laser cooling, hence sympathetic cooling by another laser cooled ion remains as the only choice. The sympathetic cooling was first shown in 1986 where Hg^+ ion was sympathetically cooled by Be^+ ion [62]. Among very few atomic ions with suitable transition for laser cooling, Be^+ has a small charge-to-mass ratio close to that of the MHIs ($q/m \simeq 0.11\,e/u$ for Be^+ and $q/m \simeq 0.33\,e/u$ for HD^+), which facilitates simultaneous stable trapping of both ion species. The Lamb-Dicke regime can be reached by resolved sideband cooling of the atomic ion, where the Coulomb interaction between the two species provides sympathetic laser cooling and detection scheme for the molecular ion [63, 64]. In this technique both atomic and molecular ions are cooled down to their motional ground state, which is smaller than the wavelength of the investigated molecular transition. However, this technique is very challenging to implement, and we demonstrate a novel alternative to achieve the Lamb-Dicke regime with a simpler approach.

Instead of trapping single ions, we trap and laser cool few thousand Be^+ and few hundred HD^+ ions in a linear Paul trap [65, 66]. A frequency stabilized UV laser at 313 nm cools the Be^+ ions [67], where they form a prolate ellipsoidal shaped Coulomb crystal. The different charge-to-mass ratios of Be^+ and HD^+ leads to spatial (radial) separation which is determined by the trap parameters. The HD^+ ions with higher charge-to-mass ratio experience weaker trapping pseudo-potential and stay closer to the trap axis. We exploit this phenomenon to confine radially the HD^+ ions in a very small region. Lamb-Dicke condition is satisfied by (a) choosing a molecular transition with its wavelength larger than the radial extent of the ion (HD^+), and (b) choosing the radiation propagation direction transverse to the long axis of the prolate ellipsoidal. Fig. 3.2 shows the molecular dynamics simulation [68] of 2000 Be^+ and 200 HD^+ ions' positions at an arbitrary time. The projection of the ions' positions on the xy-plane shows that the extent of the radial positions of the HD^+ ions is less than 20 μm. Since the wavelength of our choice of fundamental rotational transition (Tab. 2.1) is 228 μm (= 1.3 THz), the radial confinement of the ions satisfies equation 3.1 if the radiation propagates along the y or x-axis.

3.3. Experimental setup

3.3.1. Trapping and cooling of Be^+ and HD^+

Ion trap

The ion trapping apparatus (Fig. A.1) is designed to confine HD^+ ions in a laser cooled Be^+ Coulomb crystal. Beryllium atoms are evaporated from an oven inside the vacuum

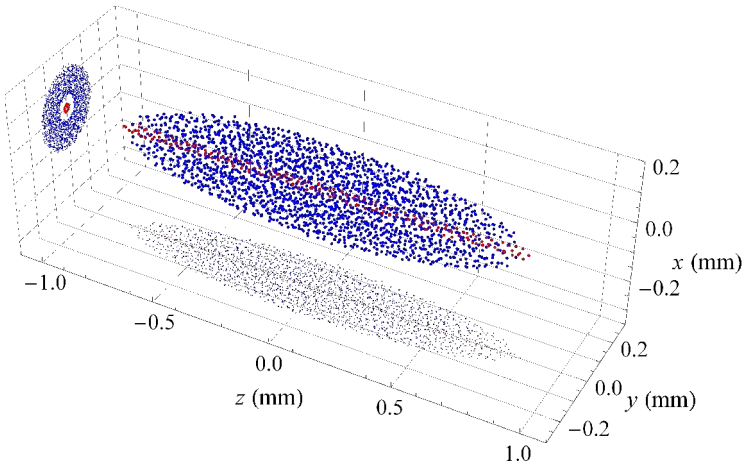

Figure 3.2. Simulated positions of 2000 Be^+ and 200 HD^+ ions at an arbitrary time. The blue and red spheres indicate Be^+ and HD^+ ions, respectively.

chamber which is then ionized through electron impact ionization. We use a linear Paul trap that consists of four cylindrical rods made of stainless steel. Each rod is divided into three electrically isolated segments, where the center electrode's length z_0 is 16 mm and the end-cap electrodes are 27 mm long. The electrodes' diameters are 9.9 mm and minimum distance measured from the surface of cylindrical electrodes to the trap axis R is 4.32 mm. Every segment is separately connected to the RF voltage and is provided with adjustable DC voltages [69]. This arrangement allows compensating stray electric fields due to possible excess charge. A synthesizer (SRS, DS345) referenced to hydrogen maser provides the RF frequency at $\Omega_{\mathrm{RF}} = 2\pi \times 14.16$ MHz. The end-cap DC voltages are $U_{\mathrm{ec}} = 4$ V.

Cooling laser

For Doppler cooling of Be^+, a 313 nm laser is used which is generated by frequency quintupling of a continuous wave (cw) Erbium doped distributed feedback (DFB) fiber laser at 1565 nm (Koheras K80-153-12). In order to achieve a closed cooling cycle, a repumper laser with frequency detuning of 1.25 GHz compared to the cooling laser is required which removes the population from the unwanted dark state. Therefore, the master laser is modulated using an electro-optical phase modulator (EOM). The phase-modulated master laser is amplified to 13 W in a polarization-maintaining erbium doped fiber amplifier (EDFA, IPG EAR-15K-C-LP-SF-UD) and a chain of nonlinear optical crystals generates the cooling laser at the desired wavelength (see Fig. 3.3 and Fig. A.4).

For frequency stabilization of the cooling laser, a fraction of the third harmonic at 522 nm is split and frequency shifted using a double-pass acousto-optic frequency modulator (AOM1). The frequency-shifted third harmonic then passes through AOM2, where

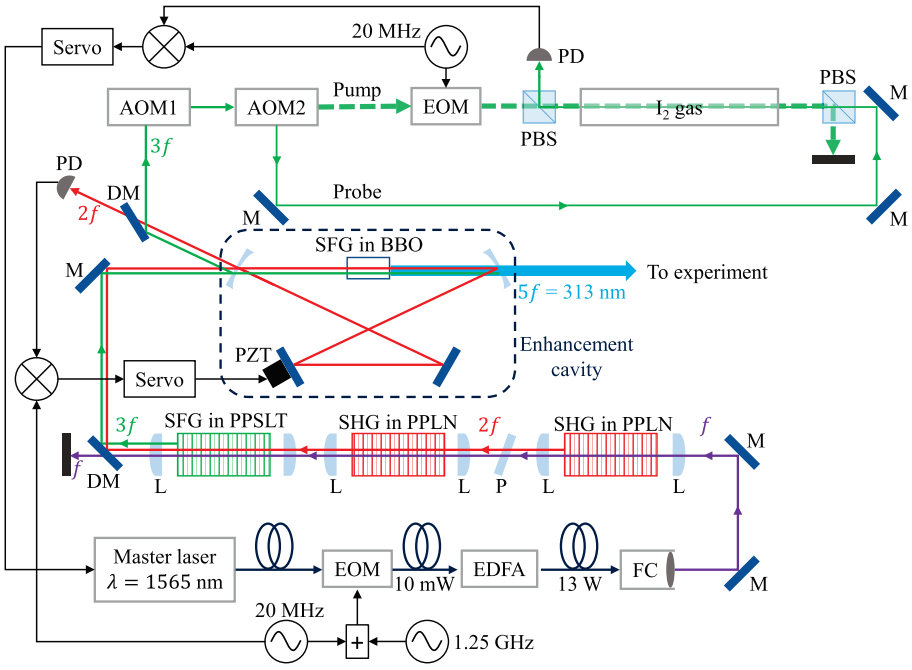

Figure 3.3. Simplified scheme of the setup for generation and frequency stabilization of the cooling laser. FC: fiber collimator, M: mirror, L: lens, P: Brewster plate for phase mismatch compensation, DM: dichroic mirror, PD: photodetector, PBS: polarizing beam splitter, SFG: sum frequency generation, SHG: second harmonic generation, PPLN: periodically poled lithium niobate crystal, PPSLT: periodically poled stoichiometric lithium tantalate crystal, BBO: Beta barium borate crystal, PZT: piezo-electric transducer, f: frequency of the master laser.

the zeroth and first order beams are used as pump and probe inputs for saturation spectroscopy of molecular iodine gas. The pump beam is phase modulated by an EOM, and the demodulated error signal is used for frequency control of the master laser. Fig. 3.4 shows the absorption spectrum of I_2 molecule, where the black arrow indicates the hyperfine transition component used as the frequency reference for our experiment. The cooling laser frequency f_{UV} is related to the iodine frequency f_{I_2} via $f_{UV} = (5/3) \cdot (f_{I_2} - 2f_{AOM1} - f_{AOM2}/2)$, where f_{AOM1} and f_{AOM2} are modulation frequencies of the AOMs. The cooling laser frequency can be fine-tuned by tuning f_{AOM1}, and it is tuned in such a way that the fluorescence of the ions increases for a warmer Coulomb crystal.

Experimental determination of the trap RF potential

The trap RF potential is measured using analysis of the secular motion spectrum of the trapped Be^+ ions, through detection of the UV fluorescence of the ions. The scattered UV light from the trapped cold Be^+ ions are collected using a triplet lens inside the vacuum chamber close to the trap. A photo-multiplier tube (PMT) located outside the vacuum

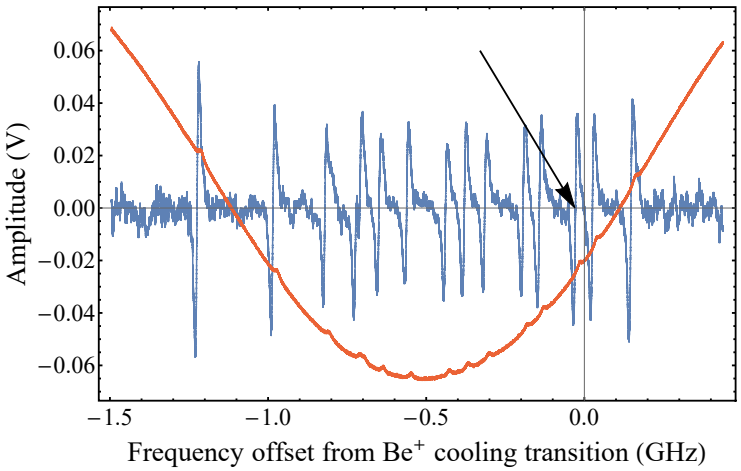

Figure 3.4. A sub-Doppler absorption spectrum of I_2 molecule (15 cm long iodine cell at 30 °C) in the range relevant for the Be^+ laser cooling applications. The blue trace is the Doppler background with hyperfine structure Lamb dips and the red trace is the demodulated error signal. The arrow shows the error signal used for stabilization of the cooling laser.

chamber detects the fluorescence and a CCD camera (PCO, type Sensicam) images the Coulomb crystal. The blade electrode inside the vacuum chamber is used to excite the secular motion of the trapped ions and consequently increases the atomic fluorescence. Fig. 3.5 shows the fluorescence change of Be^+ ions with excitation of the radial secular motion.

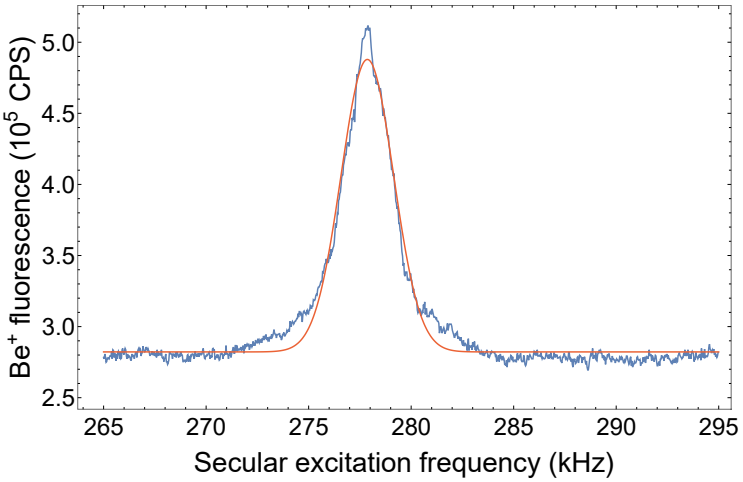

Figure 3.5. Radial secular motion spectrum of Be^+. The red trace is a fitted Gaussian function.

Since the radial secular frequency ω_r depends on the trap geometry and the trap RF po-

tential and the end-cap voltage,

$$\omega_r = \sqrt{-\frac{Q\kappa U_{\mathrm{ec}}}{m_{\mathrm{Be}} z_0^2} + \frac{Q^2 V_{\mathrm{RF}}^2}{2m_{\mathrm{Be}}^2 R^4 \Omega_{\mathrm{RF}}^2}}, \tag{3.2}$$

analysis of the secular motion spectrum defines the RF potential of the trap. In Eq. 3.2, Q is the charge and m_{Be} is the mass of Be^+, and κ is a dimensionless constant which depends on the geometry of the electrodes. For experimental determination of V_{RF}, the radial secular frequency ω_r is deduced from the secular spectrum for different values of the end-cap voltage U_{ec} (see Fig. 3.6). Extrapolation of ω_r to zero end-cap voltage is equal

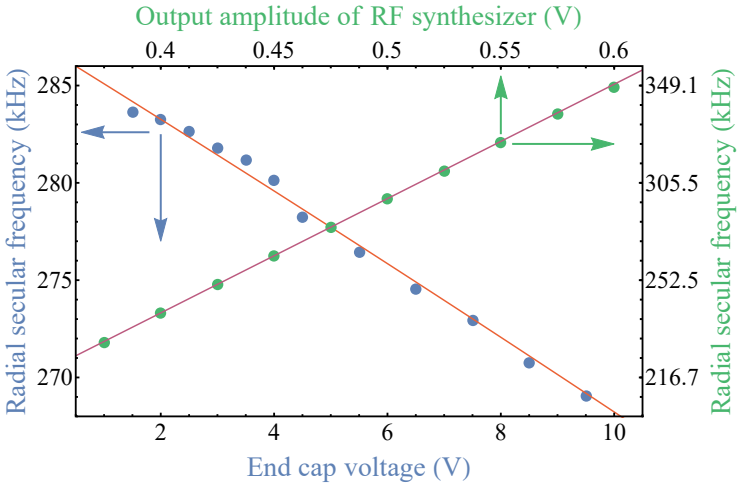

Figure 3.6. Radial secular frequency of Be^+ as a function of end-cap voltage (blue data points fitted with the red line). The error bars of blue data points are smaller than the marker size. The intercept of the fitted red line and y-axis can be used to find the trap RF potential for a given output amplitude of the RF synthesizer. The green data points show radial secular frequency of Be^+ for different output amplitudes of the RF synthesizer and 4 V end-cap voltage.

to $\sqrt{Q^2 V_{\mathrm{RF}}^2 / 2m_{\mathrm{Be}}^2 R^4 \Omega_{\mathrm{RF}}^2}$, where the only unknown is the trap RF potential. The result of trap RF potential measurement is essential for analysis of trap-induced systematic shifts.

Trapping the HD^+ ions

Following Be^+ loading and characterization of the trap potential, HD gas is released into the vacuum chamber via a piezo-electric leak valve (Oxford Applied Research, PLV1000). The ionization of HD gas is achieved through electron impact. As mentioned in sec. 3.2, the amount of trapped HD^+ ions is crucial to achieve the Lamb-Dicke regime, therefore the voltage for the piezo-electric leak valve is applied carefully via analysis of the CCD image and the vacuum pressure.

The radial secular frequency of HD^+ ions is essential for our spectroscopy scheme (as explained in sec. 3.3.2) and can be measured by applying secular excitation to the trapped HD^+ ions. The excitation of HD^+ secular motion heats up the Be^+ ions and consequently the detected fluorescence changes. Fig. 3.7 shows the detected fluorescence of Be^+ while scanning the excitation frequency around the secular frequency of HD^+.

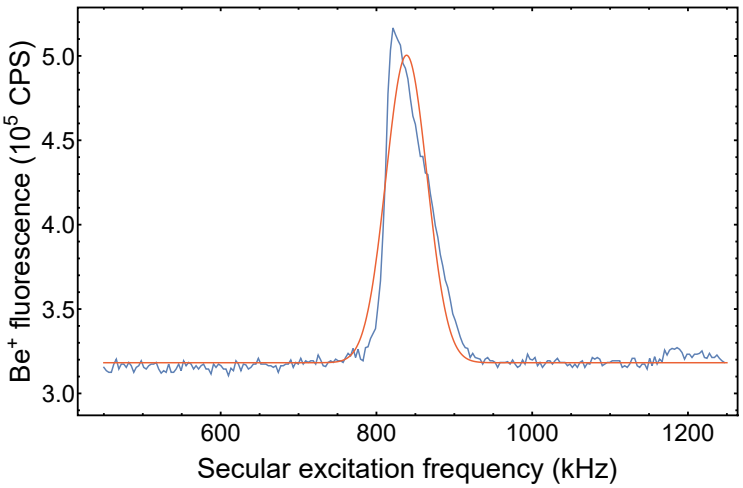

Figure 3.7. Radial secular motion spectrum of HD^+. The red trace is fitted Gaussian function.

3.3.2. Detection scheme

An essential part of the experimental sequence is to read out the number of the HD^+ ions in the $(0,1)$ state in presence of the THz radiation, and compare it with the case when there is no THz radiation. If the THz radiation frequency is in resonance with the HD^+ ion transition, the excited state population should be more compared to the non-resonant THz frequency or in absence of the THz radiation. The population is detected by dissociating HD^+ ions in the $(0,1)$ state. A quantitative prediction of fraction of dissociated molecules, for an assumed radiation power of $50\,\mathrm{mJ/mm^2}$, shows that a wavelength of 266 nm effectively dissociates HD^+ ions from the $v = 4$ vibrational state [70]. Therefore, the detection is performed through resonance enhanced multi-photon dissociation (REMPD), where the population in the $(0,1)$ state is excited with an infrared (IR) laser resonantly to the $(4,0)$ state and then the 266 nm radiation dissociates the molecular ions.

IR laser

A cw laser at 1.419 μm drives the $(0,1) \rightarrow (4,0)$ transition. For the experimental results presented in chapter 4, a tunable laser source (Agilent 81600B) generating 1.419 μm radiation is employed. The typical effective linewidth of the laser, when the coherence control

is on, is around 50 MHz with 1.4 mW output power. In order to achieve better signal-to-noise ratio for the experiment in chapter 5, we used a DFB laser (NTT electronics) with maximum output power of 18 mW (~6 mW is used for the spectroscopy), which is referenced to a wavemeter (HighFinesse, WS/7) with a linewidth of ~ 5 MHz. The narrower linewidth of the DFB laser allows to precisely dissociate the HD^+ ions from a specific hyperfine state. The hyperfine selective dissociation is a crucial step towards resolving specific Zeeman components of hyperfine transitions.

266 nm laser

The cw 266 nm radiation at 25 mW dissociates the molecules from $(4,0)$ state. Since the dissociation is into the continuum, the exact wavelength and linewidth of the 266 nm laser is irrelevant. The 266 nm laser is generated by frequency doubling a 2 W laser at 532 nm (Verdi-5W). The second harmonic generation takes place in a Beta Barium Borate (BBO) crystal placed inside a bow-tie enhancement cavity. The enhancement cavity is stabilized using the Pound-Drever-Hall technique [71]. Fig. 3.8 shows the scheme and Fig. A.5 shows photo of the setup.

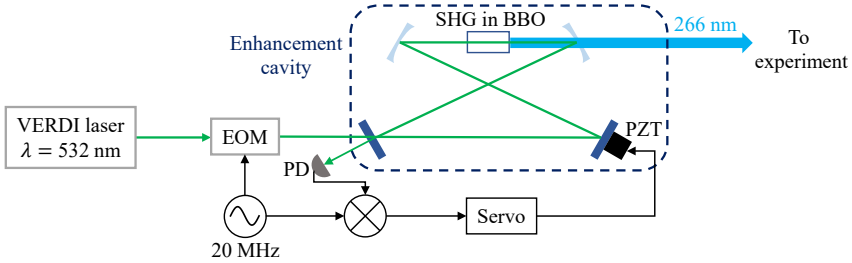

Figure 3.8. Scheme of the cw 266 nm laser setup. PZT: piezo-electric transducer, PD: photodetector, SHG: second harmonic generation.

Fractional loss of ions assessment

The fractional loss of HD^+ number before and after the REMPD is detected through applying an RF field sweeping 20 kHz around the resonant secular frequency of HD^+ (see Fig. 3.7). The indirect heating of Be^+ ions, and therefore the change in fluorescence, is proportional to the number of trapped HD^+ molecules. Fig. 3.9 illustrates the change in the fluorescence for different amount of trapped molecular ions when the same continuous secular excitation frequency and amplitude is applied. Repeating the "secular excitation - REMPD - secular excitation" sequence for a fixed THz frequency and averaging the fractional population loss provides the spectroscopy result.

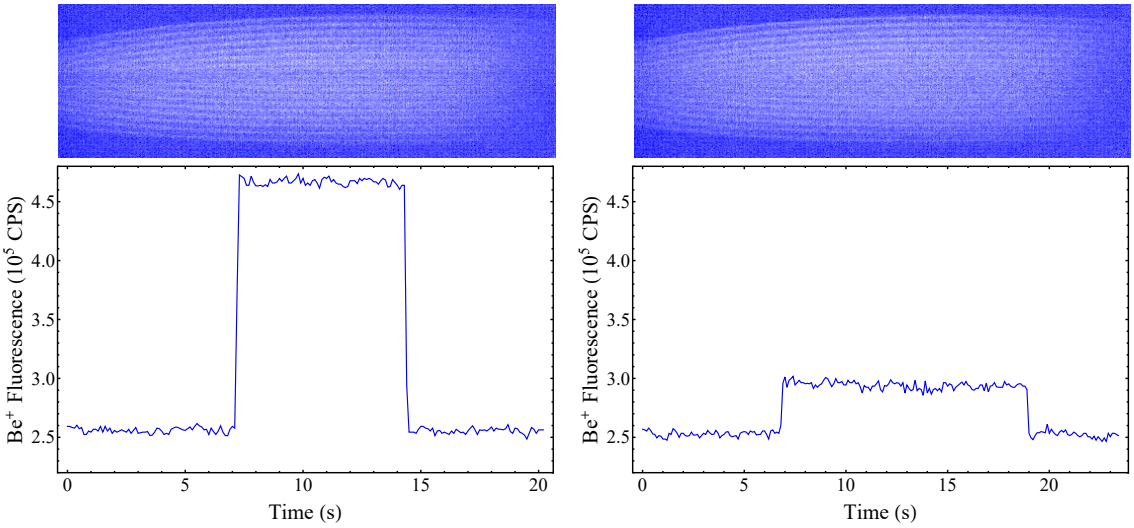

Figure 3.9. Top: CCD image of Be^+ ion Coulomb crystal and simultaneously trapped HD^+ molecules. The thicker dark region in the center of crystal of the left image shows that more HD^+ molecules are trapped. Bottom: Change in the detected fluorescence due to continuous excitation of secular motion of HD^+, where the fluorescence changes is proportional to the number of trapped molecular ions.

3.3.3. Laser induced rotational cooling of HD^+

The excited vibrational levels of HD^+ have lifetimes of order 10 ms and spontaneously decay into the ground vibrational level, where black-body radiation redistributes the population between rotational sub-states until a thermal equilibrium is reached. Enhancement of the population in the ground rotational state $(0,0)$ is another crucial step towards improvement of signal-to-noise ratio. We use two cw lasers to drive $(0,2) \rightarrow (1,1)$ and $(0,1) \rightarrow (2,0)$ transitions, where spontaneous decay from the respective excited states populates the $(0,0)$ state (see Fig. 3.10).

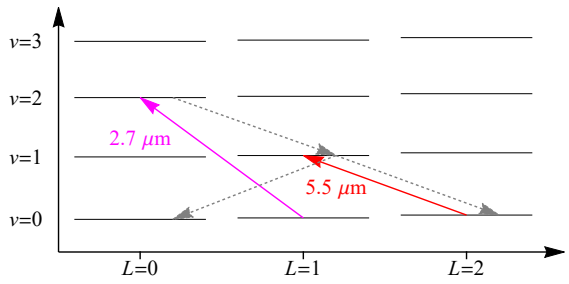

Figure 3.10. Partial rovibrational energy level scheme of HD^+ and the rotational cooling transitions. The dashed arrows show the spontaneous decay channels.

A DFB laser (Nanoplus) generates 2.713 μm radiation with maximum output power of 5 mW. The laser power used for spectroscopy of HD^+ is 200 μW. The DFB laser is

frequency stabilized using molecular CO_2 gas as a reference. The CO_2 gas is contained in a one meter long gas cell at room temperature and 100 mbar pressure. Fig. 3.11 shows the experimental setup for frequency stabilization. Since there are no molecular transitions

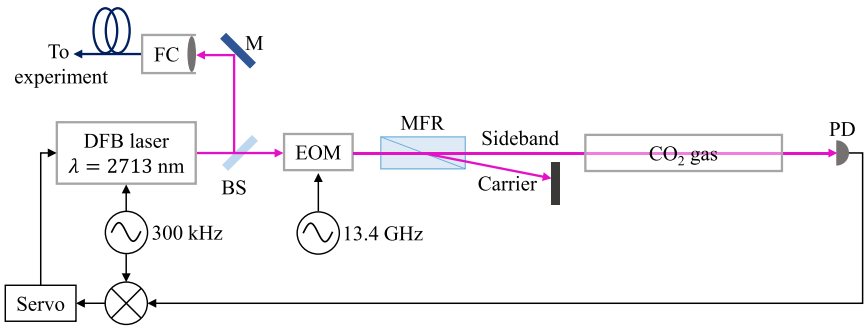

Figure 3.11. Scheme of the frequency stabilization setup for the DFB laser. The EOM imposes sidebands, whose polarization are orthogonal to the polarization of the carrier. A MgF_2 Rochon polarizing beam splitter (B. Halle) separates the sidebands and the carrier. MFR: MgF_2 Rochon polarizing beam splitter, PD: photodetector, FC: fiber collimator, BS: beam splitter, M: mirror.

of sufficient strength close enough to the $(0,1) \rightarrow (2,0)$ transition frequency of HD^+, it is necessary to produce frequency sidebands and stabilize those to molecular lines, allowing the carrier to be on resonance with HD^+ transitions. We use an EOM with central frequency of 13 GHz and bandwidth of ±5 GHz to modulate the laser. Based on the bandwidth of the EOM, a suitable molecular absorption line exists which is 13.4 GHz away from the HD^+ transition, as shown in Fig. 3.12. While the laser is locked, the sideband frequency is swept by ±50 MHz around 13.4 GHz and 3 s rate, to effectively address all of the hyperfine components of the rovibrational transition.

For depopulating the $(0,2)$ state, we use a quantum cascade laser (QCL) at 5.483 μm with maximum output power of 10 mW (Alpes lasers). Frequency stabilization of the QCL laser is based on absorption spectroscopy of ammonia (NH_3) gas contained in a 1 m long gas cell at 30 mbar. There is 720 MHz offset between the nearest ammonia transition frequency to the target frequency of the HD^+ transition. We exploit the broad linewidth of the ammonia molecular transition at room temperature and lock the laser to the side of resonance. The laser frequency is modulated at 100 kHz and demodulated error signal is used for the frequency stabilization (see Fig. 3.13). As shown in Fig. 3.14, a small DC voltage is applied to shift the DC offset of the error signal, and the lock box phase is set such that it locks the laser to the side of resonance. The DC offset defines the laser frequency, therefore its correct value can be determined via spectroscopy of HD^+. We lock the laser frequency with an arbitrary DC offset, and then simultaneously apply the continuous secular excitation of HD^+ and irradiate the ions with the QCL, 266 nm, and IR lasers. The IR laser is resonant with $(1,1) \rightarrow (5,0)$ transition of HD^+ at 1.475 μm. The DC offset is tuned until the QCL frequency is in resonance with the HD^+ transition, where the dissociation of molecular ions reduces the detected fluorescence, as demonstrated in

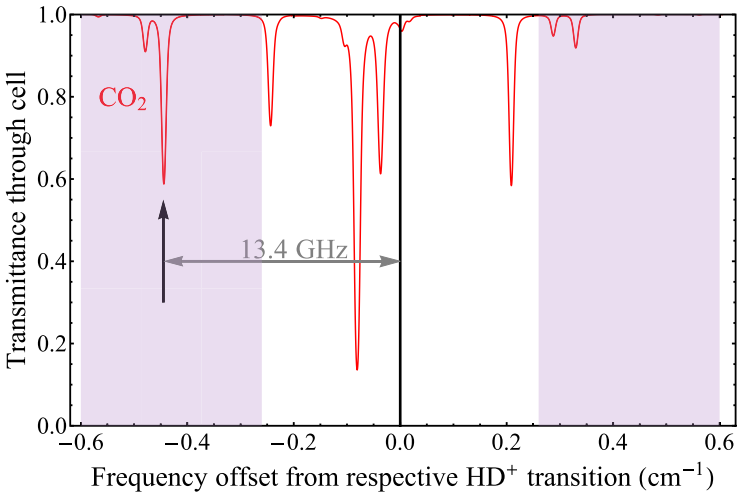

Figure 3.12. CO_2 absorption spectrum relevant for frequency stabilization of the DFB laser. The shaded areas are the allowed regions for the frequency reference dictated by the bandwidth of the EOM. The black arrow designates the transition that serves as the frequency reference. The data is extracted from HITRAN (https://hitran.org/).

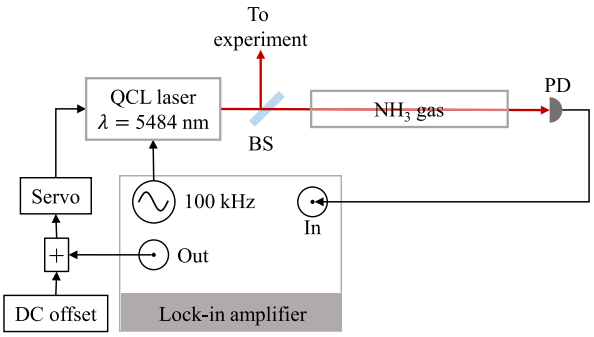

Figure 3.13. Scheme of the QCL frequency stabilization setup. BS: beam splitter, PD: photo detector.

Fig. 3.15.

Simultaneous irradiation of the HD^+ ions with DFB and QCL lasers will effectively increase the population in the ground state, which in turn leads to improved signal-to-noise ratio of the spectroscopy results. The efficiency of the rotational cooling can be examined by comparing the REMPD from the ground rovibrational state. When the IR laser is tuned to the $(0,0) \rightarrow (4,1)$ transition at 1.404 μm, the rate of the molecular dissociation depends on the number of molecules in the $(0,0)$ state. Fig. 3.16 shows comparison of different dissociation rates for the cases with and without the rotational cooling.

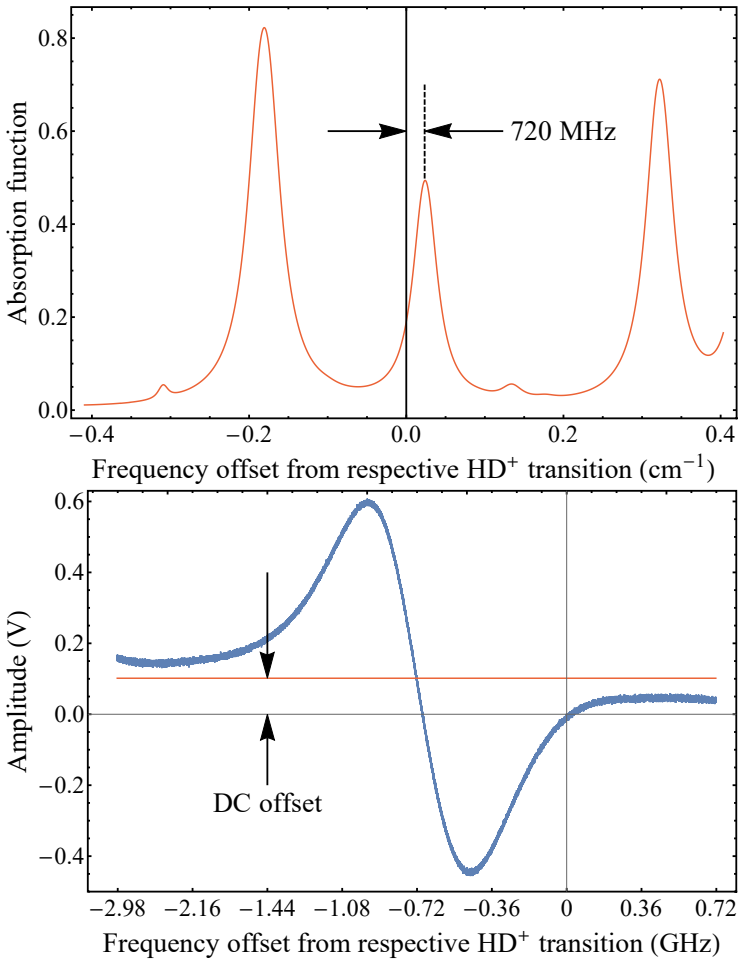

Figure 3.14. Top: Absorption function of ammonia relevant for frequency stabilization of the QCL laser. The data is extracted from HITRAN. Bottom: The error signal generated by a molecular absorption of NH_3 gas (Blue trace).

3.3.4. Spectroscopy procedure

The preparation and spectroscopy sequence consists a sequence of rotational cooling, secular excitation, and REMPD shown in Fig.3.17, which provides one data point of spectroscopy. The sequence is repeated sufficient number of times to obtain a reasonable signal-to-noise ratio.

After each HD^+ loading, typically 5 spectroscopy cycles are performed, and then all of the trapped ions except Be^+ are purged. The cleaning process of the Be^+ crystal includes two main parts. First, ions with charge-to-mass ratio smaller than Be^+ are removed from the trap. The linear Paul trap is a mass filter and unwanted trapped ions can be purged by changing the stability conditions. By inducing sufficiently large DC electric field, the trap will be unstable for the ions with smaller charge-to-mass ratio than Be^+. The upper limit for the applied DC electric field is defined with the stability condition of the Be^+ ions.

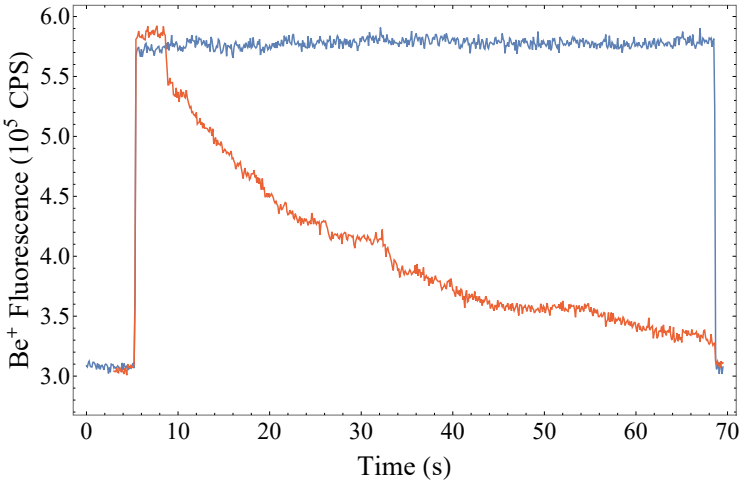

Figure 3.15. Detected fluorescence during tuning of the DC offset voltage of the QCL laser's error signal. When the DC offset is incorrect the number of trapped molecular ions stays the same (blue trace). The decay in the red trace indicates that the DC offset, and hence the QCL frequency, is correctly tuned such that the REMPD procedure dissociates the molecules and reduces the population of the trapped HD^+ ions.

Second, ions with charge-to-mass ratio larger than Be^+ are removed by scanning secular excitation frequency between 350 kHz and 1650 kHz and blocking the cooling laser for three to five seconds. The cleaning process is computer controlled and additional details can be found in [72]. The CCD images of Coulomb crystal with contaminant ions, with HD^+ ions, and when it is cleaned are shown in Fig. 3.18.

In each sequence of spectroscopy the magnetic field is set to $B_0 = 45\,\mu$T along the trap axis, except during the REMPD, where it is set to a value B_{REMPD} along the THz radiation. The magnitude and direction of magnetic field in the trap center is controlled via three sets of coils in nearly Helmholtz configuration. A three channel DC power supply (R&S®HMP4030) is computer controlled and provides the currents for the coils. Since every element of the trap apparatus is made of nonmagnetic materials, no magnetic hysteresis is observed. The magnitude of B_{REMPD} is sufficient to split Zeeman components of the studied hyperfine transitions. Different magnitudes of B_{REMPD} are chosen to investigate the systematic DC Zeeman shift.

3.4. High precision rotational spectroscopy of HD^+

3.4.1. Resolving hyperfine and Zeeman components

In chapter 4 we demonstrate the first experimental realization of the proposed technique. We chose the $|0,0,1,2,2\rangle \rightarrow |0,1,1,2,3\rangle$ transition, which possesses the highest transition

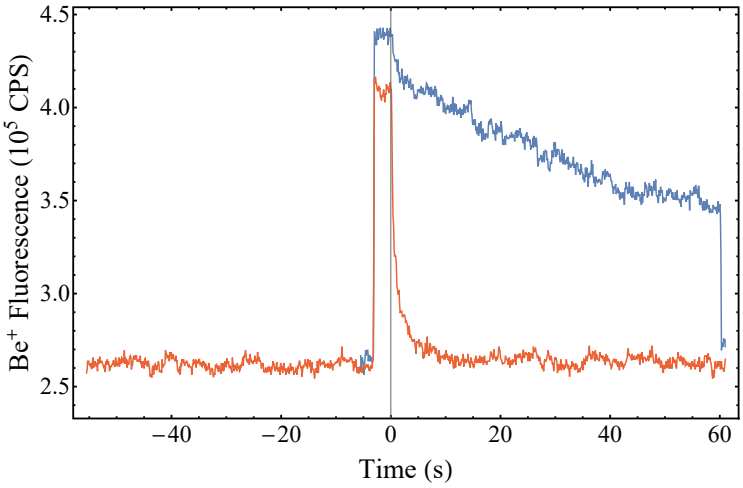

Figure 3.16. The REMPD from the $(0,0)$ level, when the rotational cooling populates the ground state (red trace) and when no ground state preparation is performed (blue trace). The state preparation increases the population in the ground state, and hence increases the HD^+ ion loss rate. The time origin is shifted to start of the REMPD.

probability compared to other hyperfine transitions. A finite magnetic field (~ 300 mG) in the direction of the THz radiation wave vector was applied to remove the Zeeman degeneracy. Among different Zeeman components, we carried out the spectroscopy between states with the maximum projection quantum number, $m_F = \pm 2 \rightarrow m'_F = \pm 3$. According to theory, these two Zeeman components have purely linear Zeeman shifts. Elimination of Doppler broadening allowed us to observe these two componets. The power broadening was observed by performing the spectroscopy at three different THz intensities, achieving the full width at half maximum (FWHM) of 1 kHz for the lowest intensity. However, further reduction of intensity was restricted due to small signal-to-noise ratio and insufficient control of the THz power.

In chapter 5 a half-wave plate and a polarizer were used in the path of the THz radiation to improve the power adjustment, and we applied the hyperfine selective dissociation to enhance the signal-to-noise ratio (see sec. 3.3.2). Consequently, we improved the experimental resolution and exploited the full capacity of our novel technique to measure 9 Zeeman components of 6 different hyperfine transitions.

3.4.2. Experimental determination of systematic shifts

Any interaction of the HD^+ ions with its environment, electric and magnetic fields, and electric field of laser radiations during the REMPD introduces a frequency shift of the transition. For high precision test of QED theory and determination of fundamental constants, we need to measure these systematic frequency shifts very precisely and apply the corresponding corrections in order to obtain the frequency of the unperturbed transition.

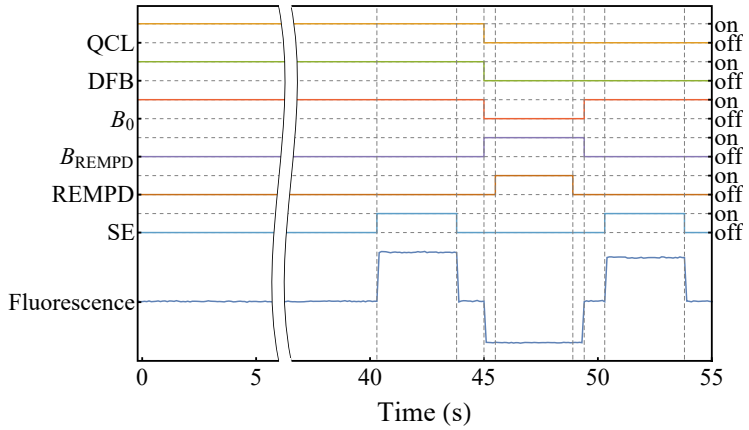

Figure 3.17. State of lasers, magnetic field, and secular excitation during one spectroscopy sequence and detected fluorescence of Be^+. The fluorescence decrease between 45.5 s and 49.5 s is due to the change in the magnitude and direction of the magnetic field. SE: secular excitation.

For the HD^+ ions the largest contribution to the systematic frequency shift, under our conditions, is due to the DC Zeeman effect. The transitions between different Zeeman components can have linear and/or quadratic dependence on the magnetic field. Other important systematic shifts are the DC and AC Stark shifts. The high resolution of our spectroscopy results allows us to study these systematic effects and compare the results with the *ab initio* calculations for the Zeeman effect and polarizability of the HD^+ ions.

In chapter 5, we present the first experimental analysis of different systematic shifts of HD^+ and use the results as corrections for the frequency of each transition. The quadratic dependence on the trap RF amplitude (micromotion and phase-offset induced Stark shifts) are measured by performing the spectroscopy of each individual transition at three differ-

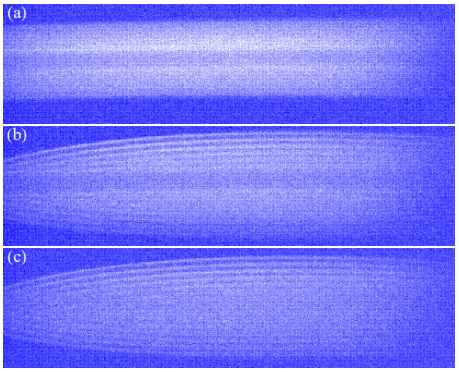

Figure 3.18. Laser cooled Be^+ Coulomb crystal image. (a) Contaminated crystal. Ions with charge-to-mass ratio smaller than Be^+ are located around the Be^+ ions and those with larger charge-to-mass ratio are located close to the axis. (b) Beryllium ion Coulomb crystal with HD^+ molecular ions. (c) Crystal image after the cleaning process.

ent trapping potentials. Extended Data Fig. 3 of chapter 5 illustrates the trap-induced shift for the $m_F = +2 \rightarrow m'_F = +3$ component of the $|0,0,1,2,2\rangle \rightarrow |0,1,1,2,3\rangle$ transition. We also measured the transition frequencies at three different magnitudes of magnetic field, for RF amplitudes close to 190 V. Consequently, we can use these measurements to determine the transition frequencies extrapolated to zero magnetic and trap-induced fields. Fig. 3.19 shows the extrapolated to $V_{\mathrm{RF}} \rightarrow 0$ transition frequencies of three Zeeman components of the $|0,0,0,1,1\rangle \rightarrow |0,1,0,1,2\rangle$ hyperfine transition, measured at different magnetic field magnitudes. The transitions with $\Delta m_F = m_F - m'_F = \pm 1$ have both linear and

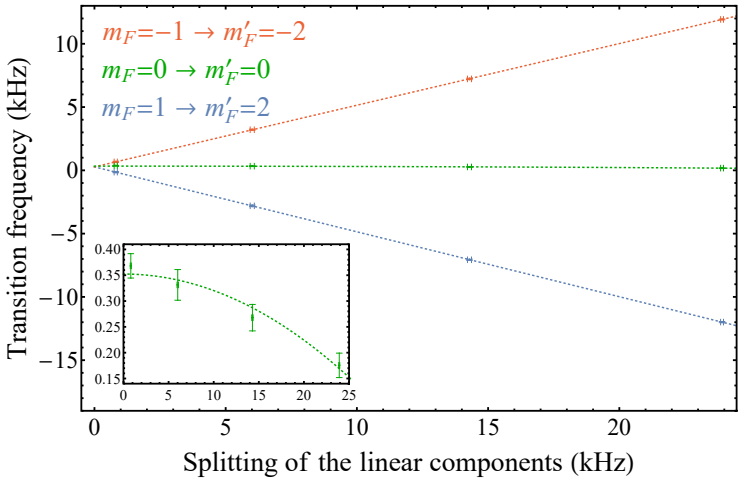

Figure 3.19. Zeeman shifts for three components of the $|0,0,0,1,1\rangle \rightarrow |0,1,0,1,2\rangle$ hyperfine transition at zero trap potential. The horizontal axis is the frequency splittings of the $m_F = +1 \rightarrow m'_F = +2$ and $m_F = -1 \rightarrow m'_F = -2$ transitions. The inset shows the $m_F = 0 \rightarrow m'_F = 0$ component, with the same horizontal and vertical axes as the main plot.

quadratic Zeeman dependence, while the $\Delta m_F = 0$ transition has pure quadratic dependence. According to theory predictions, the linear Zeeman coefficients for the $\Delta m_F = \pm 1$ transitions are $\mp 0.399 \times 10^{-2}$ kHz/μT, and the quadratic Zeeman coefficient is the same for both of the transitions, 5×10^{-6} kHz/μT^2.

Light shifts induced by the lasers present during the REMPD, AC Zeeman shift induced by the trap RF potential, DC Stark shift due to stray electric field, and line pulling effects are experimentally analyzed and the corresponding corrections are applied to find the unperturbed spin-averaged frequency.

4. Publication 1

Reproduced from

S. Alighanbari, M.G. Hansen, V. Korobov, S. Schiller

Rotational spectroscopy of cold and trapped molecular ions in the Lamb-Dicke regime,

Nat. Phys. **14**, 555-559 (2018)

DOI: 10.1038/s41567-018-0074-3

Author's contributions

All authors contributed to the work. My contributions to this work are:

- Rebuilding and adapting the existing ion trap apparatus. This includes modifying the vacuum chamber, designing and integrating a new beryllium oven, rearranging the CCD camera and PMT systems.
- Rebuilding the cooling laser, including its frequency stabilization subsystem, and optimizing its performance especially for our long measurement time.
- Rebuilding and optimizing the QCL laser system at 5.483 μm.
- Design and setup of the 266 nm laser and integrating it into the experimental setup.
- Design and setup of the DFB laser at 2.713 μm and integrating it into the experimental setup.
- I developed the idea of computer controlled cleaning of the Coulomb crystal, and together with M.G. Hansen supervised the development phase by Jana Scheuer [72].
- Design and development of the new magnetic field coils together with M.G. Hansen.
- Characterization of magnetic field in the position of ions through magnetometry of the Be^+ ions.

- Characterization of the THz source and integrating it into the experimental setup.
- I performed the spectroscopy and analyzed the experimental results.
- I produced the simulation results and cooperated in theoretical calculations based on them.
- Cooperation in manuscript editing.

Copyright and license notice

nature physics

LETTERS

https://doi.org/10.1038/s41567-018-0074-3

Rotational spectroscopy of cold and trapped molecular ions in the Lamb–Dicke regime

S. Alighanbari[1], M. G. Hansen[1], V. I. Korobov[2] and S. Schiller[1*]

Sympathetic cooling of trapped ions has been established as a powerful technique for the manipulation of non-laser-coolable ions[1–4]. For molecular ions, it promises vastly enhanced spectroscopic resolution and accuracy. However, this potential remains untapped so far, with the best resolution achieved being not better than 5×10^{-8} fractionally, due to residual Doppler broadening being present in ion clusters even at the lowest achievable translational temperatures[5]. Here we introduce a general and accessible approach that enables Doppler-free rotational spectroscopy. It makes use of the strong radial spatial confinement of molecular ions when trapped and crystallized in a linear quadrupole trap, providing the Lamb–Dicke regime for rotational transitions. We achieve a linewidth of 1×10^{-9} fractionally and 1.3 kHz absolute, an improvement of ≃50-fold over the previous highest resolution in rotational spectroscopy. As an application, we demonstrate the most precise test of ab initio molecular theory and the most accurate (1.3×10^{-9}) determination of the proton mass using molecular spectroscopy. The results represent the long overdue extension of Doppler-free microwave spectroscopy of laser-cooled atomic ion clusters[6] to higher spectroscopy frequencies and to molecules. This approach enables a wide range of high-accuracy measurements on molecules, both on rotational and, as we project, vibrational transitions.

Rotational spectroscopy of gas-phase molecules is a time-honoured technique that has been fundamental for developing our knowledge of molecular structure[7]. Its range continues to be extended (in the laboratory, in astronomical observatories and in space instruments), for example, to cold molecules[8]. Nevertheless, rotational spectroscopy has, in the majority of cases, not been able to achieve ultrahigh spectroscopic resolution and accuracy. Enabling this would open up numerous opportunities for studies in molecular physics and in fundamental physics, such as tests of molecular quantum theory, measurement of magnetic and optical susceptibilities, investigation of collision interactions, tests of the time-independence of particle masses[9–13], and the measurement of fundamental constants[5,14–16].

In conventional (linear) rotational spectroscopy, resolution can be improved by cooling of the molecules to a cryogenic translational temperature T, but the gains possible with thermal cooling methods ($T\simeq10$ K) are modest[8], due to the $\sqrt{T}$-dependence of the Doppler linewidth. For untrapped, neutral molecules, a leap in resolution and accuracy in rotational spectroscopy was achieved with the introduction of Lamb-dip (saturation) spectroscopy[17,18]. It allowed the fractional line resolution to be improved by approximately a factor of 20–30 beyond the Doppler broadening, to 5×10^{-8} (ref. [17]). However, this level has not improved for nearly 50 years[19,20], because it is limited by time-of-flight broadening. In the context of molecular ions, ion trapping combined with sympathetic cooling by Doppler-laser-cooled atomic ions to the 'crystallized' cluster state provides a well-tested approach for further reducing T to the 10 mK level, with a concomitant reduction of the Doppler linewidth by approximately a factor 30 (ref. [5]).

Here, we not only realize this improvement for rotational spectroscopy but also achieve Doppler-free spectral resolution, by reaching the rotational Lamb–Dicke regime (LDR). The LDR is defined by $\delta x<\lambda/2\pi$, where δx is the range of the ions' motion along the spectroscopy beam direction $\hat{\mathbf{k}}||x$ (ref. [21]), and λ is the radiation wavelength. In prolate ion clusters of appropriate size, the ranges of motion orthogonal to the clusters' long axes (z) are δx, $\delta y<20$ μm. Directing $\hat{\mathbf{k}}$ orthogonal to z satisfies the LDR condition for rotational transition wavelengths, with typical values $\lambda_{\rm rot}\simeq0.2$–2 mm. Ultrahigh fractional and absolute frequency resolutions are thereby enabled. In contrast, vibrational spectroscopy, where wavelengths are $\lambda_{\rm vib}<8$ μm, yields lines exhibiting the classic Doppler width[5,22], often further complicated by unresolved hyperfine structure[15,16]. The presented method does not require complex techniques such as single-ion manipulation, ground-state cooling and quantum spectroscopy[23,24] to capitalize on the advantage of the LDR regime. The performance improvement in terms of fractional resolution is a factor of ≃50 compared to both previous trapped molecular ion ensemble spectroscopy[5,22] and to the highest-resolution rotational spectroscopy of neutral molecules reported so far[20], to the best of our knowledge.

To perform a stringent test of the new method, we choose the polar molecule with the smallest fundamental rotational transition wavelength $\lambda_{\rm rot,min}\simeq228$ μm ($f_{\rm rot,max}\simeq1.3$ THz): HD^+ in its ground electronic state ($^2\Sigma_g^+$). In addition, the feasibility of ab initio calculation of $f_{\rm rot}$ for HD^+ and of its sensitivities to external fields allows the spectroscopic accuracy of the method to be tested.

The basic concept is depicted in Fig. 1. In a prolate ion cluster of appropriate size, trapped in a linear quadrupole trap (trap axis is along z), the sympathetically cooled ions arrange approximately as a narrow tube aligned along the trap axis. Maximum ion radial distances from the axis are significantly smaller than the tube length. Molecular dynamics simulations for a cluster containing $N=200$ HD^+ ions (Cluster 1, see Methods) indicate r.m.s. transverse position variations (corresponding approximately to the range $\delta x/2$) $\Delta x=\Delta y\simeq8.4$ μm at $T=12$ mK, increasing slightly to 9.0 μm at 67 mK. These values are significantly smaller than $\lambda_{\rm rot}/2\pi\simeq36$ μm, indicating the LDR if $\hat{\mathbf{k}}$ is chosen perpendicular to the trap axis. For a more quantitative treatment, we estimate the spectroscopy line shape L induced by the ions' motion, neglecting recoil and spontaneous emission effects, by evaluating the ensemble-averaged Fourier spectrum of the spectroscopy wave's electric field amplitude seen by each moving ion, $E(\mathbf{r}_i,\,t)\propto\mathrm{Re}[\exp(i\Phi(\mathbf{r}_i(t))-i\omega t)]$, where

[1]Institut für Experimentalphysik, Heinrich-Heine-Universität Düsseldorf, Düsseldorf, Germany. [2]Bogoliubov Laboratory of Theoretical Physics, Joint Institute for Nuclear Research, Dubna, Russia. *e-mail: step.schiller@hhu.de

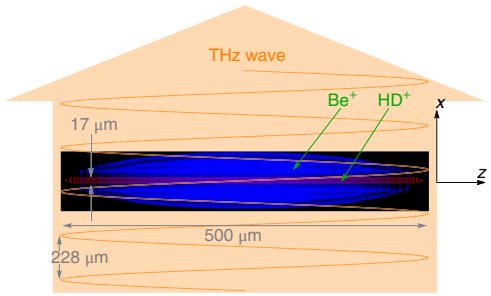

Fig. 1 | Principle of the Lamb–Dicke rotational spectroscopy of sympathetically cooled molecular ions. The ion cluster is prolate, and the sympathetically cooled ions exhibit a relatively small motional range in the directions *x*, *y* perpendicular to the trap axis *z*. The spectroscopy radiation propagates perpendicular to *z*. The ion cluster image is a time average of ion trajectories obtained from a molecular dynamics simulation of an ensemble of $N = 200$ HD^+ ions and $N_{Be^+} = 2,000$ atomic ions (see Methods). Ion clusters generated in the experiment are similar to the one shown here.

$\Phi(\mathbf{r}_i) = \mathbf{k} \cdot \mathbf{r}_i$. For transverse excitation along x, $\Phi(\mathbf{r}_i) = 2\pi x_i/\lambda$. We define $L(\Delta f) = \langle |\mathcal{F}_{\Delta f}\{\exp(i2\pi x_i(t)/\lambda)\}|^2 \rangle$, where the argument Δf of the Fourier transform $\mathcal{F}$ corresponds to the spectroscopic detuning from resonance and $x_i(t)$ are obtained from the molecular dynamics simulations and $\langle \ldots \rangle$ denotes the ensemble average. As shown in Fig. 2c, for $\lambda \leq 10\,\mu m$ (dashed lines) the line shape is close to Gaussian, with the full width at half maximum (FWHM) Δf_{FWHM} determined by the classic expression proportional to $\sqrt{T}$. For wavelengths $\lambda \geq 50\,\mu m$, the line shape shows features directly related to the x-coordinate spectral density (Fig. 2a), such as the drop for detunings larger than the secular frequency. In particular, because of the decreasing relative range with increasing λ and with decreasing temperature, a substantial delta function peak $L(0)$ (Lamb–Dicke peak) develops at $\Delta f = 0$. It is given by $L(0) = \langle |\exp(i2\pi x_i(t)/\lambda)| \rangle^2$ (the over-bar denotes the time average) and is shown in detail in Fig. 2d (points) as a function of wavelength. For the present wavelength $\lambda_{rot} \simeq 230\,\mu m$, nearly the complete line strength is in the Lamb–Dicke peak.

In the LDR, the absence of Doppler broadening and, because of ion confinement, also of transit-time broadening, puts into evidence other broadening mechanisms. However, pressure (collision) broadening can be suppressed by operating under ultrahigh-vacuum (UHV) conditions. Collisions between the trapped ions themselves do not lead to appreciable frequency shifts or broadening, because minimum approach distances are of the order of 10 μm. To reduce power (saturation) broadening below the 10^{-10} level for a typical strong transition, even for f_{rot} as high as 10^{12} Hz, extremely low power must be used (picowatt level).

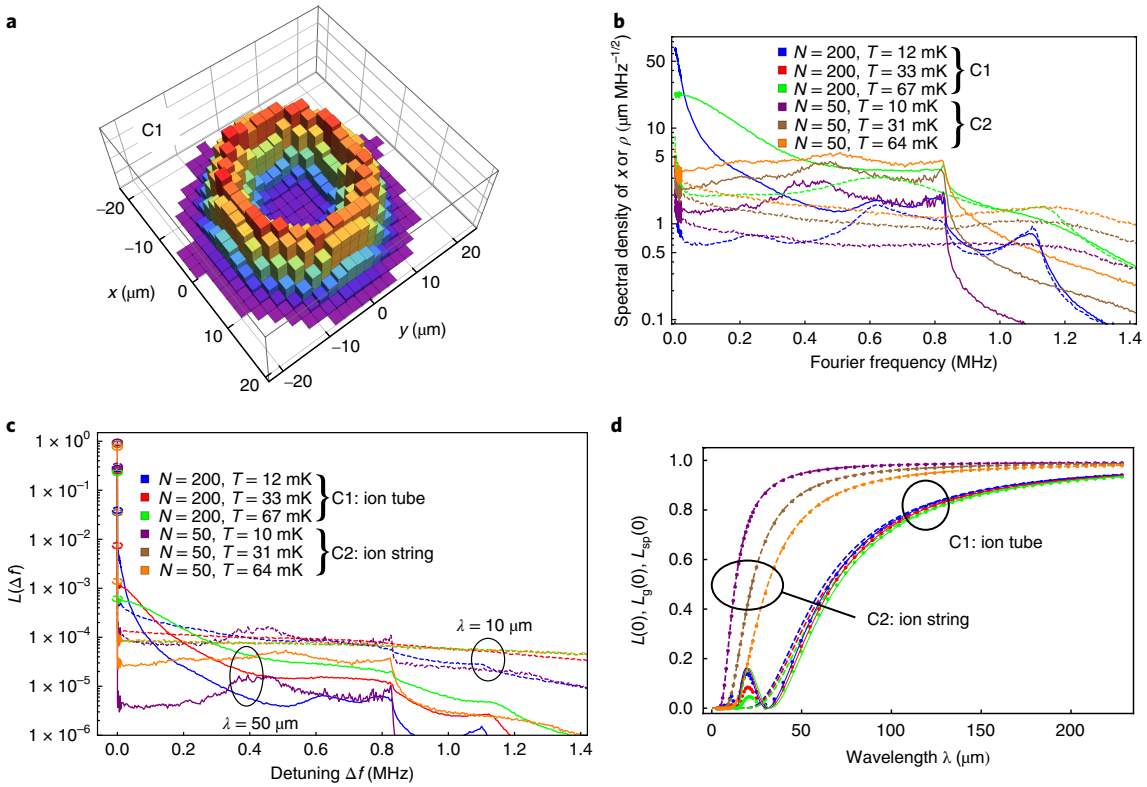

Fig. 2 | Characteristics and consequences of the motion of molecular ions in laser-cooled Be^+/HD^+ Coulomb clusters at different temperatures. Cluster C1 (C2): $N = 200(50)$, $N_{Be^+} = 2,000(500)$. The blue lines correspond to the situation in the experiment. **a**, Compound histogram of the transverse positions (x_i, y_i) of five randomly chosen molecular ions in cluster 1, at $T \simeq 33$ mK; the ring shape is related to the fact that, for the chosen ion numbers, the molecular ions arrange and move in a tubular cylindrical structure ('ion tube'). **b**, Ensemble average of the linear spectral density of the x coordinate of the ions (solid lines) and of the distance from the trap axis, $\rho = (x^2 + y^2)^{1/2}$ (dashed lines). The two spectra reflect the fact (evidenced by inspecting the ions' trajectories) that the transverse ion motion is a combination of a fast and small-range random motion perpendicular to the 'tube' axis, described by $\rho_i(t)$, and of a slower azimuthal motion around the tube, having a wider range. **c**, Qualitative spectral line shape $L(\Delta f)$, for two different wavelengths $\lambda = 50\,\mu m$ (solid lines), 10 μm (dashed lines). Only the positive detunings are shown. **d**, Strength of the Lamb–Dicke peak ($\Delta f = 0$). Points: exact values $L(0)$; dashed and solid lines: approximate expressions $L_g(0)$, $L_{sp}(0)$, respectively, defined in the Methods. The same colours in **b**–**d** correspond to the same cluster type and temperature. The transverse secular frequency of the molecular ions is 0.81 MHz; a corresponding feature is seen in the spectra of x and in the line shapes L.

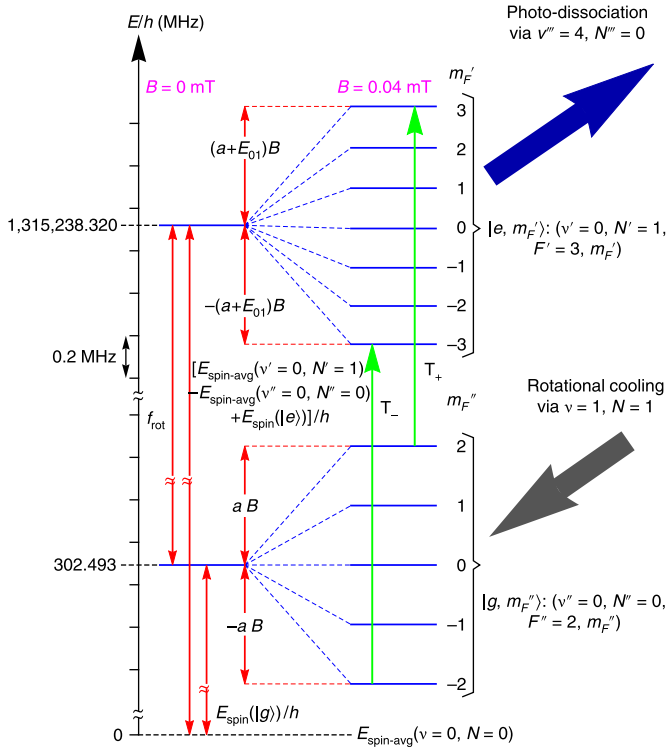

Fig. 3 | Simplified diagram of relevant energy levels of HD^+ in the ground vibrational level $v = 0$ of the $^2\Sigma_g^+$ electronic state. We show only one spin state, $F'' = 2$, of the ground rotational level $N'' = 0$, denoted by $|g\rangle$, and one spin state, $F' = 3$, of the first excited rotational level $N' = 1$, denoted by $|e\rangle$. The green arrows show the transitions $T_\pm$ addressed in this work, exhibiting a linear, and very small Zeeman splitting $2E_{01}B$. The population of the $N'' = 0$ spin states is enhanced by rotational cooling (thick grey arrow), and the population in the $N' = 1$ states is photo-dissociated by two lasers (blue arrow). The zero of the energy scale corresponds to the energy of the $v = 0$, $N = 0$ level in absence of the effective spin Hamiltonian interaction of ref. [33].

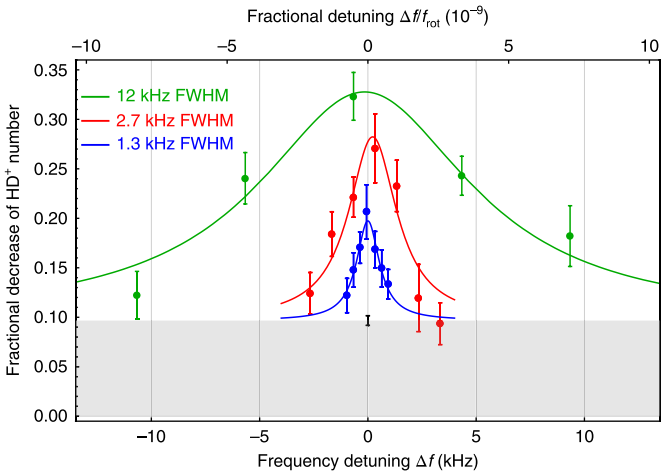

Fig. 4 | Spectroscopy of one hyperfine component of the fundamental rotational transition of HD^+. The unresolved transition pair $T_\pm$ between the stretched states, $(F'' = 2, m_{F''} = \pm F'') \rightarrow (F' = 3, m_{F'} = \pm F')$, at different power levels of the terahertz wave. The magnetic field is $B = 0.040(6)$ mT, measured with an anisotropic magnetoresistive probe and by radiofrequency spectroscopy of the Be^+ ions using the method of ref. [34]. The black error bar (the result of 500 experimental cycles) and the corresponding grey box indicate the background signal. The error bars are the standard error of the mean and the lines are Lorentzian fits. Zero detuning corresponds to the centre frequency of the blue fit.

Ultranarrow transitions may be challenging to find. Theoretical predictions and results from, for example, lower-resolution rovibrational spectroscopy may be helpful or necessary to reduce the spectral range of the search. Furthermore, performing the spectroscopy initially at high intensity leads to broad spectral lines, which are easier to find. The appropriate source power is easily satisfied by commercial devices.

To experimentally access the smallest possible linewidths, it is necessary to lift the Zeeman degeneracy of transitions by applying a magnetic field. Excitation of an individual Zeeman component implies excitation of only those molecules populating a single quantum state. Techniques for increasing the population in this state and thus the signal may therefore be required. Here, we use rotational laser cooling (see Methods).

The potential of rotational spectroscopy in the LDR can be harnessed fully only if the microwave source has excellent spectral purity (small linewidth) and high absolute frequency stability. For this work, we have implemented a frequency chain, where $f_{\mathrm{rot}} \simeq 1.3$ THz is referenced to a hydrogen maser (see Methods).

We address one particular spin component of the rotational transition, $|g\rangle = (v'' = 0, N'' = 0, F'' = 2) \xrightarrow{1.3\ \mathrm{THz}} |e\rangle = (v' = 0, N' = 1, F' = 3)$ of the ground electronic state $^2\Sigma_g^+$ (see Fig. 3). v, N and F denote the vibrational, rotational and total angular momentum quantum number, respectively. More precisely, we focus on two Zeeman components, T_+: $m_{F''} = 2 \rightarrow m_{F'} = 3$ and T_-: $m_{F''} = -2 \rightarrow m_{F'} = -3$ (m_F is the projection of the total angular momentum on the quantization axis). These connect so-called spin-stretched states (maximal F and m_F) and are advantageous for precision measurements because their Zeeman shift is strictly linear and tiny, $\Delta f_{\mathrm{rot,Zeeman}} = \pm E_{10}(v = 0, \quad N = 1)B = \pm 5.6\,\mathrm{kHz}(B/1\,\mathrm{mT})$ (ref. [25] and Methods). The mean frequency of T_+ and T_- is therefore free of any Zeeman shift. We computed the frequency ab initio using the most advanced techniques available (see Methods); in zero magnetic field

$$f_{\mathrm{rot,theory}} = 1,314,935.8273(10)_{\mathrm{theo}}\ \mathrm{MHz} \qquad (1)$$

Spectroscopy is performed by $1 + 1' + 1''$ resonance-enhanced multi-photon dissociation, where the upper spectroscopy level undergoes $|e\rangle \xrightarrow{1.42\ \mu\mathrm{m}} (v''' = 4, \ N''' = 0, \ F''' = 2) \xrightarrow{266\ \mathrm{nm}} \mathrm{H} + \mathrm{D}^+$. The reduction in the number of trapped HD^+ following dissociation is measured using secular excitation, and represents the spectroscopy signal. Repeated HD^+ trap loading and spectroscopy cycles are performed and the signals are averaged so as to increase the signal-to-noise ratio. Typical ion clusters used for spectroscopy are similar to the one shown in Fig. 1, having $T \simeq 10$ mK.

Figure 4 shows the measured spectrum $|g\rangle \rightarrow |e\rangle$ in the neighbourhood of $f_{\mathrm{rot,theory}}$. At comparatively high intensity ($\simeq 0.1\,\mu\mathrm{W\,mm^{-2}}$, green points), the linewidth is 12 kHz, whereas the calculated Doppler linewidth is 54 kHz. By reducing the source power successively, the line width decreases to 1.3 kHz (blue points). This clearly evidences power broadening. The latter linewidth is mostly due to residual power broadening. To obtain sufficient signal strength, we did not lift the Zeeman degeneracy completely and the spectrum contains the unresolved superposition of the pair T_+ and T_-.

Systematic shifts were computed or estimated, resulting in a frequency correction $\delta f_{\mathrm{rot,exp,syst}} = 0.0(3)$ kHz (see Methods). We obtain the rotational frequency

$$f_{\mathrm{rot,exp}} = 1,314,935.8280(4)_{\mathrm{stat}}(3)_{\mathrm{syst}}\ \mathrm{MHz} \quad (2)$$

The statistical uncertainty results from the experimental line centre resolution.

The value $f_{\mathrm{rot,exp}}$ is in agreement with the ab initio prediction $f_{\mathrm{rot,theory}}$. This represents the most accurate test of a molecular physics prediction, and is limited by the current uncertainty of the theory value, 8×10^{-10}.

The ab initio value $f_{\mathrm{rot,theory}}$ is based on the CODATA2014 values of the fundamental constants[26], in particular on the proton mass m_{p}. Among the stable fundamental particles of atomic physics, this is the particle that currently has the largest fractional mass uncertainty (9×10^{-11}). We can obtain a value for m_{p} from the present experiment by treating it as a fit parameter, while taking the other constants, m_{d}, m_{e}, R_∞ and α, and their uncertainties from CODATA2014. The value then is

$$m_{\mathrm{p}} = 1.0072764669(13)\ \mathrm{u} \quad (3)$$

with fractional uncertainty 1.3×10^{-9}, where the statistical, the systematic and the theoretical error enter as a sum of squares. Our result is consistent with CODATA2014, and is obtained by a different measurement method. It is the most accurate result for m_{p} using molecular spectroscopy to date, and improves by a factor of 3.4 on the recent result[16].

Our experiment–theory agreement is a direct proof that the present method permits rotational frequency inaccuracy at the 9×10^{-10} level or better, without the necessity for corrections. The reasons for this are the long spectroscopy wavelength, the stretched-state transitions and the favourable conditions in the UHV ion trap, and not a particular insensitivity of the HD^+ test molecule to perturbations. Rotational transitions between stretched states, with Zeeman splittings comparable to the present one, are available in most species, owing to the structure of the underlying magnetic Hamiltonian and of the wavefunctions[25]. Therefore, similar inaccuracy levels should be achievable for numerous other molecular species.

The present work opens outstanding perspectives for precision physics. With improvements in signal strength, we expect that the spectroscopic resolution can be increased by at least one order, leading in addition to a systematic uncertainty $<3\times10^{-11}$ (see Methods). This will eventually allow testing of the ab initio prediction of the rotational frequency of the HD^+ molecular ion[27–30] with corresponding accuracy, then providing also a fairly direct test of the theory of the related molecular ions H_2^+ and D_2^+ and of antiprotonic helium. Eventually, the fundamental constants R_∞, m_{e}, m_{p} and m_{d} will become measurable at the 10^{-11} level by molecular spectroscopy. This complementary approach to the current ones will strengthen the overall consistency of this set of fundamental constants.

Our method opens up additional wide possibilities, for several reasons. Given the mass (m_{c}) of singly ionized laser-coolable atomic ions, molecular ions with a mass-to-charge-squared ratio $m/q^2 < m_{\mathrm{c}}/e^2$ can be confined inside the atomic ion cluster, in the rotational Lamb–Dicke regime. Employing, for example, the high-mass ytterbium ion $^{171}Yb^+$ as a coolant, many thousands of singly ionized ($q=e$) molecular species, not counting isotopologues, have a suitable mass. Many of these species exhibit a simpler spin structure than the test case used here, which can be advantageous in simplifying the spectrum and increasing state populations. A general method for preparing molecular ions in the ground rovibrational level ($v=0$, $N=0$) is cryogenic buffer gas cooling[31]. It is also applicable to homonuclear ions, including H_2^+ and D_2^+ (ref. [32]).

Finally, the present method should be applicable also to rotational stimulated Raman transitions driven by co-propagating waves and to two-photon vibrational transitions. The latter would be driven by counter-propagating waves f_1 and f_2 having a sufficiently small frequency difference $|f_1-f_2| < c\,/\,2\pi\delta x$, ensuring the LDR. It is particularly advantageous that, in diatomics, transitions exist for which f_1 and f_2 can be chosen to satisfy this condition and also to be near-resonant with a dipole-allowed transition to an intermediate rovibrational level, so that the two-photon transition rate is enhanced.

Methods

Methods, including statements of data availability and any associated accession codes and references, are available at https://doi.org/10.1038/s41567-018-0074-3.

Received: 4 October 2017; Accepted: 2 February 2018;
Published online: 26 March 2018

References

1. Raizen, M., Gilligan, J., Bergquist, J., Itano, W. & Wineland, D. Ionic crystals in a linear Paul trap. *Phys. Rev. A* **45**, 6493 –6501 (1992).
2. Waki, I., Kassner, S., Birkl, G. & Walther, H. Observation of ordered structures of laser-cooled ions in a quadrupole storage ring. *Phys. Rev. Lett.* **68**, 2007–2010 (1992).
3. Bowe, P. et al. Sympathetic crystallization of trapped ions. *Phys. Rev. Lett.* **82**, 2071–2074 (1999).
4. Barrett, M. D. et al. Sympathetic cooling of $^9Be^+$ and $^{24}Mg^+$ for quantum logic. *Phys. Rev. A* **68**, 042302 (2003).
5. Bressel, U. et al. Manipulation of individual hyperfine states in cold trapped molecular ions and application to HD^+ frequency metrology. *Phys. Rev. Lett.* **108**, 183003 (2012).
6. Berkeland, D. J., Miller, J. D., Bergquist, J. C., Itano, W. M. & Wineland, D. J. Laser-cooled mercury ion frequency standard. *Phys. Rev. Lett.* **80**, 2089–2092 (1998).
7. Townes, C. & Schawlow, A. *Microwave Spectroscopy* (Dover, New York, NY, 1975).
8. Jusko, P., Asvany, O., Wallerstein, A.-C., Brünken, S. & Schlemmer, S. Two-photon rotational action spectroscopy of cold OH^- at 1 ppb accuracy. *Phys. Rev. Lett.* **112**, 253005 (2014).
9. Schiller, S. & Korobov, V. Test of time-dependence of the electron and nuclear masses with ultracold molecules. *Phys. Rev. A.* **71**, 032505 (2005).
10. Shelkovnikov, A., Butcher, R. J., Chardonnet, C. & Amy-Klein, A. Stability of the Proton-to-Electron Mass Ratio. *Phys. Rev. Lett.* **100**, 150810 (2008).
11. Uzan, J.-P. Varying constants, gravitation and cosmology. *Living Rev. Relativ.* **14**, 2 (2011).
12. Godun, R. M. et al. Frequency ratio of two optical clock transitions in $^{171}Yb^+$ and constraints on the time variation of fundamental constants. *Phys. Rev. Lett.* **113**, 210801 (2014).
13. Huntemann, N. et al. Improved limit on a temporal variation of m_p/m_e from comparisons of Yb^+ and Cs atomic clocks. *Phys. Rev. Lett.* **113**, 210802 (2014).
14. Roth, B. et al. in *Precision Physics of Simple Atoms and Molecules. Lecture Notes in Physics* Vol. 745 (ed. Karshenboim S. G.) 205–232 (Springer, Berlin, Heidelberg, 2008).
15. Koelemeij, J. C. J., Roth, B., Wicht, A., Ernsting, I. & Schiller, S. Vibrational spectroscopy of HD^+ with 2-ppb accuracy. *Phys. Rev. Lett.* **98**, 173002 (2007).
16. Biesheuvel, J. et al. Probing QED and fundamental constants through laser spectroscopy of vibrational transitions in HD^+. *Nat. Comm.* **7**, 10385 (2016).
17. Winton, R. S. & Gordy, W. High-precision millimeter-wave spectroscopy with Lamb dip. *Phys. Lett. A.* **32**, 219–220 (1970).
18. Cazzoli, G. & Dore, L. Observation of crossing resonances in the hyperfine structure of the $J = 1 \leftarrow 0$ transition of $DC^{15}N$. *J. Mol. Spectrosc.* **143**, 231–236 (1990).
19. Winnewisser, G., Belov, S. P., Klaus, T. & Schieder, R. Sub-Doppler measurements on the rotational transitions of carbon monoxide. *J. Mol. Spectrosc.* **184**, 468–472 (1997).
20. Cazzoli, G. & Puzzarini, C. Sub-Doppler resolution in the THz frequency domain: 1 kHz accuracy at 1 THz by exploiting the Lamb-dip technique. *J. Phys. Chem. A* **117**, 13759–13766 (2013).
21. Dicke, R. H. The effect of collisions upon the Doppler width of spectral lines. *Phys. Rev.* **89**, 472–473 (1953).
22. Germann, M., Tong, X. & Willitsch, S. Observation of dipole-forbidden transitions in sympathetically cooled, state-selected, homonuclear diatomic molecular ions. *Nat. Phys.* **10**, 820–824 (2014).
23. Wolf, F. et al. Non-destructive state detection for quantum logic spectroscopy of molecular ions. *Nature* **530**, 457–460 (2016).

24. Chou, C. et al. Preparation and coherent manipulation of pure quantum states of a single molecular ion. *Nature* **545**, 203–207 (2017).
25. Bakalov, D., Korobov, V. & Schiller, S. Magnetic field effects in the transitions of the HD^+ molecular ion and precision spectroscopy. *J. Phys. B* **44**, 025003 (2011); corrigendum **45**, 049501 (2012).
26. Mohr, P. J., Newell, D. B. & Taylor, B. N. CODATA recommended values of the fundamental physical constants: 2014. *Rev. Mod. Phys.* **88**, 035009 (2016).
27. Korobov, V. I., Hilico, L. & Karr, J. P. Theoretical transition frequencies beyond 0.1 ppb accuracy in H_2^+, HD^+, and antiprotonic helium. *Phys. Rev. A* **89**, 032511 (2014).
28. Korobov, V. I., Hilico, L. & Karr, J.-P. $m\alpha^7$-order corrections in the hydrogen molecular ions and antiprotonic helium. *Phys. Rev. Lett.* **112**, 103003 (2014).
29. Korobov, V. I., Koelemeij, J. C. J., Hilico, L. & Karr, J.-P. Theoretical hyperfine structure of the molecular hydrogen ion at the 1 ppm level. *Phys. Rev. Lett.* **116**, 053003 (2016).
30. Korobov, V. I., Hilico, L. & Karr, J.-P. Fundamental transitions and ionization energies of the hydrogen molecular ions with few ppt uncertainty. *Phys. Rev. Lett.* **118**, 233001 (2017).
31. Hansen, A. K. et al. Efficient rotational cooling of Coulomb-crystallized molecular ions by a helium buffer gas. *Nature* **508**, 76–79 (2014).
32. Schiller, S., Kortunov, I., Hernández Vera, M., Gianturco, F. & da Silva, H. Quantum state preparation of homonuclear molecular ions enabled via a cold buffer gas: An ab initio study for the H_2^+ and the D_2^+ case. *Phys. Rev. A* **95**, 043411 (2017).
33. Bakalov, D., Korobov, V. I. & Schiller, S. High-precision calculation of the hyperfine structure of the HD^+ ion. *Phys. Rev. Lett.* **97**, 243001 (2006).
34. Shen, J., Borodin, A. & Schiller, S. A simple method for characterization of the magnetic field in an ion trap using Be^+ ions. *Eur. Phys. J. D.* **68**, 359 (2014).

Acknowledgements

This work has been partially funded by Deutsche Forschungsgemeinschaft project Schi 431/19-1. V.I.K. acknowledges support from the Russian Foundation for Basic Research under grant no. 15-02-01906-a. We thank U. Rosowski for important assistance with the frequency comb, A. Nevsky for assistance with a laser system, E. Wiens for characterizing H-maser instability, D. Iwaschko, R. Gusek and P. Dutkiewicz for electronics development, J. Scheuer and M. Melzer for assistance, and S. Schlemmer (Universität zu Köln) for equipment loans. We thank K. Brown (Georgia Institute of Technology) for useful discussions and suggestions.

Author contributions

S.A. and M.G.H. developed the apparatus and performed the experiments; S.A., M.G.H. and S.S. analysed the data; S.A., S.S. and V.I.K. performed theoretical calculations; S.S. conceived the study, supervised the work and wrote the paper.

Competing interests

The authors declare no competing interests.

Additional information

Supplementary information is available for this paper at https://doi.org/10.1038/s41567-018-0074-3.

Reprints and permissions information is available at www.nature.com/reprints.

Correspondence and requests for materials should be addressed to S.S.

Methods

Simulation of ion dynamics in Coulomb clusters. The spatial distribution of ions in a two-species Coulomb crystal is well known[35]. Given an elongated trap and electrode geometry, and for typical magnitudes of the radiofrequency voltages and of the end-cap voltages, a strongly prolate atomic ion cluster can result. Sympathetically cooled molecular ions, if lighter than the atomic coolant ions, and if fewer in number, are distributed in a string-like or tube-like volume, centred on the trap axis (z). (Equal charge states are assumed.) The boundary shapes of the two species' spatial distributions are constant in time.

Molecular dynamics simulations help to elucidate details, in particular effects of temperature and dynamics. We simulated two ion clusters. Cluster C1 contains $N_{Be^+}=2{,}000$ Be^+ ions that sympathetically cool $N=200$ HD^+ ions, resulting in a tubular configuration for the latter. C1 is similar to the experimentally produced clusters (Fig. 1). A smaller cluster (C2) was modelled for comparison: with $N=50$, $N_{Be^+}=500$, the molecular ions arrange as a string. The simulations are performed in the pseudopotential approximation, since the micromotion of HD^+ ions gives only small corrections (here, the q-parameter is 0.15). The simulations extended over 5 ms. The equilibrium secular temperature T of the molecular ions is determined by the assumed cooling and heating rate parameters, which are varied in order to exhibit the temperature dependence of the clusters' properties[36]. A key feature of large clusters such as C1 is that even at the lowest temperatures achievable experimentally by sympathetic cooling, $T\simeq 10$–30 mK, the ions' positions are not completely 'frozen'. Instead, the ions diffuse through the cluster volume, with the diffusion speed being a function of temperature[36].

The ion motion characteristics can be analysed in detail. One characteristic is the coordinate r.m.s. variation, defined as $\Delta\xi=\langle\Delta\xi_i\rangle$, $\Delta\xi_i^2=\overline{\xi_i(t)^2}-\overline{\xi_i(t)}^2$, where i is the ion number, $\xi=x,y,z$, the over-bar denotes the time average and $\langle\ldots\rangle=N^{-1}\sum_{i=1}^{N}\ldots$ denotes the ensemble average. The values for C1 put in evidence transverse confinement and diffusion features: whereas for motion along the trap axis $\Delta z_{C1}=(41, 142, 206)$ μm over a time interval of 5 ms, at $T=(12, 33, 67)$ mK, respectively, the transverse excursions are $\Delta x_{C1}=\Delta y_{C1}=(8.4, 8.6, 9.0)$ μm. These latter values are significantly smaller than $\lambda_{rot,min}/2\pi$. In Fig. 2a,b, we show some details of HD^+ ion motion, the time-averaged spatial distribution of a tube-like cluster and the spectral density of the x coordinate. Two characteristics of the spectral density related to the increasing localization with decreasing temperature are: the increasing strength for near-zero frequency; and the strong drop in spectral density at frequencies larger than 0.81 MHz, the secular frequency. At the smallest simulated temperatures, the drop is stronger for the string-like ion cluster than for the tube-like cluster. For the former, the secular frequency eventually becomes the largest frequency of motion possible, because it is the frequency of the small (thermally driven) oscillations around the equilibrium positions. For the latter, the ions can still perform azimuthal motion and thus the spectrum differs qualitatively.

If the ions' coordinates $x_i(t)$ were Gaussian random variables, $L(0)$ would simplify to $L_g(0)=\langle\exp(-(2\pi\Delta x_i/\lambda)^2)\rangle$ (ref. [37]). Since in clusters of the sizes as in C1, C2, most ions behave similarly, $L_g(0)\simeq\exp(-(2\pi\Delta x/\lambda)^2)$. This expression explicitly shows the wavelength dependence, and is presented as dashed lines in the figure. The Gaussian assumption is well satisfied when the number of molecules N is reduced so far (cluster C2) that they arrange approximately like a string along the z axis, since their x histogram is then found to be Gaussian. For C2, $\Delta x_{C2}=\Delta y_{C2}\simeq(1.7, 3.0, 4.1)$ μm at $T=(12, 33, 67)$ mK increase approximately with the square root of the temperature, and thus more strongly in relative terms than for C1. This leads to a more pronounced variation of $L(0)$ with temperature than for C1 (see Fig. 2d). The small values Δx_{C2}, Δy_{C2} lead to a substantial $L(0)\simeq 0.3$ already for $\lambda\simeq 10$ μm when $T=13$ mK.

For the C1 cluster, the Gaussian assumption is not correct (see the histogram in Fig. 2a); therefore, deviations between $L_g(0)$ and $L(0)$ are visible in Fig. 2d for intermediate and small wavelengths. Heuristically, we find that the expression $L_{sp}(0)=J_0(2\pi\sqrt{2}\,\Delta x/\lambda)^2$, the result for a single ion harmonically oscillating along the x axis[38], provides a better description of the exact values because of the similarity in the probability distributions of the x coordinate values.

Thus, the simulations indicate that even for only moderately cold ensembles ($T\simeq 70$ mK) and for a relatively small rotational wavelength $\lambda_{rot,min}=228$ μm ($f_{rot,max}=1.3$ THz), strong signatures of Lamb–Dicke confinement in rotational spectroscopy with transverse incidence can be expected. For string-like ion clusters, a similar signature might be possible also for axial irradiation, but only at the lowest temperatures ($T\simeq 10$ mK), when ion position changes are infrequent.

Experimental apparatus. The ion trap apparatus used in the present work, shown in Supplementary Fig. 1, is based on the device used previously[5,39–41], and upgraded in several respects: fully computer-controlled operation, accurate magnetic field control via solenoid pairs, improved frequency stabilization of the rotational cooling lasers L-RC1 and L-RC2, and improved terahertz source frequency control.

The vacuum chamber housing the ion trap provides UHV conditions (3×10^{-11} mbar), minimizing spectral broadening and shifts due to ion–background gas collisions. Electron impact ionization inside the ion trap volume is used to generate beryllium ions from Be atoms emitted by a hot filament and HD^+ ions from HD gas injected into the chamber. A 313 nm radiation laser cools the beryllium ions that sympathetically cool the HD^+ ions, resulting in a structured ion cluster as shown in Fig. 1. Subsequently, radiation fields at 5.48 μm and 2.71 μm perform rotational cooling. The 1.3 THz radiation for rotational spectroscopy propagates at 90 degrees with respect to the ion trap axis and thus the ion cluster axis, in order to provide the LDR. The beam radius at the centre of the trap is approximately 1 mm. A CCD (charge-coupled device) camera images the cluster's spatial structure, allowing for a direct observation of the spatial confinement and also comparison with molecular dynamics simulations. The photo-multiplier tube detects the fluorescence of the Be^+ ions, and also provides the signal for the spectroscopy.

The terahertz system consists of a hydrogen maser, whose frequency, $f_H\simeq 1.4$ GHz, is down-converted to 10 MHz and then used as a reference for a microwave synthesizer operating at $f_{mmw}/72=18.262$ GHz. Its output is converted in a ×72 multiplier/amplifier chain to $f_{mmw}=f_{rot}=1.31$ THz (ref. [42]). We verified the high spectral purity of the terahertz wave at the intermediate frequency 18.251 GHz, close to $f_{mmw}/72$. The set-up used is shown in Supplementary Fig. 2 (inset). The repetition rate $f_{rep}\simeq 250$ MHz of a fibre-based optical frequency comb is stabilized by phase-locking the beat frequency between an ultrastable reference laser at 1.5 μm (L-ULE, with optical frequency f_{ULE}[43]) and a nearby comb mode (mode number $n\simeq 7.8\times10^5$) to a (maser-referenced) direct digital synthesizer (DDS) set at $f_{DDS}=50$ MHz, by controlling the repetition rate. The comb's carrier-envelope offset frequency f_{CEO} is independently stabilized to the H-maser. The absolute frequency stability of the reference laser is therefore transferred to the repetition rate, $f_{rep}=(f_{ULE}-f_{DDS}-f_{CEO})/n$. Comb radiation at 1.5 μm is detected by a fast photo-detector, and a radiofrequency signal arising from the 73rd harmonic of the repetition rate, $f_{rep}\times 73$, is generated. This harmonic is chosen because it can be set close to $f_{mmw}/72$. The difference frequency between $f_{rep}\times 73$ and $f_{mmw}/72$ is generated using a mixer and is analysed with a fast Fourier transform-based spectrum analyser. Supplementary Fig. 2 shows the linewidth of the difference frequency signal, which is 86 mHz. On the basis of this value and previous characterizations[42], we estimate a linewidth <10 Hz at 1.3 THz. We can also infer the long-term frequency stability of the terahertz wave, by comparing the maser frequency to a Global Positioning System (GPS)-derived 1 pulse per second signal and to a cryogenic silicon optical resonator[44]. The residual instability is negligible ($<1\times10^{-13}$ for integration times $\tau>10$ s) and so is drift.

Laser rotational cooling. In the present experiment, when molecular ions are generated and trapped and reach thermal equilibrium, the ($v''=0$, $N''=0$) level's population is ≃10%, and thus only ≃1% is in a single state $|g,m_F^{\,*}\rangle$. Therefore, before spectroscopy, we apply rotational laser cooling[40] (lasers L-RC1, L-RC2 in Supplementary Fig. 1), to significantly increase the population in ($v''=0$, $N''=0$), a procedure that also increases the population in the Zeeman states $|g,m_F^{\,*}\rangle$ to a level that can be observed.

We apply two laser fields that drive the fundamental vibrational transition ($v''=0$, $N''=2$) → ($v'=1$, $N'=1$), and the overtone vibrational transition ($v''=0$, $N''=1$) → ($v'=2$, $N'=0$), respectively. Owing to quantum mechanical selection rules, repeated absorption–spontaneous emission cycles transfer the majority of the ion population into the ground state ($v=0$, $N=0$).

The fundamental transition at 5.48 μm is driven by a quantum cascade laser (L-RC2 in Supplementary Fig. 1), whose frequency is stabilized to the side of a fringe of an NH_3 molecular transition. The overtone vibrational transition is excited by a distributed feedback laser at 2.71 μm (L-RC1 in Supplementary Fig. 1). The laser is frequency-stabilized to a CO_2 gas transition using an offset locking technique[45] to bridge the frequency gap between the CO_2 and the HD^+ transition frequencies.

Experimental sequence. The preparation and spectroscopy sequence consists of the following steps: (1) HD^+ generation by electron impact ionization; (2) impurity ion removal procedures; (3) rotational cooling for $t_{rc}=35$ s; (4) secular excitation for $t_{se}=3$ s, with rotational cooling lasers on; (5) during $t_{det}=3$ s, the rotational cooling lasers are blocked, while terahertz radiation and the 1.42 μm and 266 nm waves for resonance-enhanced multi-photon dissociation are on; (6) secular excitation during t_{se}. The signal is obtained from the difference in Be^+ fluorescence recorded during intervals (4) and (6).

The magnetic field is set to 0.11 mT along the trap axis z, except during step (5), where it is set to a smaller value B, sufficient to produce Zeeman splitting of most components of the studied transition. The sequence is repeated a number of times sufficient to obtain a reasonable signal-to-noise ratio. Be^+ ions are reloaded every 100 to 150 sequences.

Rotational transition. The fundamental rotational transition of the molecular ion used here has an important spin structure because of the electron and nuclear magnetic moments[33]. Whereas in the ground rovibrational level ($v''=0$, $N''=0$) they give rise to four spin states (having total angular momentum $F''=0$, 1, 2), in the first excited rotational level ($v'=0$, $N'=1$) the number increases to ten spin states (having $F'=0$, 1, 2, 3), because of the additional presence of rotational angular momentum $N''\neq 0$. Figure 3 shows the two spin states relevant to the spectroscopy of this work (for a complete diagram, see Fig. 2 in ref. [41]). A controllable magnetic field lifts the total angular momentum projection (m_F) degeneracies. We address transitions between two individual Zeeman components

$|g, m_{F''}\rangle$ of the $F''=2$ spin state of the $N''=0$ level, and two components $|e, m_F\rangle$ of the $F'=3$ spin state of the $N'=1$ level. These are the transitions T_+: $m_{F''}=2 \rightarrow m_{F'}=3$ and T_-: $m_{F''}=-2 \rightarrow m_{F'}=-3$, shown by green arrows in Fig. 3.

Ab initio theory of the HD$^+$ rotational transition. The transition frequency $f_{\mathrm{rot,theory}}$ involves two contributions. The first is the spin-averaged frequency $f_{\mathrm{spin\text{-}avg}}$. We have computed it with high accuracy using the same technique as in ref. [30], obtaining

$$f_{\mathrm{spin-avg}} = 1,314,925.752627(18)\ \mathrm{MHz}$$

CODATA2014 values[26] have been used and the relative uncertainty indicated is that due to theory, 1.4×10^{-11}. The second contribution is the hyperfine shift f_{spin} due to spin interactions (including coupling with the total orbital angular momentum), $f_{\mathrm{spin}} = [E_{\mathrm{spin}}(|e\rangle) - E_{\mathrm{spin}}(|g\rangle)]\ /\ h$. Here, $E_{\mathrm{spin}}(|e\rangle)$ and $E_{\mathrm{spin}}(|g\rangle)$ are the hyperfine spin energy shifts for the lower and upper states, respectively. So far, they have been calculated only within the Breit–Pauli approximation[33]. For the stretched states $|g, m_{F''}=\pm2\rangle$ and $|e, m_{F'}=\pm3\rangle$, including the Zeeman energy in a finite magnetic field B, we have previously derived the algebraic expression (equation (6) in ref. [25]),

$$\begin{aligned} E_{\mathrm{spin}}(v,N,F=N+2,m_F=\pm F,B)/\ h = {} & E_4\ /\ 4 + E_5\ /\ 2 \\ & + (E_1+E_2+2E_3+E_6+2E_7+2E_8+E_9)N\ /\ 2 \\ & - (2E_6+4E_7+4E_8+2E_9)N^2\ /\ 2 \\ & \pm (2E_{10}N+E_{11}+2E_{12}+E_{13})B\ /\ 2 \end{aligned}$$

where $E_i = E_i(v,N)$ are the coefficients of the effective spin Hamiltonian[25,33] and $E_{10}=E_{10}(v,N\geq1)\simeq-5\,\mathrm{kHz\,mT^{-1}}$ is the weakly v, N-dependent strength of the rotational Zeeman interaction $\mathbf{N}\cdot\mathbf{B}$. E_{11}, E_{12} and E_{13} are particle magnetic constants, with $a=(E_{11}+2E_{12}+E_{13})/2\simeq14.0\,\mathrm{MHz\,mT^{-1}}$. Since the $F''=2\rightarrow F'=3$ transition keeps the spin function untouched, the hyperfine shift f_{spin} is most sensitive to the electron spin–orbit interaction $E_1(v=0,N=1)(\mathbf{s}_e\cdot\mathbf{N})$, where $E_1(v=0,N=1)\simeq32\,\mathrm{MHz}$ (ref. [33]). The spin–spin interactions, proportional to E_4 and E_5, which are known with much higher accuracy than the other coefficients[29], give a much smaller contribution to f_{spin}, due to the similarity of the spin wavefunctions in $|g\rangle$, $|e\rangle$ that leads to a substantial cancellation. The hyperfine shift of the transitions $T_\pm$ is

$$f_{\mathrm{spin}} = 10.0747(10)\ \mathrm{MHz} \pm E_{10}(v=0,N=1)B \qquad (4)$$

Summing both above contributions, we obtain equation (1).

It is important to note that the theoretical considerations of the spin-averaged and the hyperfine spin shift contributions to $f_{\mathrm{rot,theory}}$ have recently been confirmed through a comparison, respectively, with one particular rovibrational transition frequency of HD$^+$ at the 1.1×10^{-9} level[16] and with several spin transition frequencies (that is, radiofrequency transitions) of H_2^+ at the 10^{-6} level[29].

The particular sensitivity of the observed transition to the accuracy of the effective spin Hamiltonian is characteristic for rotational transitions. For vibrational transitions, the much larger ratio of $f_{\mathrm{spin\text{-}avg}}$ to f_{spin} reduces the sensitivity to the latter significantly. This is the case for the most intensive hyperfine components of the transitions (for which $|f_{\mathrm{spin}}|<100$ MHz), and the Breit–Pauli approximation is then in most cases sufficient to guarantee a fractional uncertainty of the total transition frequency comparable to the fractional uncertainty of the theoretical spin-averaged frequency.

To improve the 1 kHz theoretical uncertainty of f_{spin}, it will be necessary to calculate the higher-order corrections to the coefficients E_1, E_6 and E_7. It is expected that a calculation of their contributions of relative order α^4 and partially of α^5 will be possible, with reduction of the uncertainty in f_{spin} by a factor of up to 10^3 and thus in $f_{\mathrm{rot,theory}}$ to the 1×10^{-11} level.

Systematic shifts. We have previously computed most relevant sensitivities of the rotational transition to external perturbations: Zeeman shift[25], electric quadrupole shift[46], d.c. Stark shift, black-body radiation shift, and spin-state dependences of the d.c. Stark and light shift[47]. For the experimental parameters of our trap, the cluster shape, and the moderate intensities of the radiation fields, the shifts of the transitions $T_\pm$ are all small, except for the linear Zeeman shift (the quadratic Zeeman shift is zero). In detail we have the following contributions.

(1) Since the orientation of the quantization axis and the populations of the lower Zeeman states are unknown, we assign a Zeeman uncertainty equal to half the Zeeman splitting of T_+ and T_-, 0.22 kHz. (2) The d.c. Stark shift has been computed taking into account ion trajectories and Coulomb fields, also allowing for d.c. offset potentials, and is less than 10 Hz. (3) Collision shifts related to background gas are negligible due to the UHV conditions, and effects of non-thermal velocity distribution[16] are considered negligible because of the spectroscopy technique used here and the magnitude of the hyperfine splittings. (4) The light shift induced by the 266 nm dissociation laser (35 mW power) has been evaluated by performing an accurate calculation of the a.c. polarizabilities of the lower and upper rotational levels using the procedure described in ref. [47]. We obtained the scalar (s) and tensor (t) polarizabilities $\alpha_s(v=0,N=0(1),\lambda=266.0\,\mathrm{nm})=3.677(3.687)$, $\alpha_t(v=0,N=0(1),\lambda=266.0\,\mathrm{nm})=0(-1.044)$, in atomic units. For the considered transitions, the shift is 7 (40) Hz. (5) Black-body radiation shift and electric quadrupole shift are negligible.

In total, we obtain a frequency correction of $\delta f_{\mathrm{rot,exp,syst}}=0.0(3)\,\mathrm{kHz}$.

In future studies, any light shifts from the dissociation laser and from the 1.4 μm laser could be avoided by applying these lasers only after the rotational excitation. If the Zeeman pair were split and resolved, the Zeeman shift uncertainty should be reduced at least tenfold. This would then allow a total systematic uncertainty of $<3\times10^{-11}$.

Outlook. We note that radiation sources of appropriate spectral purity and stability can be implemented not only using an H-maser as a reference but also more simply and accessibly using a GPS-steered high-performance quartz oscillator. For most molecules, the fundamental rotational transition frequency is smaller than 1 THz, which simplifies the source further. In a complementary direction, the method could also be applied to other rotational transitions $N''>0\rightarrow N'=N''+1$, with correspondingly higher frequencies and thus potentially higher fractional spectral resolution. It is possible that two-photon[48] and electric quadrupole rotational transitions could also become accessible.

Data availability. The data that support the plots within this paper and other findings of this study are available from the corresponding author upon reasonable request.

References

35. Hornekær, L., Kjærgaard, N., Thommesen, A. M. & Drewsen, M. Structural properties of two-component Coulomb crystals in linear Paul traps. *Phys. Rev. Lett.* **86**, 1994 (2001).
36. Zhang, C. B., Offenberg, D., Roth, B., Wilson, M. A. & Schiller, S. Molecular-dynamics simulations of cold single-species and multispecies ion ensembles in a linear Paul trap. *Phys. Rev. A* **76**, 012719 (2007).
37. Cramér, H. *Random Variables and Probability Distributions* (Cambridge Univ. Press, Cambridge, 1970).
38. Berkeland, D. J., Miller, J. D., Bergquist, J. C., Itano, W. M. & Wineland, D. J. Minimization of ion micromotion in Paul trap. *J. Appl. Phys.* **83**, 5025–5033 (1998).
39. Blythe, P., Roth, B., Fröhlich, U., Wenz, H. & Schiller, S. Production of ultracold trapped molecular hydrogen ions. *Phys. Rev. Lett.* **95**, 183002 (2005).
40. Schneider, T., Roth, B., Duncker, H., Ernsting, I. & Schiller, S. All-optical preparation of molecular ions in the rovibrational ground state. *Nat. Phys.* **6**, 275–278 (2010).
41. Shen, J., Borodin, A., Hansen, M. & Schiller, S. Observation of a rotational transition of trapped and sympathetically cooled molecular ions. *Phys. Rev. A* **85**, 032519 (2012).
42. Schiller, S., Roth, B., Lewen, F., Ricken, O. & Wiedner, M. Ultra-narrow-linewidth continuous-wave THz sources based on multiplier chains. *Appl. Phys. B* **95**, 55–61 (2009).
43. Wiens, E., Nevsky, A. Y. & Schiller, S. Resonator with ultrahigh length stability as a probe for equivalence-principle-violating physics. *Phys. Rev. Lett.* **117**, 271102 (2016).
44. Wiens, E. et al. A silicon single-crystal cryogenic optical resonator. *Opt. Lett.* **39**, 3242–3245 (2014).
45. Nevsky, A. Y. et al. Robust frequency stabilization of multiple spectroscopy lasers with large and tunable offset frequencies. *Opt. Lett.* **38**, 4903–4906 (2013).
46. Bakalov, D. & Schiller, S. The electric quadrupole moment of molecular hydrogen ions and their potential for a molecular ion clock. *Appl. Phys. B* **114**, 213–230 (2014).
47. Schiller, S., Bakalov, D., Bekbaev, A. K. & Korobov, V. I. Static and dynamic polarizability and the Stark and blackbody-radiation frequency shifts of the molecular hydrogen ions. *Phys. Rev. A* **89**, 052521 (2014).
48. Constantin, F. L. THz/infrared double resonance two-photon spectroscopy of HD$^+$ for determination of fundamental constants. *Atoms* **5**, 38 (2017).

nature physics

SUPPLEMENTARY INFORMATION

https://doi.org/10.1038/s41567-018-0074-3

In the format provided by the authors and unedited.

Rotational spectroscopy of cold and trapped molecular ions in the Lamb–Dicke regime

S. Alighanbari[1], M. G. Hansen[1], V. I. Korobov[2] and S. Schiller[1]*

[1]Institut für Experimentalphysik, Heinrich-Heine-Universität Düsseldorf, Düsseldorf, Germany. [2]Bogoliubov Laboratory of Theoretical Physics, Joint Institute for Nuclear Research, Dubna, Russia. *e-mail: step.schiller@hhu.de

Supplementary material to "*Rotational spectroscopy of cold and trapped molecular ions in the Lamb-Dicke regime*"

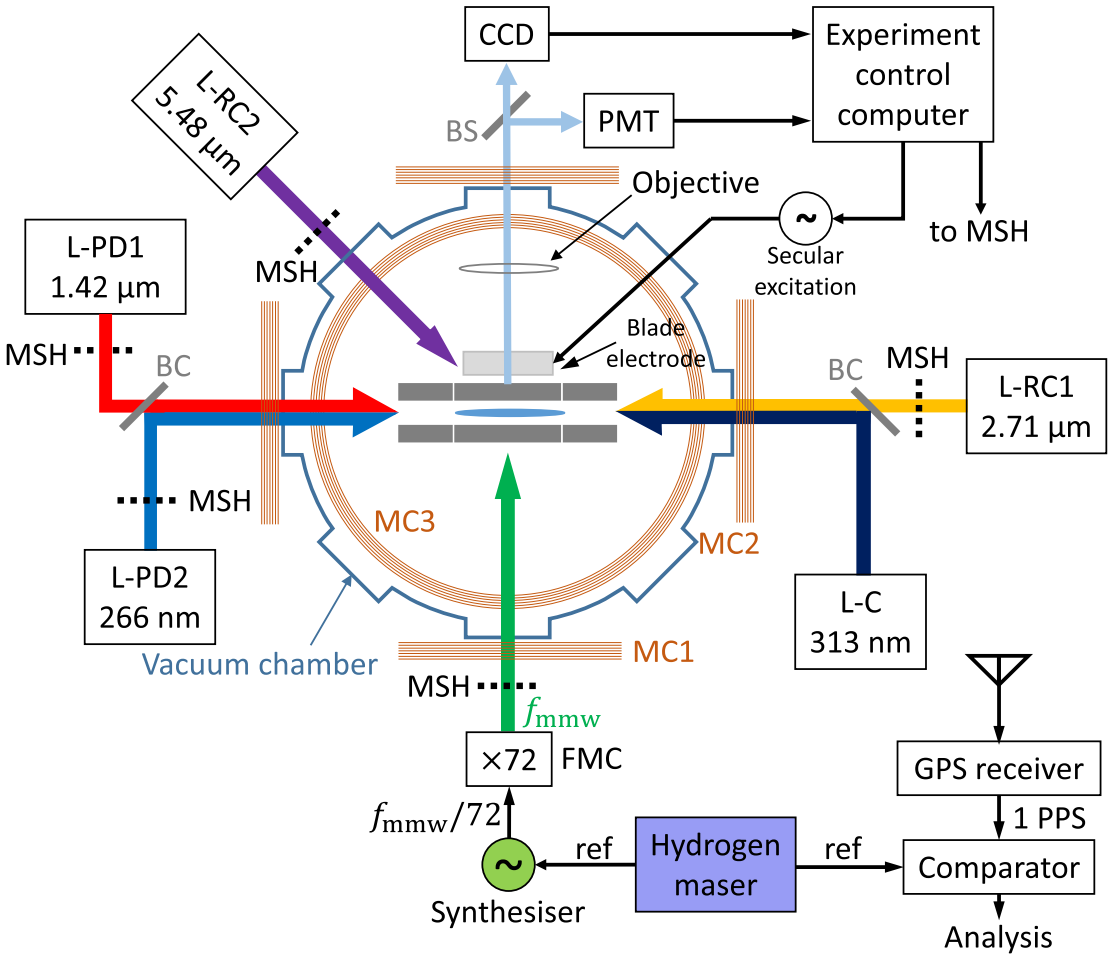

Supplementary Figure 1. **Simplified schematic of the apparatus.** The THz radiation (green arrow) propagates along x, perpendicularly to the ion cluster´s axis. BC: beam combiner, BS: beam splitter, FMC: frequency multiplier chain, MSH: mechanical shutter, L-PD: photo-dissociation lasers, L-RC: rotational cooling lasers, L-C: Be^+ cooling laser, PMT: photo-multiplier tube, MC: magnetic coils, CCD: CCD camera. Beryllium oven, electron gun, and HD gas handling system are not shown.

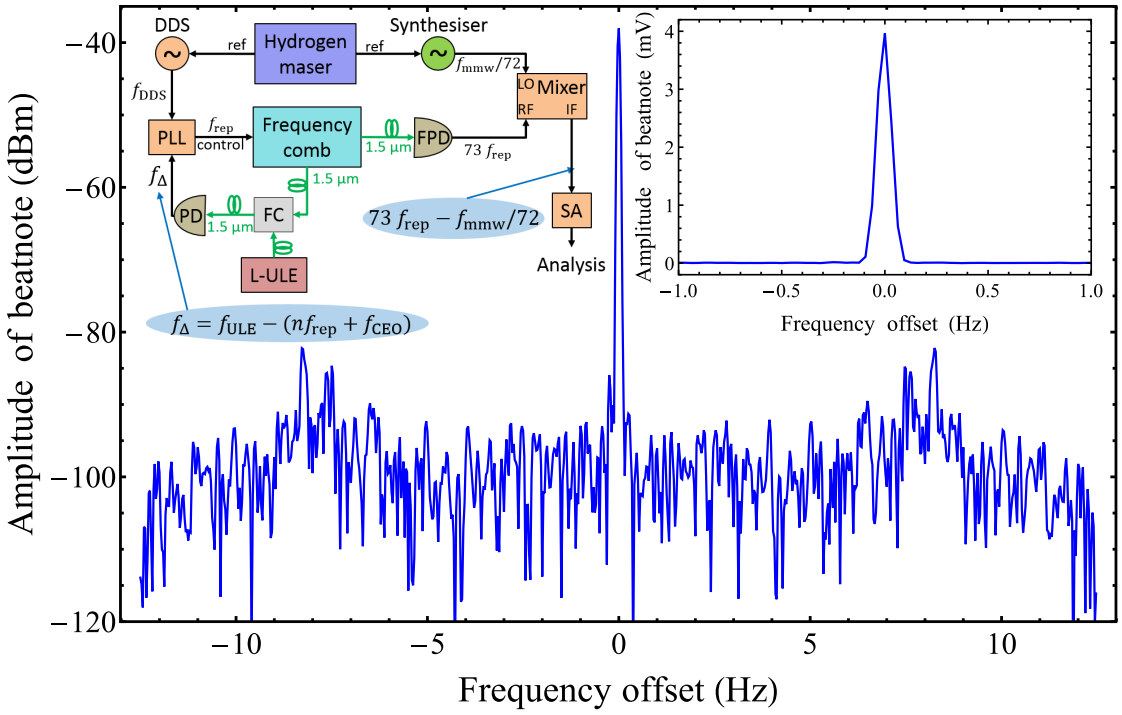

Supplementary Figure 2. **THz line-width characterization.** Main plot: power spectrum of the signal oscillating at the difference between an intermediate frequency close to $f_{\mathrm{mmw}}/72$ (synthesizer) and $f_{\mathrm{rep}} \times 73$, the 73$^{\mathrm{rd}}$ harmonic of the frequency comb's repetition rate. Full-width half-maximum is 86 mHz, with the resolution bandwidth being 31.25 mHz. Right inset: same as the main plot but the amplitude is in mV. Left inset: Schematic of the line-width measurement setup. FC: Fiber combiner, L-ULE: continuous-wave 1.5 μm semiconductor laser stabilized to an ultra-low expansion (ULE) glass cavity, PD: photo-detector, FPD: high-bandwidth photo-detector, SA: spectrum analyzer, PLL: phase lock feedback loop, DDS: direct digital synthesizer.

5. Publication 2

Reproduced from

S. Alighanbari, G.S. Giri, F. L. Constantin, V.I. Korobov, S. Schiller

Precise test of quantum electrodynamics and determination of fundamental constants with HD^+ *ions,*

Nature **581**, 152-158 (2020)

DOI: 10.1038/s41586-020-2261-5

Author's contributions

All authors contributed to the work. My contributions to this work are:

- Development and maintenance of the experimental setup.
- Design and setup of the DFB laser at 1.419 μm and integrating it into the experimental setup.
- Design, setup, and characterize the setup to control the THz power.
- I performed the spectroscopy together with Dr. G.S. Giri and Dr. F.L. Constantin.
- Analysis of the experimental data.
- Cooperation in manuscript editing.

Copyright and license notice

- To reproduce the contribution in whole or in part in any printed volume (book or thesis) of which they are the author(s).
- The author and any academic institution, where they work, at the time may reproduce the contribution for the purpose of course teaching.
- To reuse figures or tables created by the Author and contained in the Contribution in oral presentations and other works created by them.
- To post a copy of the contribution as accepted for publication after peer review (in locked Word processing file, of a PDF version thereof) on the Author's own web site, or the Author's institutional repository, or the Author's funding body's archive, six months after publication of the printed or online edition of the Journal, provided that they also link to the contribution on the publisher's website.
- Authors wishing to use the published version of their article for promotional use or on a web site must request in the normal way.
- For full paper portion: Authors of original research papers published by Springer Nature are encouraged to submit the author's version of the accepted, peer-reviewed manuscript to their relevant funding body's archive, for release six months after publication. In addition, authors are encouraged to archive their version of the manuscript in their institution's repositories (as well as their personal Web sites), also six months after original publication.

Precise test of quantum electrodynamics and determination of fundamental constants with HD^+ ions

https://doi.org/10.1038/s41586-020-2261-5

Received: 18 November 2018

Accepted: 12 February 2020

Published online: 06 May 2020

Check for updates

S. Alighanbari[1], G. S. Giri[1], F. L. Constantin[1,2], V. I. Korobov[3] & S. Schiller[1]✉

Bound three-body quantum systems are important for fundamental physics[1,2] because they enable tests of quantum electrodynamics theory and provide access to the fundamental constants of atomic physics and to nuclear properties. Molecular hydrogen ions, the simplest molecules, are representative of this class[3]. The metastability of the vibration–rotation levels in their ground electronic states offers the potential for extremely high spectroscopic resolution. Consequently, these systems provide independent access to the Rydberg constant (R_∞), the ratios of the electron mass to the proton mass (m_e/m_p) and of the electron mass to the deuteron mass (m_e/m_d), the proton and deuteron nuclear radii, and high-level tests of quantum electrodynamics[4]. Conventional spectroscopy techniques for molecular ions[5–14] have long been unable to provide precision competitive with that of ab initio theory, which has greatly improved in recent years[15]. Here we improve our rotational spectroscopy technique for a sympathetically cooled cluster of molecular ions stored in a linear radiofrequency trap[16] by nearly two orders in accuracy. We measured a set of hyperfine components of the fundamental rotational transition. An evaluation resulted in the most accurate test of a quantum-three-body prediction so far, at the level of 5×10^{-11}, limited by the current uncertainties of the fundamental constants. We determined the value of the fundamental constants combinations $R_\infty m_e(m_p^{-1} + m_d^{-1})$ and m_p/m_e with a fractional uncertainty of 2×10^{-11}, in agreement with, but more precise than, current Committee on Data for Science and Technology values. These results also provide strong evidence of the correctness of previous key high-precision measurements and a more than 20-fold stronger bound for a hypothetical fifth force between a proton and a deuteron.

Since the inception of quantum mechanics, the precise understanding of three-body systems has represented a challenging fundamental physics problem. Its detailed study, both theoretical and experimental, is an ongoing effort, with a strong rate of improvement. Different three-body systems (for example, the helium atom, lithium ion, helium-like ions, antiprotonic helium atom and molecular hydrogen ions (MHIs)) provide the opportunity to test our understanding of quantum physics at the highest levels, in particular, the theory of quantum electrodynamics (QED). In doing so, important fundamental constants of physics (such as the Rydberg constant R_∞, fine-structure constant α, electron mass m_e, proton mass m_p, deuteron mass m_d and antiproton mass) and particular nuclear properties, such as charge radii, electric quadrupole moments and charge-current moments, can be determined.

The MHIs (HD^+, H_2^+ and so on) are molecular three-body systems containing two heavy particles and one light particle (electron). The electronic ground state supports hundreds of metastable rotation–vibration levels. A small subset of them have been studied with different experimental techniques and concerning different aspects since the mid-1960s[5–14,17] (for an early review, see ref. [3]). Over the past decade, the MHIs have come into focus because of their relevance for the metrology of the particle masses[4,18–21]. These can be determined from rotation–vibration spectroscopic data, an approach independent of the established technique of mass spectrometry in ion traps. An additional opportunity is the determination of the Rydberg constant R_∞ and the proton charge radius, independently from the established technique of atomic hydrogen spectroscopy[22–24]. The precise value of these constants has been called into question in recent years in connection with the 'proton radius puzzle'[25], and therefore alternative and independent approaches for its determination are highly desirable.

The ab initio theory of the MHIs has made enormous progress in precision over the past 20 years[26–28], reducing the uncertainty by four orders of magnitude. It currently stands at 1.4×10^{-11} fractionally for the fundamental rotational transition frequency and 7×10^{-12} for

[1]Institut für Experimentalphysik, Heinrich-Heine-Universität Düsseldorf, Düsseldorf, Germany. [2]Laboratoire PhLAM CNRS UMR 8523, Université Lille 1, Villeneuve d'Ascq, France. [3]Bogoliubov Laboratory of Theoretical Physics, Joint Institute for Nuclear Research, Dubna, Russia. ✉e-mail: step.schiller@hhu.de

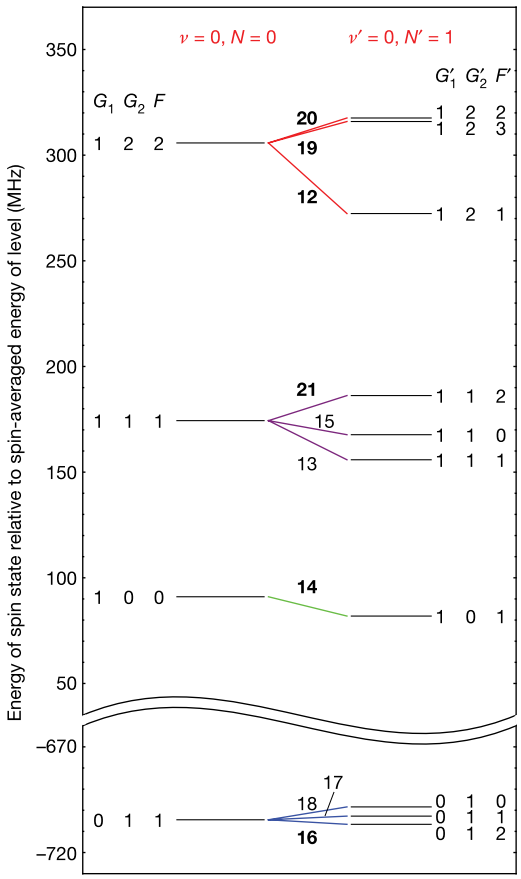

Fig. 1 | Energy diagram of the spin structures and favoured transitions. The left side shows the rovibrational ground level ($v = 0, N = 0$) and the right side shows the rotationally excited level ($v' = 0, N' = 1$). The magnetic field is zero. The spin states are labelled by the (in part approximate) quantum numbers (G_1, G_2 and F). The spin energies $E_{\mathrm{spin}}(v, N, G_1, G_2, F)$ and $E_{\mathrm{spin}}(v', N', G_1', G_2', F')$ are shown as thin black lines. Transitions ('hyperfine components') are numbered according to increasing values of $hf_{\mathrm{spin},i} = E_{\mathrm{spin}}(v', N', G_1', G_2', F') - E_{\mathrm{spin}}(v, N, G_1, G_2, F)$, including both favoured and weak transitions. The favoured electric-dipole transitions obey the selection rules $\Delta G_1 = 0$, $\Delta G_2 = 0$ and $\Delta F = 0, \pm 1$. The ten favoured transitions are shown by coloured lines. The rotational transition frequency of a particular hyperfine component is $f_i = f_{\mathrm{spin\text{-}avg}} + f_{\mathrm{spin},i}$, with $f_{\mathrm{spin\text{-}avg}} \approx 1.314$ THz and, for favoured transitions, $f_{\mathrm{spin},i} \approx \mathcal{O}(10\ \mathrm{MHz})$. The six components measured in this work are shown by bold numbers in the diagram.

vibrational transitions, ignoring spin-structure effects[15]. These uncertainties are smaller than the current (Committee on Data for Science and Technology (CODATA) 2018[29]) uncertainties of the masses m_e, m_p and m_d, pointing at the potential of MHI spectroscopy for the metrology of fundamental constants. Here we perform precision spectroscopy of the fundamental rotational transition of HD^+. Fundamental constants can be derived by comparison of the measured transition frequency $f^{(\mathrm{exp})}$ with the prediction $f^{(\mathrm{theor})} = 2cR_\infty(m_e/\mu_{pd})F^{(\mathrm{theor})}_{\mathrm{spin\text{-}avg}}$, where $\mu_{pd} = m_p m_d/(m_p + m_d)$ is the reduced nuclear mass, c is the speed of light, and $F^{(\mathrm{theor})}_{\mathrm{spin\text{-}avg}} = 0.244591781951(33)_{\mathrm{theory}}(11)_{\mathrm{CODATA2018}}$ is a dimensionless normalized frequency computed ab initio, neglecting the hyperfine interactions. $F^{(\mathrm{theor})}_{\mathrm{spin\text{-}avg}}$ encompasses—besides the dominant non-relativistic (Schrödinger) part—essential relativistic, nuclear-size-related and radiative contributions. The nuclear charge radius values (r_p, r_d) are from the CODATA 2018 adjustment that took into account the muonic hydrogen spectroscopy results. Whereas the uncertainty of $F^{(\mathrm{theor})}_{\mathrm{spin\text{-}avg}}$ due to theory is 1.4×10^{-11}, the uncertainty originating from the CODATA 2018 uncertainties of the fundamental constants is smaller (4.4×10^{-12}), and stems from the uncertainties of r_p and r_d.

Apart from a matching comparison with a 50-year-old radiofrequency (RF) spectroscopy benchmark result on H_2^+ (ref. [17]), the ab initio theory could not be tested experimentally at a competitive level, owing to lack of suitable experimental methods. With a few exceptions, the spectroscopic resolution in rotational and vibrational spectroscopy of molecular ions in general has been limited by Doppler broadening. Although this broadening can be minimized by trapping molecular ions in an RF trap and sympathetically cooling them by atomic ions, their effective temperature remains of the order of 10 mK, leading to Doppler-limited linewidths not lower than 5×10^{-8} fractionally[12]. Unresolved hyperfine structure increases linewidths again[11,14], posing a roadblock for testing theory at more precise levels.

Only recently, new methods have been introduced that open up the next generation of precision experiments[30,31]. Specifically for rotational spectroscopy, we have shown[16] that sub-Doppler spectroscopy is possible for a radiation propagation direction transverse to the 'long' axis of the molecular ion cluster (trapped ion cluster transverse excitation spectroscopy, TICTES). The small motional amplitude of the ions along the spectroscopy wave propagation direction compared with its wavelength allows reaching the Lamb–Dicke regime. In the first demonstration[16], a fractional line resolution of 1×10^{-9} (full-width at half-maximum (FWHM) relative to absolute frequency) was obtained.

Here we improve the resolution of TICTES by more than two orders of magnitude. This enables a detailed direct study of the fundamental rotational transition of HD^+, whose hyperfine spectrum and Zeeman splittings are resolved and systematic effects are determined.

Comparison with our improved theory and a new analysis method allows us to establish agreement between theory and experiment at the 5×10^{-11} level (limited by CODATA 2018 uncertainties), not only representing the most accurate test of a molecular three-body system so far, but also demonstrating the power of TICTES, a method applicable to a plethora of molecular ions.

The experiment

We performed spectroscopy of the fundamental rotational transition $(v, N) = (0, 0) \rightarrow (v, N') = (0, 1)$ at 1.3 THz. v and N are the vibrational and rotational quantum numbers, respectively. See Extended Data Fig. 1 for the experimental scheme. The fractional population of HD^+ ions in the lower spectroscopy state (0, 0) is enhanced using rotational laser cooling[32]. The transition is detected by resonance-enhanced multiphoton dissociation (REMPD)[33]. See Extended Data Fig. 2 for typical data. To achieve a spectroscopy wave with narrow linewidth, high frequency stability and high accuracy, a GPS-monitored, hydrogen-maser-referenced terahertz frequency multiplier is used[16,34]. Compared with our previous work[16], we performed measurements for different magnetic-, electric- and light-field strengths, and minimized the terahertz wave power. These extensive measurements were enabled by improvements in the long-term stability of the apparatus and improved detection schemes.

The HD^+ molecule has spin structure in both the lower and the upper rotational levels, due to the presence of (1) the intrinsic spins of the electron ($\mathbf{s}_e$), proton ($\mathbf{I}_p$) and deuteron ($\mathbf{I}_d$), and (2) of the rotational angular momentum $\mathbf{N}$ (Fig. 1). For state description, we use the angular momentum coupling scheme $\mathbf{G}_1 = \mathbf{s}_e + \mathbf{I}_p$, $\mathbf{G}_2 = \mathbf{G}_1 + \mathbf{I}_d$, $\mathbf{F} = \mathbf{G}_2 + \mathbf{N}$ (ref. [35]), where $\mathbf{F}$ is the total angular momentum. The rotational transition encompasses 32 hyperfine components f_i in absence of a magnetic field; of these, ten are favoured (strong) (Fig. 1). Their frequencies $f_{12}, \ldots, f_{21}$ lie within a range of 45 MHz around $f_{\mathrm{spin\text{-}avg}} \approx 1.314$ THz. Averaging over these ten components with appropriate weights yields the 'spin-averaged' frequency $f_{\mathrm{spin\text{-}avg}}$ (ref. [36]). Here we measured six hyperfine components, $f_{12}, f_{14}, f_{16}, f_{19}, f_{20}$ and f_{21}.

Figure 2 shows the measured transitions, in the presence of a small magnetic field. The different linewidths are due to the different terahertz wave intensities used and due to the different transition dipole moments. Line 19 includes the two transitions between states of

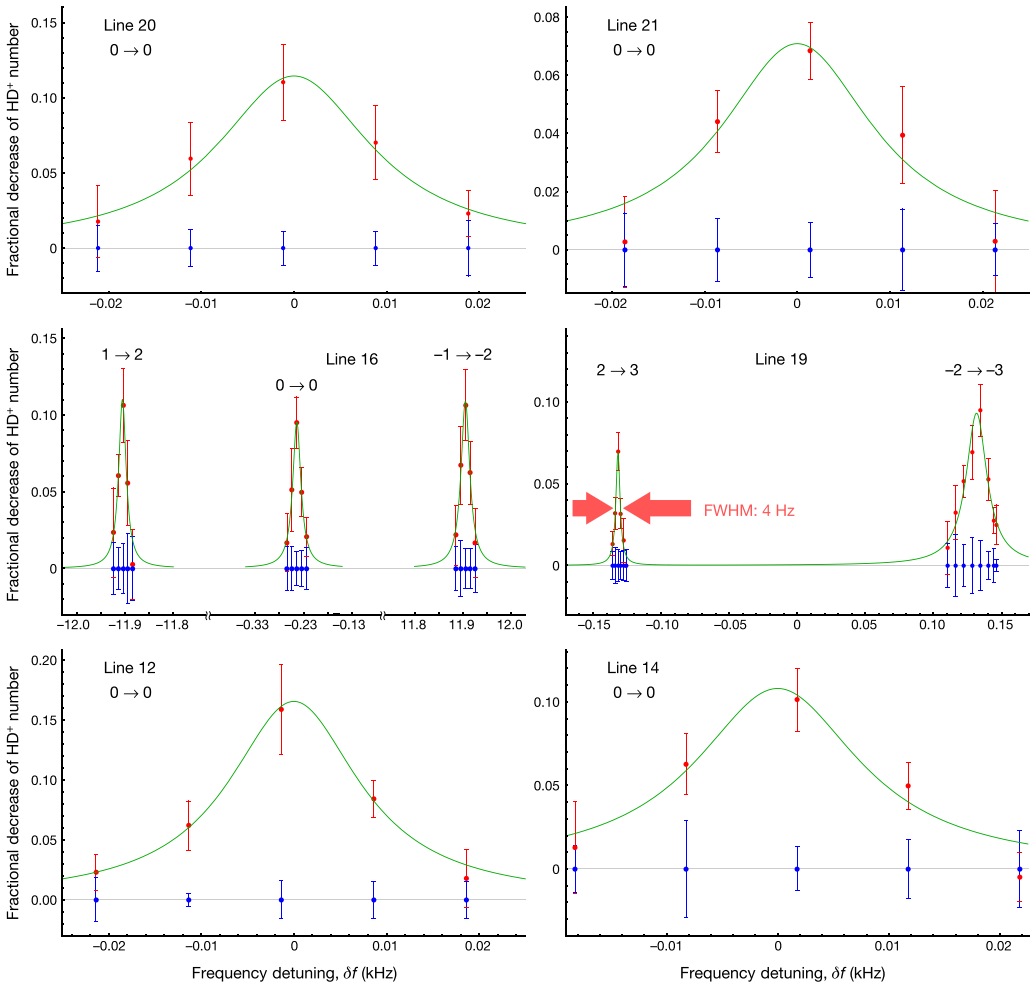

Fig. 2 | Hyperfine components of the fundamental rotational transition of HD^+ at 1.3 THz. The red and blue points indicate the cases of terahertz radiation on and off (background), respectively. Green lines are Lorentzian fits. The Zeeman components are indicated by the expression $m_F \rightarrow m'_F$. The terahertz wave intensity varied and was less than 10 nW mm^{-2}. The zero of the frequency scales are set to coincide with the fitted line maxima or means. At each frequency setting, the red and blue data points are both shown with an offset equal to the value of the blue point. Each error bar represents the standard deviation of the mean. The nominal magnetic field is $B_{nom} \approx 30$ μT and the trap RF amplitude is approximately 190 V.

maximum total angular momentum F and maximum projection quantum number m_F, $(F = 2, m_F = \pm 2) \rightarrow (F' = 3, m'_F = \pm 3)$, denoted by $19_{\pm}$, whose Zeeman shift is purely linear, according to theory[37]. The two components were observed at lower resolution and with unresolved Zeeman splitting in ref. [16]. One Zeeman component (19_-) measured at particularly low intensity exhibited a full linewidth of 4 Hz, or 3×10^{-12} fractionally, indicating the potential of the experimental technique in the context of mass determination. For line 16, we measured a Zeeman pair $m_F = \pm 1 \rightarrow m'_F = \pm 2$ (denoted by $16_{\pm}$), split by a linear Zeeman shift and weakly shifted by a common quadratic Zeeman shift, and a component 16_0: $m_F = 0 \rightarrow m'_F = 0$, which exhibits a moderate quadratic Zeeman shift[37]. For the remaining lines, we measured only the $m_F = 0 \rightarrow m'_F = 0$ Zeeman components.

Systematic shifts

For an accurate comparison between theoretical transition frequencies (computed assuming an absence of perturbing fields) and experimental values (measured in presence of such fields), the systematic shifts must be taken into account. We determined them experimentally. The dominant systematic effect is the Zeeman shift. For a nominal RF drive amplitude, we measured the frequency shifts of all considered components as a function of applied magnetic field. The shifts are consistent with the theoretically calculated ones, except for small deviations. We obtained the transition frequencies corresponding to zero magnetic field by extrapolation.

The quadratic Stark shift due to the ion trap's electric field $E(t)$, oscillating at comparatively low (RF) frequency and leading to a mean-square value $\langle E(t)^2 \rangle$, is a second shift, of lower magnitude. For a nominal magnetic field, we measured the frequency shifts of all considered components for a set of trap RF amplitudes. All shifts were found to increase with amplitude, with values in the range of 0.5 to 1.2 kHz kV^{-2}. We determined the frequencies corresponding to zero RF-field amplitude by extrapolation. For additional information, see Methods and Extended Data Fig. 3.

Table 1 presents the experimental transition frequencies $f_i^{(exp)}$ (corrected for the systematic shifts) and their uncertainties. The uncertainties result from the number of frequency measurements, which were taken at different RF drive settings and different magnetic-field settings, and the statistical uncertainties of the frequency measurements. The lowest experimental uncertainty is achieved for line 16, $u(f_{16}^{(exp)}) = 0.017$ kHz (fractional uncertainty $u_r = 1.3 \times 10^{-11}$). This represents the best performance level of the TICTES technique as currently implemented.

Theory

For a compelling comparison between theory and the experimental data, highly precise theoretical predictions and qualified estimates of

Table 1 | Experimental rotational frequencies, and comparison with theoretical ab initio frequencies

Line i	$G_1G_2F \rightarrow G_1'G_2'F'$	$f_i^{(\mathrm{exp})}$	$u(f_i^{(\mathrm{exp})})$	$f_i^{(\mathrm{theor})}$	$u(f_{\mathrm{spin},i}^{(\mathrm{theor})})$	$u(f_{\mathrm{spin\text{-}avg}}^{(\mathrm{theor})})$	$u_{\mathrm{CODATA}}(f_i^{(\mathrm{theor})})$
12	122 → 121	1314892544.276	0.040	1314892544.23	1.2	0.018	0.061
14	100 → 101	1314916678.487	0.064	1314916678.74	1.3	0.018	0.061
16	011 → 012	1314923618.028	0.017	1314923617.94	0.20	0.018	0.061
19	122 → 123	1314935827.695	0.037	1314935827.58	1.2	0.018	0.061
20	122 → 122	1314937488.614	0.060	1314937488.80	1.4	0.018	0.061
21	111 → 112	1314937540.762	0.046	1314937540.61	0.73	0.018	0.061

Uncertainties are denoted by u. Frequency values are in kHz. The theoretical values $f_i^{(\mathrm{theor})}$ were computed using CODATA 2018 constants. The last three columns show the three contributions to the total uncertainty of $f_i^{(\mathrm{theor})}$. Line 16 offers the most stringent comparison, due to its comparatively small theory uncertainty.

their uncertainties are essential. The ab initio transition frequency $f_i^{(\mathrm{theor})}$ of each hyperfine component i is the sum of two contributions, $f_{\mathrm{spin\text{-}avg}}^{(\mathrm{theor})} + f_{\mathrm{spin},i}^{(\mathrm{theor})}$. The dominant contribution is

$$f_{\mathrm{spin\text{-}avg}}^{(\mathrm{theor})} = 1{,}314{,}925{,}752.896(18)_{\mathrm{theory}}(61)_{\mathrm{CODATA2018}}\ \mathrm{kHz} \qquad (1)$$

computed[15] including all relativistic and radiative corrections up to the relative order α^5 and partially including contributions of the order α^6 (Table 2). The value $f_{\mathrm{spin\text{-}avg}}^{(\mathrm{theor})}$ is updated from the value reported in ref. [16] by using CODATA 2018[29] updates of the Rydberg constant, the particle masses (in atomic mass units, u), the proton charge radius and the deuteron charge radius. The theory uncertainty is estimated as $u(f_{\mathrm{spin\text{-}avg}}^{(\mathrm{theor})}) \approx 0.018$ kHz, while the larger CODATA 2018 uncertainty, $u_{\mathrm{CODATA2018}}(f_{\mathrm{spin\text{-}avg}}^{(\mathrm{theor})}) \approx 0.061$ kHz, is dominated by the uncertainties of the particle masses.

A spin frequency contribution $f_{\mathrm{spin},i}^{(\mathrm{theor})}$ is the difference of the spin structure energies of the upper and lower spin states involved in the transition. For the favoured transitions measured here, the values of $f_{\mathrm{spin},i}^{(\mathrm{theor})}$ are of the order of 10 MHz. The spin contributions are computed by diagonalizing the Breit–Pauli spin Hamiltonian of ref. [35]. The various terms of this Hamiltonian are proportional to coefficients $\mathcal{E}_k$, $\mathcal{E}_k'$, computed ab initio (Extended Data Table 1). The spin Hamiltonian of the $N=0$ level necessitates two coefficients, $\mathcal{E}_4$ and $\mathcal{E}_5$, while the $N=1$ level necessitates nine, $\mathcal{E}_1', \ldots, \mathcal{E}_9'$.

The coefficients $\mathcal{E}_4$, $\mathcal{E}_4'$ and $\mathcal{E}_5$, $\mathcal{E}_5'$ describe the dominant $\mathbf{s}_e\cdot\mathbf{I}_p$ and $\mathbf{s}_e\cdot\mathbf{I}_d$ interactions, respectively, and have been calculated with high theoretical precision, including all corrections of the order $\alpha^2 E_F/h$ and the leading corrections of the order $\alpha^3 E_F/h$, where $E_F \approx h(1.4\ \mathrm{GHz})$ is the Fermi contact energy for the hyperfine splitting in atomic hydrogen and h is Planck's constant[38]. The fractional theoretical uncertainties of these spin Hamiltonian coefficients are of the order α^3; they are estimated as $\varepsilon_F = 1\times10^{-6}$. Furthermore, the signed theory errors are expected to be nearly equal: $\Delta\mathcal{E}_4^{(\mathrm{theor})} \approx \Delta\mathcal{E}_4'^{(\mathrm{theor})}$ and $\Delta\mathcal{E}_5^{(\mathrm{theor})} \approx \Delta\mathcal{E}_5'^{(\mathrm{theor})}$ (Methods).

The other spin coefficients, $\mathcal{E}_1'$, $\mathcal{E}_2'$, $\mathcal{E}_3'$, $\mathcal{E}_6'$, $\mathcal{E}_7'$, $\mathcal{E}_8'$ and $\mathcal{E}_9'$, have been obtained within the Breit–Pauli approximation. We computed them using our most precise non-relativistic non-adiabatic molecular variational wave functions (Methods, Extended Data Table 1). The omitted terms are of the relative order α^2. References[38,39] lead us to estimate a common fractional theory uncertainty equal to $\alpha^2 = \varepsilon_0 \approx 5\times10^{-5}$.

To determine the impact of the theory uncertainty of a particular Hamiltonian coefficient on a particular spin frequency, we introduce the quantities $\gamma_{i,k}'\Delta\mathcal{E}_k'^{(\mathrm{theor})}$, with the derivatives $\gamma_{i,k}' = \partial E_{\mathrm{spin},i}'(\mathcal{E}_1', \ldots, \mathcal{E}_9')/\partial\mathcal{E}_k'$ relevant for the upper spin level and similarly for the lower spin level. The γ values are reported in Extended Data Table 1. Assuming equal theory errors for the pairs $(\mathcal{E}_4, \mathcal{E}_4')$ and $(\mathcal{E}_5, \mathcal{E}_5')$, we conservatively estimate the total theory uncertainty of the spin-frequency contribution with the following expression

$$u(f_{\mathrm{spin},i}^{(\mathrm{theor})}) = \varepsilon_F \sum_{4,5} |\gamma_{i,k}'\mathcal{E}_k' - \gamma_{i,k}\mathcal{E}_k| + \varepsilon_0 \sum_{1,2,3,6,7,8,9} |\gamma_{i,k}'\mathcal{E}_k'|$$

The form of the first sum embodies the assumption of equal fractional errors and correlation, $\Delta\mathcal{E}_{4,5}^{(\mathrm{theor})} = \delta_{4,5}\varepsilon_F\mathcal{E}_{4,5}$, $\Delta\mathcal{E}_{4,5}'^{(\mathrm{theor})} = \delta_{4,5}\varepsilon_F\mathcal{E}_{4,5}'$, with $\delta_4 = 1$ or -1, $\delta_5 = 1$ or -1. The similarities $\gamma_4 \approx \gamma_4'$ and $\gamma_5 \approx \gamma_5'$ for the lower and upper rotational levels then lead to a strong suppression of the contributions related to the theory errors of $\mathcal{E}_4$, $\mathcal{E}_4'$, $\mathcal{E}_5$ and $\mathcal{E}_5'$. This results in the spin-frequency uncertainties shown in Table 1 (column 6). They dominate the total uncertainty of the transition frequencies $f_i^{(\mathrm{theor})}$.

Comparison between theory and experiment

Table 1 presents the comparison between the theory and experimental data of the individual hyperfine components of the rotational

Table 2 | Contributions to the ab initio spin-averaged rotational frequency $f_{\mathrm{spin\text{-}avg}}^{(\mathrm{theor})}$

Term	Relative order	Contribution (kHz)	Origin
$f^{(0)}$	1	1,314,886,776.526	Solution of three-body Schrödinger equation
$f^{(2)}$	α^2	48,416.268	Relativistic corrections in Breit–Pauli approximation; nuclear radii
$f^{(3)}$	α^3	−9,378.119	Leading-order radiative corrections (for example, leading-order Lamb shift, anomalous magnetic moment)
$f^{(4)}$	α^4	−65.631(2)	One-loop, two-loop radiative corrections; relativistic corrections
$f^{(5)}$	α^5	3.923(3)	Radiative corrections up to three-loop diagrams; Wichman–Kroll contribution
$f^{(6)}$	α^6	−0.070(18)	Higher-order radiative corrections
Total $f_{\mathrm{spin\text{-}avg}}^{(\mathrm{theor})}$		1,314,925,752.896(18)	

The values were calculated using CODATA 2018 values of the fundamental constants. The main contribution $f^{(0)}$ is of order $cR_\infty(m_e/\mu_{pd})$. Recoil corrections (due to finite masses of nuclei) are included fully at the order α^2; the leading recoil corrections proportional to m_e/m_p or m_e/m_d are included at the order α^3. Contributions due to the finite size of the nuclei are included in the $f^{(2)}$ term[15]. The one-loop contribution from μ^+–μ^- vacuum polarization is included in $f^{(3)}$. The estimated fractional theory uncertainty of the spin-averaged frequency is $u_r = 1.4\times10^{-11}$ ($u(f_{\mathrm{spin\text{-}avg}}^{(\mathrm{theor})}) = 0.018$ kHz). The impact of the fundamental constants' uncertainties is given in the text. The change in the value of $f^{(0)}$ from CODATA 2014 to CODATA 2018 has contributions of −0.041 kHz from the Rydberg constant adjustment and 0.213 kHz from the particle masses adjustments. The change in the value of $f^{(2)}$ due to the proton and deuteron charge radii adjustments is 0.104 kHz.

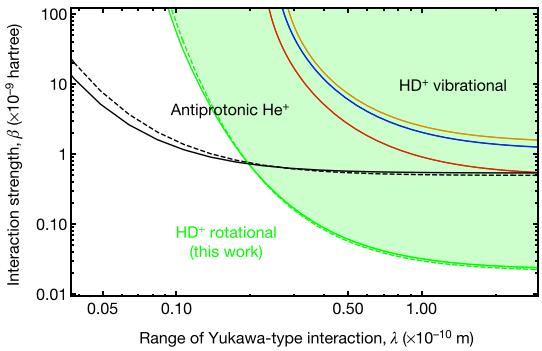

Fig. 3 | Exclusion plot (95% confidence limit) for a Yukawa-type interaction between a proton and a deuteron, deduced from spectroscopy of MHIs. The parameter space above the lines is excluded. The assumed interaction is $V_5(R) = \beta N_1 N_2 \exp(-R/\lambda)/R$, where R is the proton–deuteron distance, λ is the interaction range, $N_1 = 1$ and $N_2 = 2$ are the nuclear mass numbers, and β is the interaction strength. Green lines, this work (full green, numerical; dashed green, analytical, equation (4) in Methods); red line, ref. [14]; blue line, ref. [11]; orange line, ref. [12]. For comparison, the black lines show the limits for the interaction between the antiproton and the helium-4 nucleus, obtained from two different transitions[46]. See Methods for details.

transition. We find agreement for all lines, within the combined uncertainties of theory and experiment. The agreement is most stringent for line 16, and it is limited by the prediction's total uncertainty $u(f_{16}^{(\mathrm{theor})}) \approx 0.21$ kHz , or 1.5×10^{-10} fractionally. The agreement is far less stringent than the roughly ten times lower experimental uncertainty would allow. The precise experimental value can therefore serve as a benchmark for tests of future improved spin-structure calculations.

Frequencies related to only the spin structure of the molecule can be obtained from rotational frequency differences $\Delta f_{i,j} = f_i - f_j = f_{\mathrm{spin},i} - f_{\mathrm{spin},j}$, where the spin-averaged frequency is cancelled. All deviations between experiment and theory are smaller than 0.42 kHz in magnitude and are well within the theory uncertainties (CODATA 2018 uncertainties are not relevant here). The most stringent theory–experiment agreement is found for $\Delta f_{21,19}$, within the roughly 0.7-kHz theory uncertainty, but ten times less stringent than the experimental uncertainty would allow.

In view of the relatively large uncertainties for $f_{\mathrm{spin},i}^{(\mathrm{theor})}$ above, we introduce a novel way of comparing experiment with theory, using composite frequencies defined as $f_c = \sum_i b_i f_i$, with appropriate weights b_i. We aim to find composite frequencies with small theory uncertainty, and therefore must suppress the contribution of the spin energies' uncertainties without suppressing the spin-averaged energies that give rise to $f_{\mathrm{spin\text{-}avg}}$. The latter requirement is satisfied by imposing the 'normalization' condition $\sum_i b_i = 1$, so that $f_c = f_{\mathrm{spin\text{-}avg}} + f_{\mathrm{spin,c}}$, with $f_{\mathrm{spin,c}} = \sum_i b_i f_{\mathrm{spin},i}$. The former requirement is implemented by finding the composite frequency that minimizes the theory uncertainty. We use a conservative measure of theory uncertainty that does not assume any relationship between the theory errors of $(\mathcal{E}_4, \mathcal{E}'_4)$ and of $(\mathcal{E}_5, \mathcal{E}'_5)$: $\bar{u}(f_{\mathrm{spin,c}}^{(\mathrm{theor})}) = \sum_k (|\sum_i b_i \gamma'_{i,k} \mathcal{E}'_k| + |\sum_i b_i \gamma_{i,k} \mathcal{E}_k|)\varepsilon_k$. The solution $\{b_i\}$ is found numerically (see 'Composite frequencies' in Methods), $f_{\mathrm{spin,c}}^{(\mathrm{theor})}(\{b_i\}) = 934.635$ kHz, with negligible uncertainty $\bar{u}(f_{\mathrm{spin,c}}^{(\mathrm{theor})}) = 0.001$ kHz. We note that this approach for eliminating the spin-energy-related uncertainty is complementary to the more general method recently proposed by some of us in ref. [36], where the composite frequency is equal to $f_{\mathrm{spin\text{-}avg}}$.

From the experimental composite frequency, we deduce the experimental spin-averaged frequency

$$f_{\mathrm{spin\text{-}avg}}^{(\mathrm{exp})} = f_c^{(\mathrm{exp})}(\{b_i\}) - f_{\mathrm{spin,c}}^{(\mathrm{theor})}(\{b_i\}) = 1{,}314{,}925{,}752.910(17)_{\mathrm{exp}}\ \mathrm{kHz} \quad (2)$$

($u_r = 1.3 \times 10^{-11}$). The theory uncertainty (via $f_{\mathrm{spin,c}}^{(\mathrm{theor})}$) is negligible and is therefore not indicated.

QED test and determination of fundamental constants

A comparison of equations (1) and (2) indicates that our experiment and theory achieve a successful test of three-body physics with a combined fractional uncertainty of 4.8×10^{-11} (0.064 kHz), limited by CODATA 2018 uncertainties. Comparing the total uncertainty of $f_{\mathrm{spin\text{-}avg}}^{(\mathrm{theor})}$ with the QED contributions listed in Table 2, we see that it is close to the QED contribution of highest calculated relative order, $f^{(6)} \approx 0.070(18)$ kHz. Therefore, more specifically, our experiment furnishes a test of QED at the relative order of α^6. According to theory, the contributions to $f^{(2)}$ stemming from the finite proton root-mean-square charge radius r_p and the deuteron charge radius r_d with their CODATA 2018 uncertainties are −0.644(3) kHz and −4.120(3) kHz, respectively. The sum of these contributions is put in evidence by our experiment–theory comparison, with a fractional uncertainty of 1.4%.

Our experiment–theory agreement is obtained when including in the hyperfine structure calculation the contribution of the deuteron quadrupole moment Q_d, quantified by the coefficient $\mathcal{E}'_9 \propto Q_d$. This contribution is observed here in an MHI for the first time. From the measured hyperfine structure we can extract, independently of any QED contributions, a value for Q_d with 1.5% fractional uncertainty (Methods).

The experiment–theory agreement can also be used to set improved limits to the hypothetical existence of a spin-averaged fifth force between a proton and a deuteron (Fig. 3, Methods). Compared with previous bounds from MHI spectroscopy, the improvement is a factor of 21 or more for force ranges $\lambda > 1$ Å.

We can obtain the combination $R_\infty m_e/\mu_{pd}$ of fundamental constants from any of the measured rotational frequencies $f_i^{(\mathrm{exp})}$ and the corresponding ab initio value $f_i^{(\mathrm{theor})}$. However, the highest precision is obtained by instead choosing the composite frequency f_c or the spin-averaged frequency, because their spin-structure theory uncertainty is suppressed to a negligible level. Furthermore, we note that the ab initio calculation is performed assuming trial values for m_e/m_p and m_e/m_d, and naturally yields the rotational frequencies (independent of Rydberg constant value), $f_i^{(\mathrm{theor,n})} \approx 1.998\ldots \times 10^{-4}$ atomic units. From these, we compute the scaled, dimensionless values $F_i^{(\mathrm{theor})} = (\mu_{pd}/m_e) f_i^{(\mathrm{theor,n})}/1$ atomic unit. These have an important dependence on r_p and r_d. The dependence on other fundamental constants is weak, compared with their uncertainties, the largest of which is $\partial \ln F_i^{(\mathrm{theor})}/\partial \ln(m_e/\mu_{pd}) \approx 4 \times 10^{-3}$. Because of this smallness, it is consistent to use the CODATA 2018 values of the fundamental constants in the computation of $F_i^{(\mathrm{theor})}$. This results in

$$R_\infty m_e (m_p^{-1} + m_d^{-1}) = \frac{f_{\mathrm{spin\text{-}avg}}^{(\mathrm{exp})}}{2c F_{\mathrm{spin\text{-}avg}}^{(\mathrm{theor})}} = 8{,}966.20515050(12)_{\mathrm{exp}}(12)_{\mathrm{theor}}(4)_{\mathrm{CODATA2018}}\ \mathrm{m}^{-1} \quad (3)$$

($u_r = 2.0 \times 10^{-11}$), where the third uncertainty is due to the proton and deuteron radius uncertainties. The value is in agreement with the CODATA 2018 value of 8,966.20515041(41) m^{-1} ($u_r = 4.6 \times 10^{-11}$) (Fig. 4). It results from atomic hydrogen spectroscopy (providing R_∞), hydrogen-like ion spin resonance spectroscopy (m_e) and Penning trap mass spectrometry (m_p, m_d). Our result's total uncertainty is smaller by a factor of 2.4 compared with the CODATA 2018 value and ranks among the most precise measurements of a fundamental constant combination.

Owing to the comparatively small CODATA 2018 uncertainty of R_∞, our improved uncertainty impacts mostly the mass ratio sum $m_e(m_p^{-1} + m_d^{-1})$. Combining equation (3) with the CODATA 2018 values of R_∞, m_e/u and m_d/u yields the proton mass

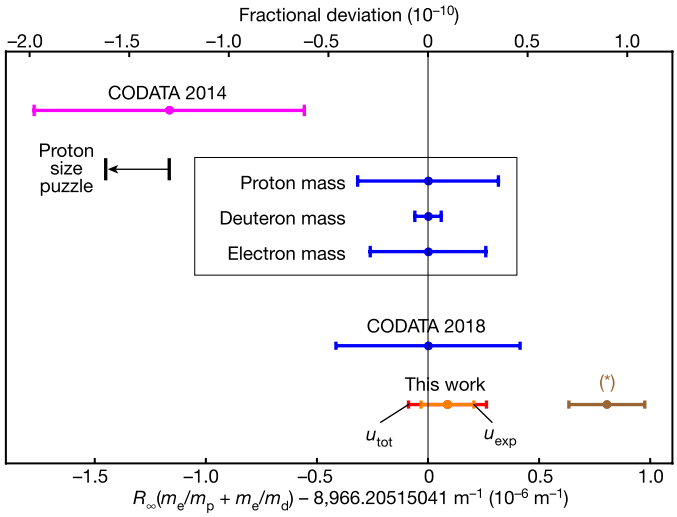

Fig. 4 | Comparison of results of this work with literature values. In the inner box, we plot the error bars for the CODATA 2018 $R_\infty(m_e/m_p + m_e/m_d)$ for the hypothetical cases that the uncertainties of all contributing constants were zero, except for the named constant. The black arrow indicates the shift of the CODATA 2014 value for a change $\Delta R_\infty = -0.00035\ m^{-1}$ corresponding to the 'proton size puzzle'[47]. The brown data point (*) shows the result of the present work when the CODATA 2014 values of r_p and r_d are used in $f^{(theor)}_{spin\text{-}avg}$, instead of the CODATA 2018 values resulting from muonic hydrogen spectroscopy.

$$m_p/u = 1.007276466605(20)_{exp}(21)_{theor}(45)_{CODATA2018}$$

in excellent agreement with the recent most precise direct measurement[40]

$$m_p/u = 1.007276466598(16)_{stat}(29)_{syst}$$

Taking into account a recent Penning trap measurement of m_d/m_p (ref. [41]), we also obtain the proton-to-electron mass ratio

$$m_p/m_e = 1,836.152673449(24)_{exp}(25)_{theor}(13)_{CODATA2018,Fink-Myers}$$

($u_r = 2.0 \times 10^{-11}$) in agreement but approximately two times more accurate than the most precise value, obtained by combining two published measurements in Penning traps[40,42]: $m_p/m_e = 1,836.152673374(78)_{exp}$.

Conclusion

The performance of the recently introduced TICTES technique for rotational spectroscopy has been improved by more than two orders in both resolution and accuracy, reaching a fractional FWHM linewidth of 3×10^{-12} and a fractional uncertainty of 1.3×10^{-11}. This vastly higher performance compared with traditional techniques can be of general relevance to the field of precision molecular physics.

Precise measurements of several rotational hyperfine components of HD^+ and suppression of the impact of the limited accuracy of the ab initio theory of the spin structure allowed us to establish agreement between experiment and theory at the 5×10^{-11} level, limited by uncertainties of the CODATA 2018 fundamental constants. To the best of our knowledge, this represents the most accurate test of a molecular physics prediction to date and also provides the most accurate experiment–theory comparison for any three-body quantum system[2,43–45]. Specifically, we confirmed the combination of the QED contributions of α^5 and α^6 relative order, of the proton finite size contribution and of the deuteron finite size contribution, with uncertainty equal to 0.7% of the total contribution. A strongly improved upper bound for a new force between a proton and a deuteron was set.

Spin-energy differences were experimentally determined with three orders smaller uncertainty than previously[12]. The best (effective) line resolution for spin energy is one order higher and the accuracy is 30 times higher than the benchmark experiment on the spin structure of H_2^+, which has stood unchallenged for 50 years. The spin-energy predictions were confirmed within the uncertainties of the theory predictions, the smallest uncertainty being 0.7 kHz. As the experimental uncertainties are much lower, the obtained spin-energy data offer new benchmark values for future improved ab initio theory of the spin structure.

We deduced the combinations $R_\infty m_e(m_p^{-1} + m_d^{-1})$ and m_p/m_e of fundamental constants with 2.0×10^{-11} fractional uncertainty, 2.4 and 3.0 times smaller, respectively, than the CODATA 2018 uncertainties. The proton mass in atomic mass units was deduced with the same uncertainty as in CODATA 2018. Interestingly, for the first time, fundamental constants have been determined with competitive uncertainty making use of the rotational motion of a physical system.

Our result also provides independent evidence of the correctness of some of the most precise measurements in atomic and particle physics: Rydberg constant determination via hydrogen spectroscopy, electron mass determination via the bound-electron g-factor, and proton mass and deuteron mass determination via cyclotron motion. Our measurement on a three-body quantum system thus provides an independent link between these one- and two-body systems. The substantial changes introduced in the CODATA 2018 adjustments of the fundamental constants are confirmed. In particular, the predicted HD^+ transition frequency is shifted by 0.063 kHz when the CODATA 2014 proton root-mean-square charge radius and Rydberg constant are replaced by the values deduced from the muonic hydrogen experiment (as in CODATA 2018). Our experimental frequency is consistent with the prediction based on these most recent values, within the combined uncertainties from experiment (0.017 kHz), theory (0.018 kHz) and masses (0.061 kHz).

Beyond the present results, our work has important implications for the near future. First, we suppose that in the spectroscopy of vibrational transitions a similar absolute systematic uncertainty can be achieved as in rotational spectroscopy, because the systematic shifts will not increase substantially with transition frequency. Indeed, the shifts depend on the size of the coefficients of appropriate Hamiltonians, and these coefficients do not vary substantially between the levels. If an optical spectroscopic technique with spectral resolution at the 10-Hz level becomes available, total experimental uncertainties at the 10^{-13} to 10^{-14} level could come into reach. Second, our composite frequency approach obviates the need for a more precise spin-structure theory, both for rotational and vibrational transitions. Therefore, more precise QED calculations of the spin-averaged rotational and vibrational frequencies are both sufficient and well worth pursuing. If this challenging programme is successful, the precision of fundamental constants derived from HD^+ spectroscopy will further improve. Specifically, the combination of rotational and vibrational spectroscopy results and ab initio theory will eventually allow the determination of the fundamental constants R_∞, m_e/μ_{pd}, r_p and r_d independently rather than in combination, with accuracies competitive with or better than CODATA 2018, and testing QED without limitation by the current determination of the fundamental constants.

Online content

Any methods, additional references, Nature Research reporting summaries, source data, extended data, supplementary information, acknowledgements, peer review information; details of author contributions and competing interests; and statements of data and code availability are available at https://doi.org/10.1038/s41586-020-2261-5.

1. Karshenboim, S. G. (ed.) *Precision Physics of Simple Atoms and Molecules* (Springer-Verlag, 2008).
2. Pachucki, K., Patkóš, V. & Yerokhin, V. A. Testing fundamental interactions on the helium atom. *Phys. Rev. A* **95**, 062510 (2017).
3. Leach, C. A. & Moss, R. E. Spectroscopy and quantum mechanics of the hydrogen molecular cation: a test of molecular quantum mechanics. *Annu. Rev. Phys. Chem.* **46**, 55–82 (1995).
4. Roth, B. et al. in *Precision Physics of Simple Atoms and Molecules* (ed. Karshenboim, S. G.) 205–232 (Springer-Verlag, 2008).
5. Wing, W. H., Ruff, G. A., Lamb, W. E. & Spezeski, J. J. Observation of the infrared spectrum of the hydrogen molecular ion HD^+. *Phys. Rev. Lett.* **36**, 1488–1491 (1976).
6. Arcuni, P. W., Fu, Z. W. & Lundeen, S. R. Energy difference between the (v = 0, R = 1) and the (v = 0, R = 3) states of H_2^+, measured with interseries microwave spectroscopy of H_2 Rydberg states. *Phys. Rev. A* **42**, 6950–6953 (1990).
7. Carrington, A., McNab, I. R., Montgomerie-Leach, C. A. & Kennedy, R. A. Vibration-rotation spectroscopy of the HD^+ ion near the dissociation limit. *Mol. Phys.* **72**, 735–762 (1991).
8. Fu, Z. W., Hessels, E. A. & Lundeen, S. R. Determination of the hyperfine structure of H_2^+ (v = 0, R = 1) by microwave spectroscopy of high-L, n = 27 Rydberg states of H_2. *Phys. Rev. A* **46**, R5313–R5316 (1992).
9. Critchley, A. D. J., Hughes, A. N. & McNab, I. R. Direct measurement of a pure rotation transition in H_2^+. *Phys. Rev. Lett.* **86**, 1725–1728 (2001).
10. Osterwalder, A., Wüest, A., Merkt, F. & Jungen, C. High-resolution millimeter wave spectroscopy and multichannel quantum defect theory of the hyperfine structure in high Rydberg states of molecular hydrogen H_2^+. *J. Chem. Phys.* **121**, 11810–11838 (2004).
11. Koelemeij, J. C. J., Roth, B., Wicht, A., Ernsting, I. & Schiller, S. Vibrational spectroscopy of HD^+ with 2-ppb accuracy. *Phys. Rev. Lett.* **98**, 173002 (2007).
12. Bressel, U. et al. Manipulation of individual hyperfine states in cold trapped molecular ions and application to HD^+ frequency metrology. *Phys. Rev. Lett.* **108**, 183003 (2012).
13. Haase, C., Beyer, M., Jungen, C. & Merkt, F. The fundamental rotational interval of para-H_2^+ by MQDT-assisted Rydberg spectroscopy of H_2. *J. Chem. Phys.* **142**, 064310 (2015).
14. Biesheuvel, J. et al. Probing QED and fundamental constants through laser spectroscopy of vibrational transitions in HD^+. *Nat. Commun.* **7**, 10385 (2016).
15. Korobov, V. I., Hilico, L. & Karr, J.-P. Fundamental transitions and ionization energies of the hydrogen molecular ions with few ppt uncertainty. *Phys. Rev. Lett.* **118**, 233001 (2017).
16. Alighanbari, S., Hansen, M. G., Korobov, V. I. & Schiller, S. Rotational spectroscopy of cold and trapped molecular ions in the Lamb–Dicke regime. *Nat. Phys.* **14**, 555–559 (2018).
17. Jefferts, K. B. Hyperfine structure in the molecular ion H_2^+. *Phys. Rev. Lett.* **23**, 1476–1478 (1969).
18. Schiller, S. & Korobov, V. I. Test of time-dependence of the electron and nuclear masses with ultracold molecules. *Phys. Rev. A* **71**, 032505 (2005).
19. Bakalov, D. & Schiller, S. The electric quadrupole moment of molecular hydrogen ions and their potential for a molecular ion clock. *Appl. Phys. B* **114**, 213–230 (2014); erratum **116**, 777–778 (2014).
20. Karr, J.-Ph. H_2^+ and HD^+: candidates for a molecular clock. *J. Mol. Spectrosc.* **300**, 37–43 (2014).
21. Schiller, S., Bakalov, D. & Korobov, V. I. Simplest molecules as candidates for precise optical clocks. *Phys. Rev. Lett.* **113**, 023004 (2014).
22. Beyer, A. et al. The Rydberg constant and proton size from atomic hydrogen. *Science* **358**, 79–85 (2017).
23. Fleurbaey, H. et al. New measurement of the 1S–3S transition frequency of hydrogen: contribution to the proton charge radius puzzle. *Phys. Rev. Lett.* **120**, 183001 (2018).
24. Bezginov, N. et al. A measurement of the atomic hydrogen Lamb shift and the proton charge radius. *Science* **365**, 1007–1012 (2019).
25. Antognini, A. et al. Proton structure from the measurement of 2*S*–2*P* transition frequencies of muonic hydrogen. *Science* **339**, 417–420 (2013).
26. Grémaud, B., Delande, D. & Billy, N. Highly accurate calculation of the energy levels of the H_2^+ molecular ion. *J. Phys. B* **31**, 383 (1998).
27. Moss, R. E. Energies of low-lying vibration-rotation levels of H_2^+ and its isotopomers. *J. Phys. B* **32**, L89–L91 (1999).
28. Taylor, J. M., Yan, Z.-C., Dalgarno, A. & Babb, J. F. Variational calculations on the hydrogen molecular ion. *Mol. Phys.* **97**, 25–33 (1999).
29. Tiesinga, E., Mohr, P. J., Newell, D. B. & Taylor, B. N. Values of fundamental physical constants. *NIST* https://physics.nist.gov/cuu/Constants/index.html (2019).
30. Wolf, F. et al. Non-destructive state detection for quantum logic spectroscopy of molecular ions. *Nature* **530**, 457–460 (2016).
31. Chou, C. et al. Preparation and coherent manipulation of pure quantum states of a single molecular ion. *Nature* **545**, 203–207 (2017).
32. Schneider, T., Roth, B., Duncker, H., Ernsting, I. & Schiller, S. All-optical preparation of molecular ions in the rovibrational ground state. *Nat. Phys.* **6**, 275–278 (2010).
33. Roth, B., Blythe, P., Wenz, H., Daerr, H. & Schiller, S. Ion-neutral chemical reactions between ultracold localized ions and neutral molecules with single-particle resolution. *Phys. Rev. A* **73**, 042712 (2006).
34. Schiller, S., Roth, B., Lewen, F., Ricken, O. & Wiedner, M. Ultra-narrow-linewidth continuous-wave THz sources based on multiplier chains. *Appl. Phys. B* **95**, 55–61 (2009).
35. Bakalov, D., Korobov, V. I. & Schiller, S. High-precision calculation of the hyperfine structure of the HD^+ ion. *Phys. Rev. Lett.* **97**, 243001 (2006).
36. Schiller, S. & Korobov, V. I. Canceling spin-dependent contributions and systematic shifts in precision spectroscopy of molecular hydrogen ions. *Phys. Rev. A* **98**, 022511 (2018).
37. Bakalov, D., Korobov, V. I. & Schiller, S. Magnetic field effects in the transitions of the HD^+ molecular ion and precision spectroscopy. *J. Phys. B* **44**, 025003 (2011); corrigendum **45**, 049501 (2012).
38. Korobov, V. I., Koelemeij, J. C. J., Hilico, L. & Karr, J.-P. Theoretical hyperfine structure of the molecular hydrogen ion at the 1 ppm level. *Phys. Rev. Lett.* **116**, 053003 (2016).
39. Menasian, S. C. & Dehmelt, H. G. High-resolution study of (1,1/2,1/2)–(1,1/2,3/2) HFS transition in H_2^+. *Bull. Am. Phys. Soc.* **18**, 408 (1973).
40. Heiße, F. et al. High-precision mass spectrometer for light ions. *Phys. Rev. A* **100**, 022518 (2019).
41. Fink, D. J. & Myers, E. G. Deuteron-to-proton mass ratio from the cyclotron frequency ratio of H_2^+ to D^+ with H_2^+ in a resolved vibrational state. *Phys. Rev. Lett.* **124**, 013001 (2020).
42. Sturm, S. et al. High-precision measurement of the atomic mass of the electron. *Nature* **506**, 467–470 (2014).
43. Pastor, P. C. et al. Absolute frequency measurements of the $2^3S_1 \rightarrow 2^3P_{0,1,2}$ atomic helium transitions around 1083 nm. *Phys. Rev. Lett.* **92**, 023001 (2004).
44. Hori, M. et al. Buffer-gas cooling of antiprotonic helium to 1.5 to 1.7 K, and antiproton-to-electron mass ratio. *Science* **354**, 610–614 (2016).
45. Rengelink, R. J. et al. Precision spectroscopy of helium in a magic wavelength optical dipole trap. *Nat. Phys.* **14**, 1132–1137 (2018).
46. Hori, M. et al. Two-photon laser spectroscopy of antiprotonic helium and the antiproton-to-electron mass ratio. *Nature* **475**, 484–488 (2011).
47. Udem, T. Quantum electrodynamics and the proton size. *Nat. Phys.* **14**, 632–632 (2018); correction **14**, 767 (2018).

Methods

Experimental procedure

We simultaneously trapped Be^+ and HD^+ ions in a linear RF trap driven at 14.16 MHz (Extended Data Fig. 1). The distance between the trap centre and the RF electrodes was 4.3 mm. For translational cooling of the molecular ions, we laser-cooled the atomic ions with a laser at 313 nm and the HD^+ ions were sympathetically cooled via electrostatic interactions with the Be^+ ions. We estimated the ion secular temperature as about 30 mK. Typically, roughly 10^2 HD^+ ions were trapped together with about 2×10^3 Be^+ ions. The number of trapped HD^+ ions affects the spectral resolution of the rotational transitions, since the Lamb–Dicke regime can only be reached when the ions' displacements in the transverse direction are much smaller than the transition wavelength.

Black-body radiation populates the excited rotational levels of the ground vibrational state until a thermal equilibrium population is reached. We counteracted this by pumping the HD^+ population into the ground rovibrational state using two lasers. They drive the $(0, 2) \rightarrow (1, 1)$ and $(0, 1) \rightarrow (2, 0)$ transitions, and the spontaneous decay from the respective excited states eventually transfers a large fraction of the HD^+ ions in the rovibrational ground state. A quantum cascade laser at 5.48 μm excited the former transition, and a distributed feedback laser at 2.7 μm excited the latter transition.

After rotational cooling, the terahertz radiation was turned on to drive a transition between specific Zeeman components of a specific hyperfine rotational transition. The terahertz wave intensity was controlled with a half-wave plate, a linear polarizer and via the synthesizer output level. A 1.4-μm laser selectively excited molecules from the (0, 1) level to the (4, 0) level. Molecules in this level were rapidly dissociated by a 266-nm laser.

The spectroscopy scheme relies on the ability to determine the relative decrease of the number of trapped HD^+ ions. Resonant excitation of the HD^+ ions' radial secular motion with an auxiliary a.c. electric field couples to the Be^+ ion ensemble, heating it and causing a change in atomic fluorescence. This fluorescence change is approximately proportional to the number of trapped HD^+ ions. Applying the secular excitation before and after the REMPD and calculating the ratio of average fluorescence levels provides the fractional decrease of the number of HD^+ ions. See Extended Data Fig. 2.

As the REMPD process removes HD^+ ions from the trap, repeated loadings are necessary. With one loading of Be^+, approximately 40 loadings of HD^+ were performed. For each HD^+ loading, typically five spectroscopy cycles were performed. Each cycle lasted 60 s and provided one data point.

The magnetic field was $B_0 \approx 45$ μT, directed along the trap axis, except during rotational spectroscopy/REMPD, when the field was changed to $B \approx 30$ μT or lower, oriented perpendicular to the trap axis and parallel to the terahertz radiation wave vector (Extended Data Fig. 1). The magnitude and direction of the magnetic field were controlled by three pairs of magnetic coils outside the vacuum chamber.

Owing to the complicated statistics of the ion detection process, we assigned one-half of the FWHM of a line as the statistical uncertainty of a measured transition frequency.

Systematic effects

As a guide to and comparison with the experimental work, the ab initio values for various systematic effects were taken from our previous calculations. Explicit values for the Zeeman effect are given in ref. [37]. and for the Stark effect in ref. [48]. The ab initio a.c. polarizabilities at the frequency corresponding to the wavelength 266 nm were computed in ref. [16].

Trap shift. Several systematic shifts are expected to give rise to a quadratic dependence on RF amplitude. These include the micromotion-induced Stark shift[49], phase-offset-induced Stark shift[49], and a.c. Zeeman shift due to an alternating magnetic field at the trap frequency correlated with the electric trap drive.

We therefore measured the dependence of the six lines (including three Zeeman components for line 16 and two Zeeman components for line 19) on the trap RF amplitude. The typical values chosen for the RF amplitude were 150 V, 180 V and 245 V. The precise RF amplitude value for each measurement was determined by measuring the radial secular frequency of Be^+. See Extended Data Fig. 3 for an example of the frequency shift when varying the trap's RF field amplitude. Fits, assuming quadratic dependence, furnish the correction to be applied for obtaining each line's extrapolated frequency for zero RF amplitude. The theory of the Stark shift[48] predicts shifts of the same sign (positive) and of similar value for all components considered here. The experimental data are consistent with this prediction.

Zeeman shift. Both the linear and quadratic Zeeman shift coefficients vary substantially among Zeeman components and hyperfine components (compare, for example, lines 16 and 19 in Fig. 2). The frequency splitting of the two Zeeman components $16_\pm$ together with the theoretical linear Zeeman splitting coefficient (7.98 kHz μT^{-1} (ref. [37])) allows the determination of the (time- and ensemble-averaged) magnetic field affecting the molecular ions. For the data shown in Fig. 2, the nominal magnetic field $B_{nom} = 2.98(3) \times 10^{-5}$ T is consistent with the value deduced using spectroscopy of the co-trapped beryllium ions[50]. The observed linewidth of the $16_\pm$ Zeeman components indicates that the magnetic field is homogeneous to at least 1 part in 30 over the molecule sample.

We measured the frequencies at three different values of magnetic field, for RF amplitudes close to the nominal value of 190 V. Since the RF amplitude varied slightly for the individual measurements, each measured frequency was corrected for the trap shift.

To obtain the $B \rightarrow 0$ extrapolated frequency, $f_i^{(exp)}$, for each line, we fitted to the measured line frequencies $f_i^{(exp)}(B)$ the sum of $f_i^{(exp)}$ plus a quadratic-in-B and/or linear-in-B dependence, depending on the type of Zeeman component. As an accurate measure of the magnetic field, we used the splitting $f_{16_-} - f_{16_+}$. For $m_F = 0 \rightarrow m_F' = 0$ Zeeman components, we assumed a quadratic-in-B dependence. For the two components $19_\pm$ and for the two components $16_\pm$, we allowed for independent linear-in-B shift coefficients $\alpha_{i,+}$, $\alpha_{i,-}$. For f_{16_+}, f_{16_-}, we added to the fit functions the quadratic Zeeman shift predicted by theory. From the fits, we found that the 'positive' and 'negative' shift coefficients of a given line are close: $\alpha_{19,-} \approx \alpha_{19,+}$ and $\alpha_{16,-} \approx \alpha_{16,+}$.

The input data for the magnetic-field dependence fit are the trap-field-extrapolated line frequencies. The reported uncertainty of each $f_i^{(exp)}$ contains both the uncertainty of the magnetic-field extrapolation and the uncertainty due to the trap-field extrapolation.

The magnetic field is produced by three solenoids. They were characterized with a magnetic probe before closing the vacuum chamber. We find the field value deduced from the solenoids' currents agrees with the value deduced from the splitting $f_{16_-} - f_{16_+}$, within the experimental uncertainty of the former.

Trap-induced a.c. Zeeman shift. This effect would show up as a variation of the splitting between two Zeeman components with the trap RF amplitude. The $19_\pm$ components were measured at 245 V and 154 V, at the nominal magnetic field. Their frequency difference did not change, indicating a negligible a.c. Zeeman shift.

Light shift due to cooling laser. The 313-nm cooling laser permanently irradiates the ion cluster, including when the terahertz wave is on. Its nominal power is 100 μW and the beam radius is 0.25 mm. We measured the effect of a change of the 313-nm laser intensity on f_{16_-}. No shift was discernible at the 10-Hz level upon increase of the power by a factor of four.

We computed the scalar, tensor and vector polarizabilities of the rovibrational levels at $\lambda = 313$ nm using high-precision variational

wavefunctions, similar to ref. [48], obtaining $\alpha_s(v=0, L=1) = 3.5054$, $\alpha_t(v=0, L=1) = -0.955$, $\alpha_s(v=0, L=0) = 3.4961$ and $\alpha_t(v=0, L=0) = 0$, in atomic units. The vector polarizabilities are negligible. The computed light shift is of the order of 0.01 Hz. We therefore set the correction due to the 313-nm wave intensity to zero.

Line pulling. We have no observational evidence that Zeeman components, or micromotion-induced sidebands of other hyperfine components, could affect the measured transitions. The small linewidths of the measured transitions are important in this respect. We did not observe any change of f_{16_+}, f_{16_-} and f_{16_0} at the 10-Hz level upon a 500-Hz change of the trap frequency.

d.c. offsets. For every measurement reported in the manuscript, the HD^+ ions are located along the symmetry axis of the Be^+ ion cluster. An offset of 10 V was applied to an electrode to displace the beryllium crystal by about 100 μm from the trap axis along the radial direction. We observed that this offset potential does not have an effect on the position of the HD^+ ions, as also found in molecular dynamics simulations[16]. We measured the frequency shift of f_{19} caused by this offset potential to be 1(10) Hz. Possible day-to-day variations of the trap compensation voltage are a small fraction of the applied offset. Therefore, the size and uncertainty resulting from these variations are negligible.

Light shift due to the two REMPD lasers. The shift due to the 1.4-μm laser and 266-nm laser waves present during spectroscopy has been determined by performing spectroscopy in a different mode, alternating terahertz irradiation and REMPD laser irradiation. The shift has been measured for all lines and all Zeeman components discussed here. The shifts are smaller than or equal to 0.039(17) kHz in absolute value. The measured shifts and their uncertainties are used as corrections.

Other shifts. According to theoretical calculations, the black-body radiation shift[48] and the molecular electric quadrupole shift[51] can be neglected at the present level of accuracy.

Data analysis

Extrapolation of the measured frequencies to zero magnetic field and zero trap amplitude is done by a standard least-squares method. Standard formulae for the propagation of uncertainties are applied.

Spin coefficients, their uncertainties, and sensitivity of the transition frequencies to the spin coefficients

To allow for an accurate comparison between experiment and ab initio theory, we performed a substantially more accurate computation of the spin-structure coefficients of HD^+ compared with our earlier work[35]. We extended the approach developed in ref. [38] and the relevant matrix elements were calculated to ten significant digits. Values of the two spin-structure coefficients for the lower level, $\mathcal{E}_4$ and $\mathcal{E}_5$, and the nine coefficients for the upper level, $\mathcal{E}'_1, \ldots, \mathcal{E}'_9$ are reported in the Extended Data Table 1. Using these coefficients in the diagonalization of the spin-structure Hamiltonian of ref. [35], we obtain the spin frequencies $f_{\mathrm{spin},i}$ (Extended Data Table 1).

The largest spin-structure coefficients, $\mathcal{E}_4$, $\mathcal{E}'_4$, $\mathcal{E}_5$ and $\mathcal{E}'_5$, have theoretical fractional uncertainties of approximately $\varepsilon_4 \approx \varepsilon_5 \approx 1 \times 10^{-6} = \varepsilon_F$. This estimate is confirmed by comparison of the theoretical predictions of the molecular ion H_2^+, calculated with the same theoretical approach, with the experimental results of refs. [17,39]. For a given vibrational level, the rotational dependence of the neglected terms in $\mathcal{E}_4$ and $\mathcal{E}_5$ is nearly zero, because these are contact terms determined by the electronic wave function, which depends very weakly on N. This allows us to assume that the neglected terms in $(\mathcal{E}_4, \mathcal{E}'_4)$ and in $(\mathcal{E}_5, \mathcal{E}'_5)$ are essentially equal, respectively.

Under this assumption, the theory uncertainty of a spin frequency due to these coefficients $k = 4, 5$ is set to $u_k = |\gamma'_{i,k}\mathcal{E}'_k - \gamma_{i,k}\mathcal{E}_k|\varepsilon_F$, where $\gamma_{i,k} = -\partial f_{\mathrm{spin},i}/\partial\mathcal{E}_k$ is the derivative of the spin energy of the lower quantum state involved in the transition i with respect to the spin coefficient $\mathcal{E}_k$, and $\gamma'_{i,k} = \partial f_{\mathrm{spin},i}/\partial\mathcal{E}'_k$ is defined analogously for the upper state. The values of the derivatives are presented in Extended Data Table 1.

The spin Hamiltonian coefficients $\mathcal{E}_4 \approx \mathcal{E}'_4$ and $\mathcal{E}_5 \approx \mathcal{E}'_5$ are similar for the two rotational states, and because the transitions studied here are those between similar spin states, for which $G_1 = G'_1$, $G_2 = G'_2$, the spin frequencies are small, $|f_{\mathrm{spin},i}| \ll \mathcal{E}_4, \mathcal{E}_5, \mathcal{E}'_4, \mathcal{E}'_5$ and the sensitivities are similar, $\gamma'_{i,k} \approx \gamma_{i,k}$. Therefore, we benefit from important reduction of the theory uncertainties u_4 and u_5 contributed by these four coefficients. Even in the least favourable case, line 14, the uncertainty contribution is less than or equal to $u_4 + u_5 \approx 14$ Hz (1×10^{-11}), that is, negligible compared with the following contributions.

A second set of coefficients, $\mathcal{E}'_1$, $\mathcal{E}'_6$ and $\mathcal{E}'_7$, are one to three orders smaller in magnitude, and have estimated fractional uncertainties of $\varepsilon_1 \approx \varepsilon_6 \approx \varepsilon_7 \approx \alpha^2 = \varepsilon_0 \approx 5 \times 10^{-5}$. Their absolute uncertainties, 1.5 kHz to 0.06 kHz, are at a relevant level. They enter the spin-structure frequency uncertainty with contributions $u_k = |\mathcal{E}'_k|\varepsilon_0$.

The fractional uncertainties of the coefficients $\mathcal{E}'_2$, $\mathcal{E}'_3$, $\mathcal{E}'_8$ and $\mathcal{E}'_9$ are similar to ε_0, but are not relevant at the present experimental accuracy level because the coefficients themselves are much smaller than the others.

As the details of the theory errors are unknown, the total uncertainty of the spin frequencies is set conservatively as the sum over all u_k (instead of the root sum of squares).

The sensitivities γ are obtained by first computing the eigenvalues $E_{\mathrm{spin},i}$ and $E'_{\mathrm{spin},i}$ of the Hamiltonian analytically and then computing analytically their derivatives with respect to the individual coefficients $\mathcal{E}_k$ and $\mathcal{E}'_k$. These derivatives are then evaluated for the set of current theory values for $\mathcal{E}_k$ and $\mathcal{E}'_k$.

Fit of the spin Hamiltonian coefficients

From the six measured transitions, we can derive information about the spin Hamiltonian coefficients and about the true spin-averaged frequency. Under the previous assumption of equal theory errors for $(\mathcal{E}_4, \mathcal{E}'_4)$ and for $(\mathcal{E}_5, \mathcal{E}'_5)$, there are six remaining important quantities $(\mathcal{E}'_1, \mathcal{E}'_4, \mathcal{E}'_5, \mathcal{E}'_6, \mathcal{E}'_7$ and $f_{\mathrm{spin\text{-}avg}})$, and they can be solved for using a set of equations in which the experimental frequencies are equal to the corresponding theoretical frequencies, allowing for small deviations from the nominal values. We find $\mathcal{E}'^{(\mathrm{fit})}_1 - \mathcal{E}'^{(\mathrm{theor})}_1 = 0.32(20)$ kHz, where the uncertainty is smaller than the theory uncertainty, $\varepsilon_F\mathcal{E}'_1 \approx 1.6$ kHz. Furthermore, $\mathcal{E}'^{(\mathrm{fit})}_6 - \mathcal{E}'^{(\mathrm{theor})}_6 = 0.5(9)$ kHz, $\mathcal{E}'^{(\mathrm{fit})}_7 - \mathcal{E}'^{(\mathrm{theor})}_7 = -0.3(4)$ kHz and $f^{(\mathrm{fit})}_{\mathrm{spin\text{-}avg}} - f^{(\mathrm{theor})}_{\mathrm{spin\text{-}avg}} = -0.05(22)$ kHz. The shown uncertainties result from the experimental errors and the theory error of $f^{(\mathrm{theor})}_{\mathrm{spin\text{-}avg}}$; the theory errors of $\mathcal{E}'_2$, $\mathcal{E}'_3$, $\mathcal{E}'_8$ and $\mathcal{E}'_9$ make negligible contributions. The deviations of $\mathcal{E}'_4$ and $\mathcal{E}'_5$ from the nominal values cannot be determined precisely (an aspect that is intrinsic to the favoured transitions), but are consistent with zero.

Composite frequencies

The coefficients of the composite frequency given in the main text are:

$$b_{12} = 0.0863720\ldots, \quad b_{14} = 0.1456348\ldots, \quad b_{16} = 0.2516111\ldots,$$
$$b_{19} = 0.2442792\ldots, \quad b_{20} = 0.1328074\ldots, \quad b_{21} = 0.1392955\ldots$$

We consider alternative composite frequencies. One alternative ansatz for finding a composite frequency is to impose the 'insensitivity conditions' $0 = \partial f^{(\mathrm{theor})}_c/\partial\mathcal{E}_{k_\alpha} = \sum_i b_i\gamma_{i,k_\alpha}$, $0 = \partial f^{(\mathrm{theor})}_c/\partial\mathcal{E}'_{k_\beta}$ for a suitable subset $\{k_\alpha, k_\beta\}$ of spin Hamiltonian coefficients. As discussed above, if we assume correlated errors for the pair $(\mathcal{E}_4, \mathcal{E}'_4)$ and $(\mathcal{E}_5, \mathcal{E}'_5)$, then the largest theory uncertainties arise from $\mathcal{E}'_1$, $\mathcal{E}'_6$ and $\mathcal{E}'_7$. Four experimentally measured transitions are sufficient to satisfy the three insensitivity conditions for these three coefficients. The normalization condition

is easily imposed in addition. Considering, for example, the lines 14, 16, 19 and 21, the resulting uncertainty from hyperfine theory is $u(f^{(\mathrm{theor})}_{\mathrm{spin,c}}) \approx 2$ Hz, much smaller than the uncertainty of the spin-averaged frequency $u(f^{(\mathrm{theor})}_{\mathrm{spin\text{-}avg}}) \approx 0.02$ kHz. Thus, the composite frequency has a substantially reduced theory uncertainty compared with those of the individual hyperfine transitions. $f^{(\mathrm{theor})}_{\mathrm{c}}$ is then also numerically close to $f_{\mathrm{spin\text{-}avg}}$, $f^{(\mathrm{theor})}_{\mathrm{c}} \approx f^{(\mathrm{theor})}_{\mathrm{spin\text{-}avg}} + 2,232$ kHz. With more available transitions we can impose additional conditions.

A second alternative composite frequency is as follows. As in the main text, we consider a composite frequency that minimizes the spin-coefficients-related uncertainty. If we assume correlated $\mathcal{E}$ errors, the linear combination of only three lines, $f_{\mathrm{c}} = b_{14}f_{14} + b_{16}f_{16} + (1 - b_{14} - b_{16})f_{21}$, yields an uncertainty of 3 Hz (2.4×10^{-12}). As in the first alternative, this uncertainty is also much smaller than $u(f^{(\mathrm{theor})}_{\mathrm{spin\text{-}avg}})$. The coefficients are $b_{14} = 0.0814\ldots$, $b_{16} = 0.615\ldots$ and $f^{(\mathrm{theor})}_{\mathrm{c}} = f^{(\mathrm{theor})}_{\mathrm{spin\text{-}avg}} + 1,524.23$ kHz. Such optimal solutions exist independently of the concrete values of the estimated theory uncertainties of the $\mathcal{E}$ coefficients: if the assumed fractional uncertainties ε_k are doubled, a solution is obtained whose theory uncertainty is correspondingly larger, 6 Hz. The relationship between the solution $f^{(\mathrm{theor})}_{\mathrm{c}}$ and the cancellation conditions is that the determinant of the sensitivity matrix $\Gamma_{i,k} = \gamma'_{i,k} = \partial f^{(\mathrm{theor})}_i / \partial \mathcal{E}'_k$ (where $i = \{14, 16, 21\}$ and $k = \{1, 6, 7\}$), is close to zero (about 0.008). This implies that these three transitions are nearly linearly dependent and allow for a composite frequency that nearly satisfies the cancellation conditions (and the normalization condition).

If the correlation assumption is not made, the optimum composite frequency based on lines 14, 16 and 21 yields a comparatively large spin-energy uncertainty of 0.22 kHz. For this reason, in the main text, we determined the composite frequency based on six lines.

A third example is the composite frequency based on the five lines 14, 15, 16, 19 and 20: it yields a theory uncertainty $\bar{u}(f^{(\mathrm{theor})}_{\mathrm{spin,c}}) \approx 3$ Hz.

Finally, an example of composite frequency for a vibrational transition is the following. For the transition $(v = 0, N = 0) \rightarrow (v' = 1, N' = 1)$ the six lines 14, 15, 16, 19, 20 and 21 yield a composite frequency with theory uncertainty $\bar{u}(f^{(\mathrm{theor})}_{\mathrm{spin,c}}) \approx 2$ Hz. This is only 3×10^{-14} relative to the vibrational transition frequency $f_{\mathrm{spin\text{-}avg}} \approx 58.6$ THz.

Fifth force bound

Given the present results, the 95% confidence limit to the strength of the fifth force, $\beta_{\max}(\lambda)$, is approximately given by

$$N_1 N_2 |\Delta Y(\lambda)| \beta_{\max}(\lambda) \approx 2h u_{\mathrm{tot}}(f_{\mathrm{rot}}),$$

$$u_{\mathrm{tot}}(f_{\mathrm{rot}})^2 = u(f^{(\mathrm{exp})}_{\mathrm{spin\text{-}avg}})^2 + u(f^{(\mathrm{theor})}_{\mathrm{spin\text{-}avg}})^2 + u_{\mathrm{CODATA2018}}(f^{(\mathrm{theor})}_{\mathrm{spin\text{-}avg}})^2$$

Here, $\Delta Y(\lambda)$ is obtained numerically from perturbation theory as the difference of the expectation value of $R^{-1}\exp(-R/\lambda)$ in the two rotational states, where R is the internuclear separation divided by 1 atomic unit, and λ, N_1 and N_2 were defined in Fig. 3.

We have also obtained an analytical approximate expression

$$\beta_{\max}(\lambda) \approx 2 \frac{u_{\mathrm{tot}}(f_{\mathrm{rot}})}{f_{\mathrm{rot}}} \frac{e^{R_{\mathrm{e}}/\lambda}}{2N_1N_2(1 + R_{\mathrm{e}}/\lambda)} \frac{R_{\mathrm{e}}E^2_{\mathrm{vib}}}{E_{\mathrm{rot}}} \quad (4)$$

where R_{e} is the equilibrium separation, and $E_{\mathrm{rot}} = f_{\mathrm{rot}}/2cR_\infty$ and E_{vib} are the fundamental rotational transition energy and fundamental vibrational transition energy, respectively. They are all normalized to the respective atomic unit. The previous bounds on β are also discussed in ref. [52].

Electric quadrupole moment of the deuteron

We deduce a value for the electric quadrupole moment of the deuteron, Q_{d}. The tensor interaction between Q_{d} and the electric field gradient within the HD^+ molecule[35] contributes to the hyperfine structure. It is quantified by the spin Hamiltonian coefficient $\mathcal{E}'_9 = 5.666$ kHz $\propto Q_{\mathrm{d}}$. The ratio $\mathcal{E}'_9/Q_{\mathrm{d}}$ is available from our theory with small fractional uncertainty $\varepsilon_0 \approx 5 \times 10^{-5}$. The frequencies of the rotational transition components are sensitive to $\mathcal{E}'_9$ to varying degrees, quantified by $\gamma'_{i,9}$ (see Extended Data). We therefore consider a composite frequency $f'_{\mathrm{c}} = \sum_i a_i f_i$ that suppresses the spin-averaged frequency, and thus all QED contributions, by imposing $\sum_i a_i = 0$. We determine the weight set $\{a_i\}$ that maximizes the sensitivity-to-uncertainty ratio $|\partial f'_{\mathrm{c}}/\partial \mathcal{E}'_9|^2/(u(f'^{(\mathrm{theor})}_{\mathrm{c}})^2 + u(f'^{(\mathrm{exp})}_{\mathrm{c}})^2)$. We find $a_{12} = -0.2165167$, $a_{14} = 0.6508068$, $a_{16} = -0.9098989$, $a_{19} = -0.9738303$ and $a_{20} = -0.1153690$.

From the comparison of $f'^{(\mathrm{theor})}_{\mathrm{c}}$ and $f'^{(\mathrm{exp})}_{\mathrm{c}}$, we then deduce $Q'_{\mathrm{d}} = 0.282(4)$ fm^2. It is consistent with the reference value $Q_{\mathrm{d}} = 0.28578(3)$ fm^2, obtained from RF spectroscopy of neutral D_2 and theory[53]. The precision is expected to improve with progress in MHI spin-structure theory and experimental precision.

Data availability

The datasets generated during and/or analysed during the current study are available from the corresponding author on reasonable request.

48. Schiller, S., Bakalov, D., Bekbaev, A. K. & Korobov, V. I. Static and dynamic polarizability and the Stark and blackbody-radiation frequency shifts of the molecular hydrogen ions H^+_2, HD^+, and D^+_2. *Phys. Rev. A* **89**, 052521 (2014).
49. Berkeland, D. J., Miller, J. D., Bergquist, J. C., Itano, W. M. & Wineland, D. J. Minimization of ion micromotion in Paul trap. *J. Appl. Phys.* **83**, 5025–5033 (1998).
50. Shen, J., Borodin, A. & Schiller, S. A simple method for characterization of the magnetic field in an ion trap using Be^+ ions. *Eur. Phys. J. D* **68**, 359 (2014).
51. Bakalov, D. & Schiller, S. The electric quadrupole moment of molecular hydrogen ions and their potential for a molecular ion clock. *Appl. Phys. B* **114**, 213–230 (2014); corrigendum **116**, 777–778 (2014).
52. Salumbides, E. J., Ubachs, W. & Korobov, V. I. Bounds on fifth forces at the sub-Å length scale. *J. Mol. Spectrosc.* **300**, 65–69 (2014).
53. Pavanello, M., Tung, W.-C. & Adamowicz, L. Determination of deuteron quadrupole moment from calculations of the electric field gradient in D_2 and HD. *Phys. Rev. A* **81**, 042526 (2010).

Acknowledgements We thank M. G. Hansen for assistance with optimization of the apparatus and J.-Ph. Karr for checking theoretical expressions. This work has received funding from the European Research Council (ERC) under the European Union's Horizon 2020 research and innovation programme (grant agreement number 786306, 'PREMOL'), and from the Deutsche Forschungsgemeinschaft in project Schi 431/23-1. S.A. acknowledges a fellowship of the Prof.-W.-Behmenburg-Schenkung. V.I.K. acknowledges support from the Russian Science Foundation under grant number 18-12-00128.

Author contributions S.A. and G.S.G. performed the measurements and analysed data, F.L.C. contributed to the measurements. S.A. developed and maintained the apparatus. V.I.K. performed the ab initio calculations, S.S. performed data and theoretical analyses, prepared the manuscript and supervised the work. All authors contributed to discussion and manuscript editing.

Competing interests The authors declare no competing interests.

Additional information
Correspondence and requests for materials should be addressed to S.S.
Peer review information *Nature* thanks Brian Odom, Richard Thompson and the other, anonymous, reviewer(s) for their contribution to the peer review of this work.

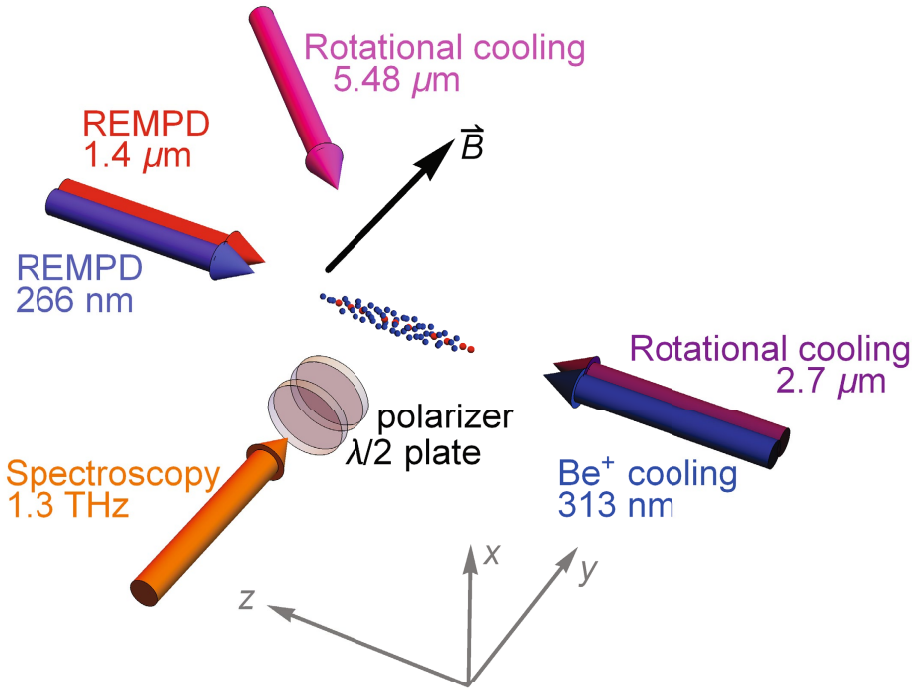

Extended Data Fig. 1 | Conceptual view of the arrangement used for high-resolution spectroscopy of HD^+ using TICTES. The spectroscopy wave (1.3 THz) crosses the ion cluster perpendicular to its long axis, enabling spectroscopy in the Lamb–Dicke regime. The ion cluster comprises atomic Be^+ ions (blue dots) and HD^+ molecular ions (red dots). The indicated laser beams implement the Doppler cooling of Be^+ ions (313 nm), rotational cooling of HD^+ (2.7 μm and 5.48 μm) and detection by REMPD (266 nm and 1.4 μm). The magnetic field **B** lifts the degeneracy of Zeeman sublevels during terahertz spectroscopy. The polarizer and the half-wave plate enable adjustment of the polarization and intensity of the terahertz radiation.

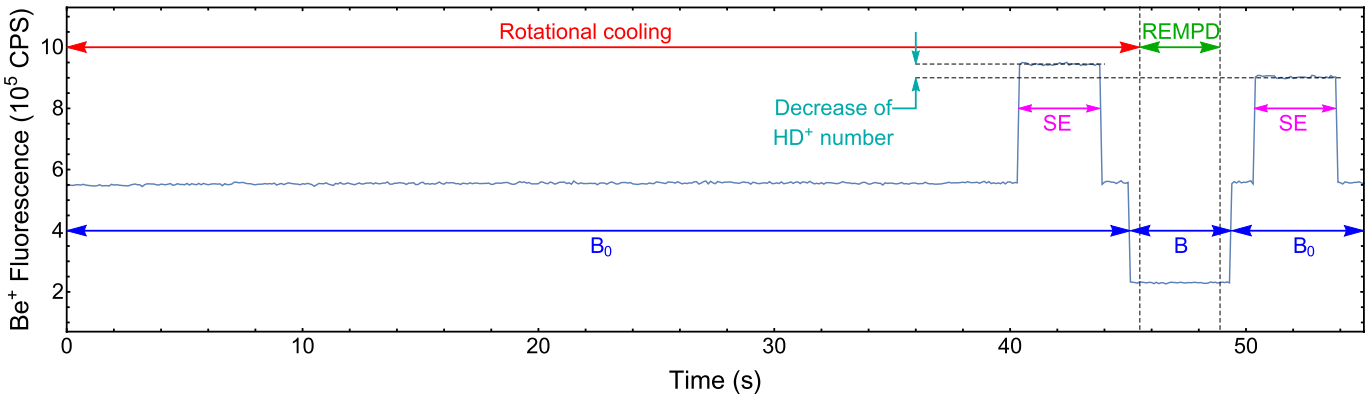

Extended Data Fig. 2 | Beryllium ion fluorescence during one preparation–spectroscopy cycle. Spectroscopy (terahertz wave on) occurs during the interval marked 'REMPD'. Beryllium laser cooling is on all the time. SE, secular excitation. B, a magnetic flux strength B is applied during REMPD. B_0, a strength B_0 is applied for rotational laser cooling. CPS, counts per second. The signal obtained from the spectroscopy cycle is indicated in cyan.

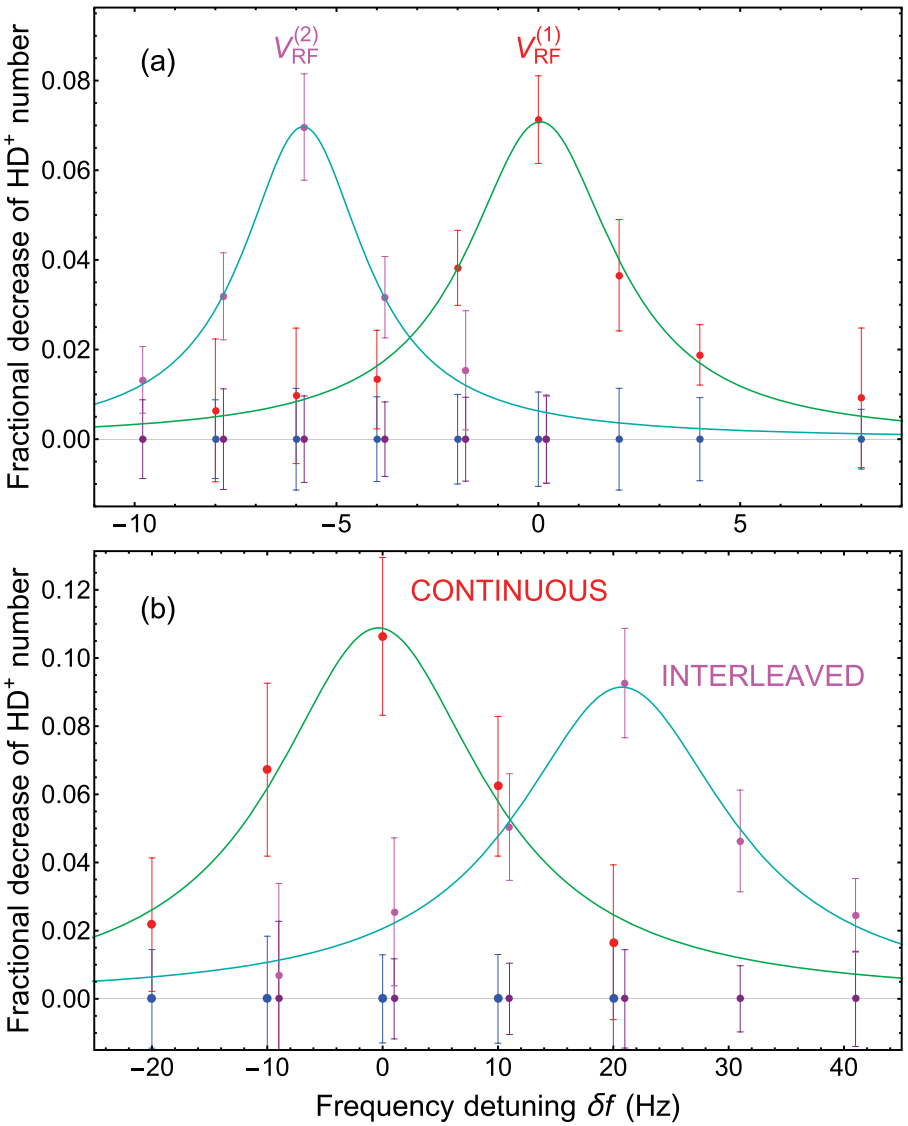

Extended Data Fig. 3 | Systematic shifts of the Zeeman component 19, of the rotational hyperfine transition line 19. a, The trap's amplitude is decreased by 2.5 V from $V_{RF}^{(1)}$ to $V_{RF}^{(2)}$. The FWHM linewidth is 4 Hz, corresponding to 3×10^{-12} fractional FWHM. **b**, The light shift induced by the 266 nm and 1.4 μm dissociation lasers, determined by comparing two spectroscopy modes. 'Continuous' indicates that the lasers are on when the terahertz radiation is applied. 'Interleaved' indicates that the lasers and terahertz radiation are on alternatingly.

Extended Data Table 1 | Spin Hamiltonian coefficients, spin-structure frequencies and spin-frequency derivatives

		$\mathcal{E}_1'$	$\mathcal{E}_2'$	$\mathcal{E}_3'$	$\mathcal{E}_4'$	$\mathcal{E}_5'$	$\mathcal{E}_6'$	$\mathcal{E}_7'$	$\mathcal{E}_8'$	$\mathcal{E}_9'$	$\mathcal{E}_4$	$\mathcal{E}_5$
		31.98465	−0.03134	−0.004810	924.56943	142.16092	8.61111	1.32177	−0.003057	0.005666	925.39588	142.28781
Line i	$f_{\mathrm{spin},i}^{(\mathrm{theor})}$	$\gamma'_{i,1}$	$\gamma'_{i,2}$	$\gamma'_{i,3}$	$\gamma'_{i,4}$	$\gamma'_{i,5}$	$\gamma'_{i,6}$	$\gamma'_{i,7}$	$\gamma'_{i,8}$	$\gamma'_{i,9}$	$\gamma_{i,4}$	$\gamma_{i,5}$
12	−33.20866	−0.569	−0.559	−1.718	0.250	0.425	0.039	−3.347	−3.284	−2.944	0.250	0.500
14	−9.07415	−0.429	−0.386	0.654	0.249	−0.908	−1.028	0.834	0.721	−0.502	0.250	−1.000
16	−2.13496	−0.107	0.111	0.995	−0.734	−0.184	0.010	0.143	−0.157	−0.493	−0.737	−0.169
19	10.07468	0.500	0.500	1.000	0.250	0.500	−0.500	−1.000	−1.000	−0.500	0.250	0.500
20	11.73591	−0.225	−0.265	−0.510	0.250	0.500	1.734	3.439	3.559	1.764	0.250	0.500
21	11.78771	0.332	0.154	0.514	0.234	−0.315	0.255	−0.582	−0.402	0.229	0.237	−0.331

$\mathcal{E}'_k$ ($\mathcal{E}_k$) are the updated coefficients of the spin Hamiltonian[35] of the upper (lower) rotational level, in MHz. $f_{\mathrm{spin},i}^{(\mathrm{theor})}$ are theoretical spin frequencies in MHz. γ are the dimensionless sensitivities of the spin frequencies to the spin Hamiltonian coefficients. $\gamma'_{i,k} = \partial f_{\mathrm{spin},i}^{(\mathrm{theor})}/\partial \mathcal{E}'_k$ refer to the upper state and $\gamma_{i,k} = -\partial f_{\mathrm{spin},i}^{(\mathrm{theor})}/\partial \mathcal{E}_k$ to the lower state. The entries for line 19 are decimal representations of rational values (see equation (6) in ref. [37]). Note that because of the tracelessness of the spin Hamiltonian[36], $\sum_i d_i \gamma_{i,k} = 0$ and $\sum_i d'_i \gamma'_{i,k} = 0$, where $d_i = (2F(i) + 1)/36$ and $d'_i = (2F'(i) + 1)/36$ are the degeneracies of the respective spin states, and the sum is over the ten favoured transitions $i = 12, \ldots, 21$.

Results

Doppler-free rotational spectroscopy of HD^+ enabled us to improve both resolution and accuracy of experimental data compared to previous spectroscopy of the MHIs. A smallest fractional FWHM linewidth of 3×10^{-12} is achieved (see Fig. 6.1), and for the first time individual Zeeman components of hyperfine transitions of HD^+ are resolved. Pre-

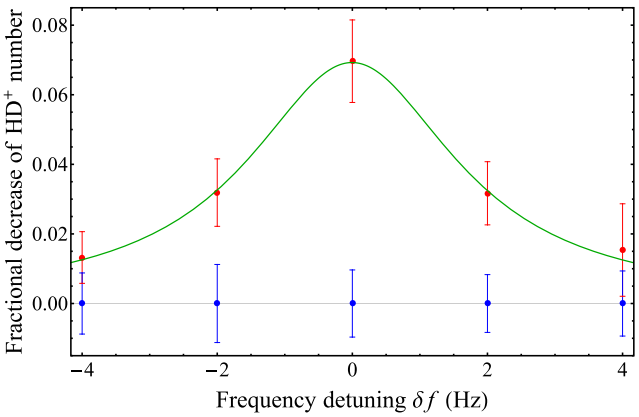

Figure 6.1. Measured spectrum of the $m_F = +2 \rightarrow m'_F = +3$ component of the $|0,0,1,2,2\rangle \rightarrow |0,1,1,2,3\rangle$ transition in HD^+. Fit with a Lorentzian lineshape (green trace). The FWHM of the fitted lineshape is 3.76±0.82 Hz and the uncertainty (standard error) of the fitted center frequency is 0.37 Hz. The origin of the frequency axis is set to coincide with the fitted line maximum.

cise measurements of 6 hyperfine components and characterization of systematic shifts allowed to perform the most accurate comparison of experiment and theory for bound three-body quantum systems. We used the composite frequency approach to suppress the impact of limited theoretical accuracy of the spin structure. In this way, we established agreement between theory and experiment at the 5×10^{-11} level limited by uncertainties of CODATA 2018. We confirmed the QED contributions of proton and deuteron finite radii with 0.7% uncertainty of the total contribution.

In addition, hyperfine energy splittings were experimentally determined, and they were compared with the *ab initio* spin energy calculations. The comparison confirmed the spin energy predictions within the uncertainty of theory. Since the experimental uncertainties are significantly lower, the obtained spin energy data offers new benchmark values for future improved *ab initio* theory of the spin structure.

The combination of fundamental constants $R_\infty m_e(1/m_p+1/m_d)$ is determined with 2.0×10^{-11} fractional uncertainty, which is 2.4 times more precise than CODATA 2018 (see Fig. 6.2).

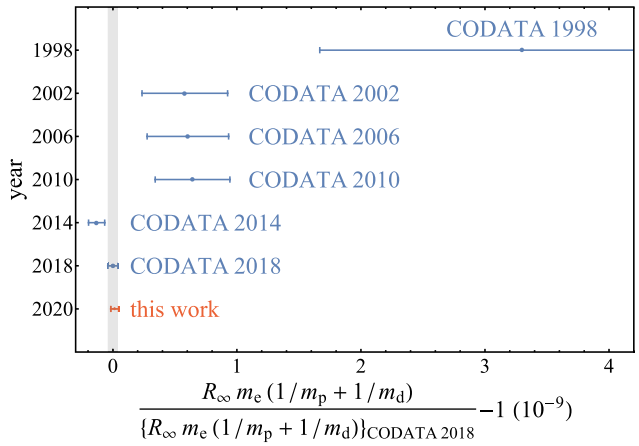

Figure 6.2. Comparison of the value of $R_\infty m_e(1/m_p+1/m_d)$ measured in this thesis with the values computed using the CODATA constants. The gray shaded area is the CODATA 2018 uncertainty. The CODATA 2018 uncertainty is calculated considering the correlations of R_∞, m_e/m_p, and m_e/m_d.

We also determined the proton mass with the same uncertainty as in CODATA 2018, and in a good agreement with the direct mass measurement in a Penning trap.

Using a recently measured deuteron-to-proton mass ratio in a Penning trap, we obtained the proton-to-electron mass ratio with 2.0×10^{-11} fractional uncertainty (see Fig. 6.3). Therefore, our results confirmed the substantial changes introduced in the CODATA 2018.

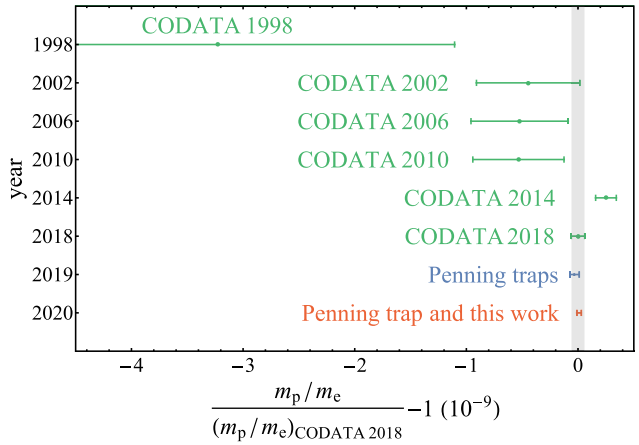

Figure 6.3. The proton-electron mass ratio deduced in this thesis (considering the Penning trap direct measurement of m_e/m_d), and its comparison with the Penning trap measurements and the CODATA values.

We exploited the resolved hyperfine structure for a determination of the deuteron quadrupole moment Q_{d} with 1.5% fractional uncertainty.

We set upper bounds on a hypothetical fifth force, acting between proton and deuteron at separations of the order of 1 Å. Modeling such an interaction with a Yukawa-type potential and computing the resulting frequency shift, we ruled out interactions at $\lambda = 1 - 2\,\text{Å}$ range and strengths larger than 2×10^{-11} Hartree with 95% confidence level.

Conclusion and Outlook

We invented a method for Doppler-free rotational spectroscopy of molecular ions. Our technique is based on spatial confinement of molecular ions inside a laser cooled atomic Coulomb crystal of prolate ellipsoidal shape. When the charge-squared-to-mass ratio of molecular ions is larger than that of the atomic ions, the former will stay close to the long crystal axis.

With excitation direction transverse to the long axis of the crystal, the Lamb-Dicke regime is achieved when the extent of radial motion of molecular ions is much smaller than wavelength of spectroscopy radiation. The technique is also applicable to stimulated Raman and two-photon transitions, if effective wavelength of transitions are large compared to extent of radial motion of the molecular ions.

This technique is applicable to variety of molecular ions, with suitable choice of laser-coolable atomic ion. For example, many molecular ions have charge-to-mass ratio close to but greater than the ytterbium ion $^{171}Yb^{+}$, which allow simultaneous trapping of the atomic and molecular ions.

Among a multitude of molecular ions we choose the MHIs for our experiment, which are interesting systems for metrological purposes. High precision calculations of their energies allow comparison of theory and experiment to determine fundamental constants and search for new physics. The HD^{+} ion possesses an electric dipole moment, which allows single photon electric dipole transitions, we focus on its spectroscopy in this thesis.

A particularly interesting goal of Doppler-free spectroscopy of HD^{+} is to determine the values of a subset of fundamental constants of physics. Our rotational spectroscopy results allowed determination of the proton mass, the proton-to-electron mass ratio, and the combination of fundamental constants $R_\infty m_e(1/m_p+1/m_d)$ with fractional uncertainty of 10^{-11}. Our results are in agreement with CODATA 2018 values, and in some cases are measured with smaller uncertainty (see chapter 5 and Results). The hyperfine resolved spectrum also enabled the determination of the deuteron quadrupole moment.

Additionally, our experimental and theoretical comparison allowed us to contribute to the proton radius puzzle understanding. A combined experimental and theoretical relative frequency uncertainty of 5×10^{-11} allowed the independent consistency check of the recent changes in CODATA 2018 values of the nuclear charge radii.

So far we have investigated 6 dipole allowed hyperfine transitions, but our technique can be extended to spectroscopy of spin-forbidden (where quantum number G_2 changes but G_2 stays the same, see Eq. 2.3) and doubly-spin-forbidden (where both quantum numbers G_1 and G_2 change) transitions. High precision spectroscopy of spin-forbidden and doubly-spin-forbidden transitions will allow us to fully resolve the hyperfine energy splittings of the ground and excited rotational levels, which allows a complete test of the spin structure calculations. The ability to excite the doubly-forbidden-transitions should allow performing to perform an effective hyperfine selective quantum state preparation and to improve the signal-to-noise ratio. For this purpose, during the rotational cooling, THz radiation would be applied to remove the population of unwanted hyperfine states which in turn would lead to more population in the desired state.

Molecular dynamics simulations for a string of HD^+ ions at ~30 mK indicated possibility of the Lamb-Dicke regime for transverse excitation at 5.1 μm [73]. Therefore, spectroscopy of rovibrational transitions with wavelength larger than 5 μm (e.g. $(0,0) \rightarrow (1,1)$ or $(0,2) \rightarrow (1,1)$), with spectral resolution comparable to or better than the present rotational spectroscopy, can be achieved.

Besides, laser-stimulated electric quadrupole transitions in the MHIs exhibit very small natural linewidth, and allow frequency metrology of the MHIs [74]. Since these transitions are extremely weak, addressing and characterizing them is very challenging. Although dipole forbidden transitions have been observed in N_2^+ molecular ion [75], they remained untapped in the MHIs. A $(0,0) \rightarrow (1,2)$ transition in HD^+ is a candidate that can be investigated using our experimental apparatus.

This work also gives strong motivation for further improvement of spin structure theory and more precise QED calculations of the spin-averaged frequency for both rotational and vibrational transitions. The magnitude of the detected systematic shifts shows that uncertainty of order 10^{-14} for vibrational overtone transitions is feasible. Through improvement of precision, combination of rotational and vibrational spectroscopy results, and *ab initio* theory, the fundamental constants R_∞, m_e/m_p, m_e/m_d, r_p, and r_d can be determined independently with accuracies competitive or better than CODATA 2018.

Our technique can be employed also for high precision spectroscopy of homonuclear H_2^+, through stimulated Raman or two-photon transitions with large effective wavelength, which can be used to independently determine the fundamental constants R_∞, m_p/m_e, and r_p. High precision spectroscopy of H_2^+ and the antihydrogen molecular ion $\bar{H}_2^-$ ($\bar{p}\bar{p}e^+$) is sensitive to CPT violation and can be used to search for physics beyond the SM. Additionally, we anticipate that the search for the weak nuclear force induced parity violation in chiral molecules can benefit from our technique.

A. Appendix

Photos of the experimental apparatus

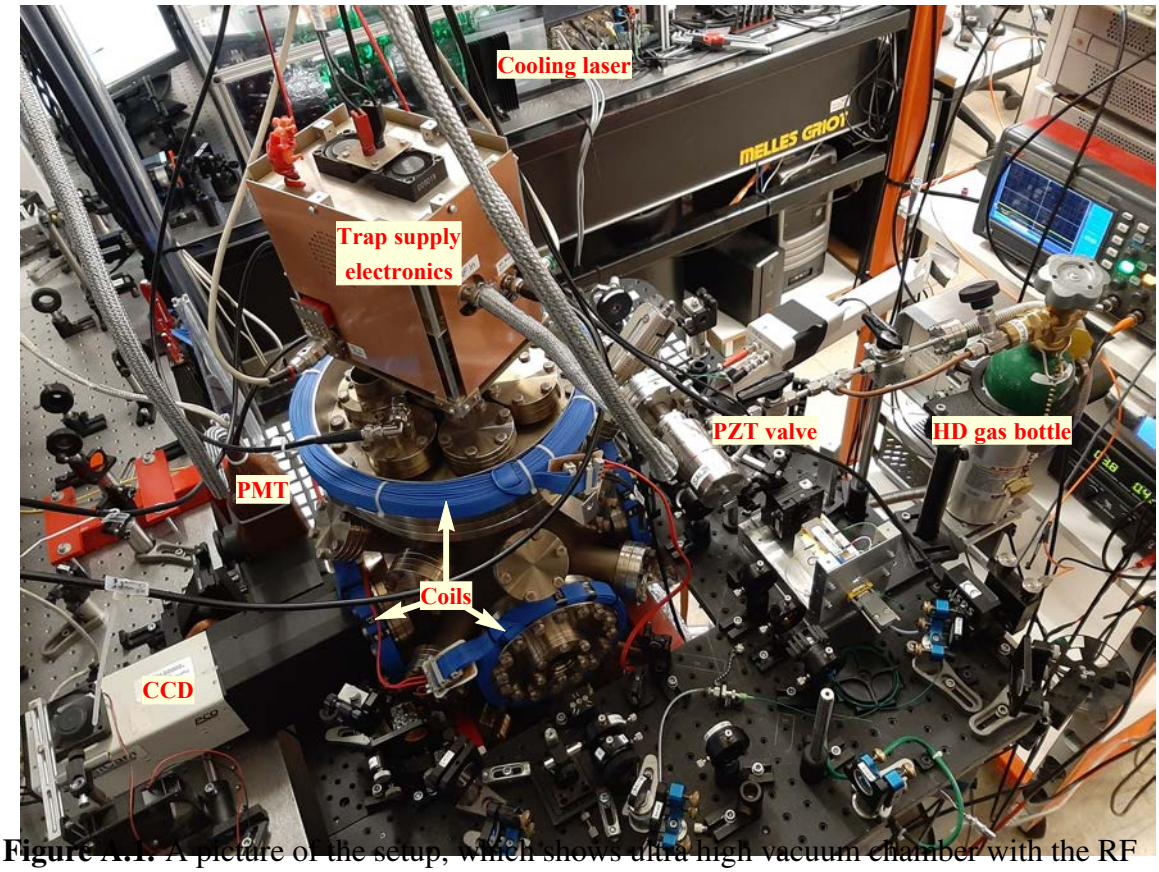

Figure A.1: A picture of the setup, which shows ultra high vacuum chamber with the RF trap electronics in a copper shielding on top. Optics on the table around the vacuum chamber align the cooling laser and spectroscopy lasers into the trap (see Fig. A.2 and Fig. A.3). Fluorescence of the Be^+ ions are detected with the CCD camera and the PMT, placed on the left side of the vacuum chamber. There are three magnetic coil pairs to control the magnetic field. The PZT valve is between the vacuum chamber and the HD gas bottle to control the amount of HD gas released into the chamber. Part of the cooling laser can be seen on top of the picture.

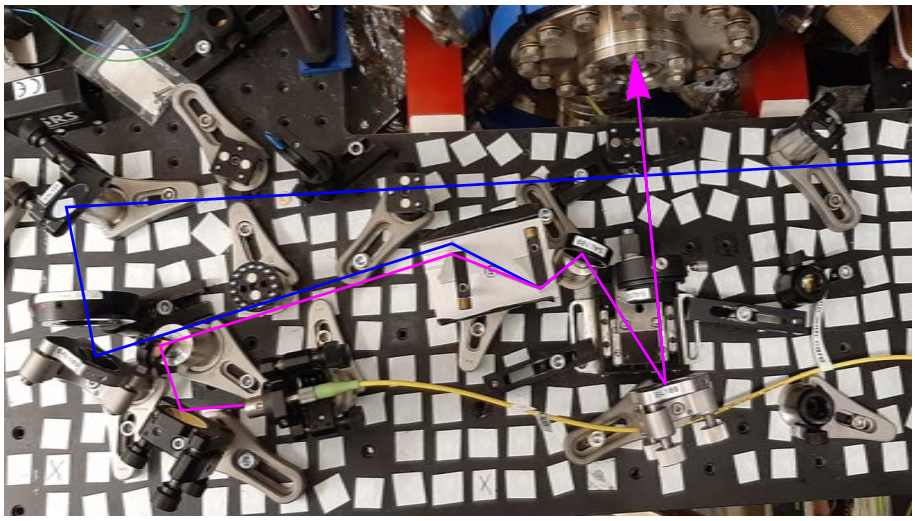

Figure A.2. A picture of part of the optical setup around the vacuum chamber, which is used to align the cooling laser (blue arrow) and the 2.713 μm laser (magenta arrow) into the trap. The white stickers are covering the optical breadboard's tapped holes to allow air-tight box (other walls of the box are not visible in the picture) around the vacuum chamber for nitrogen purging.

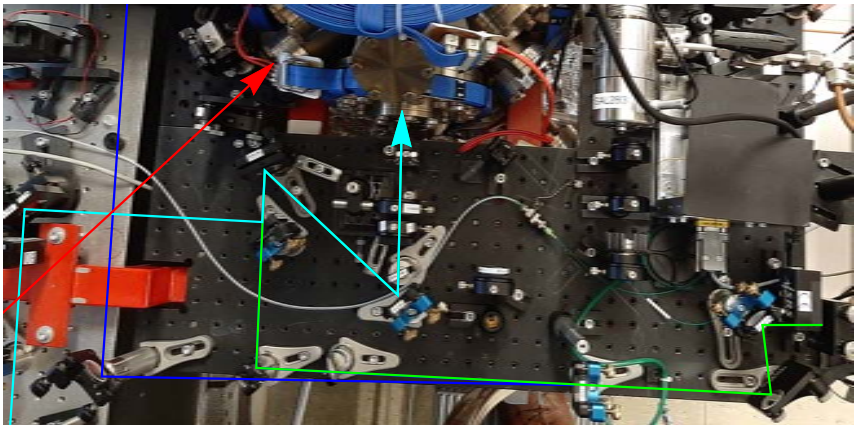

Figure A.3. A picture of part of the optical setup, which couples the 266 nm laser (cyan arrow), the IR laser (green arrow), and the 5.483 μm laser (red arrow) into the trap. The cooling laser (blue arrow) is used as a guide beam for geometrical alignment of other lasers, but it will be blocked during the experiment.

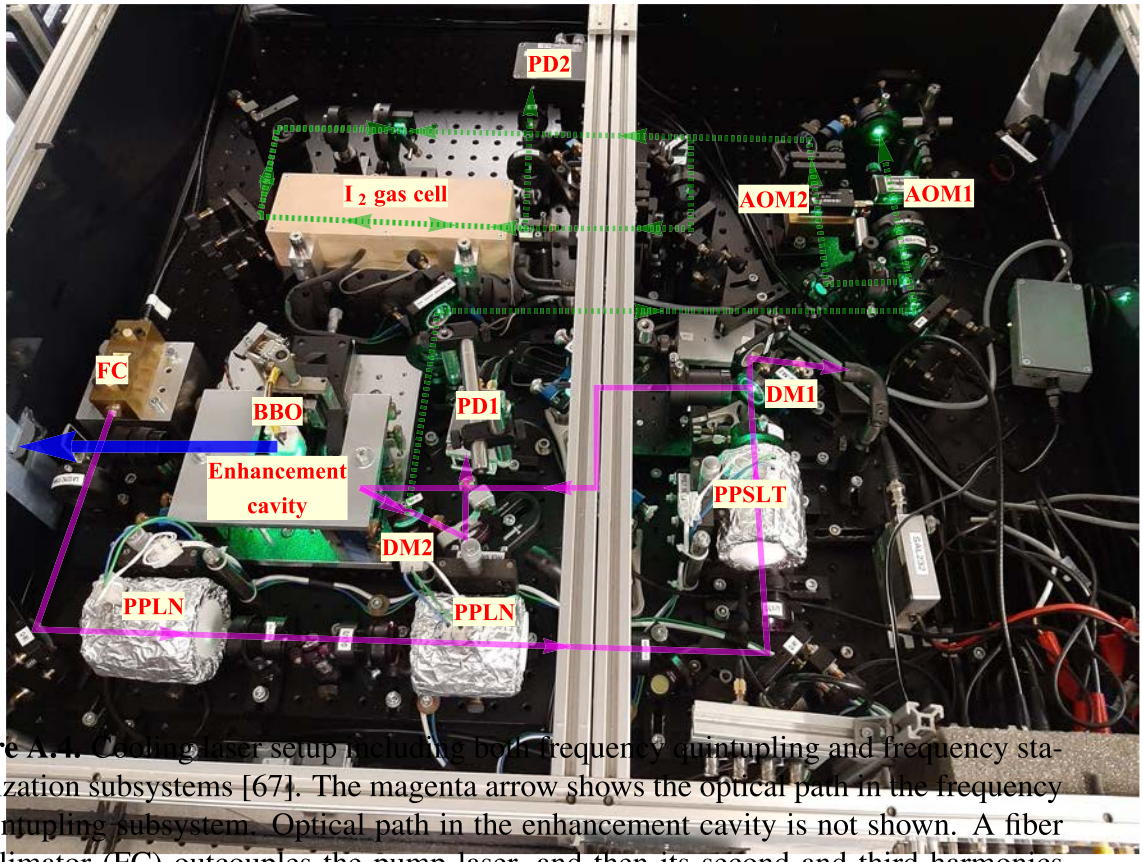

Figure A.4. Cooling laser setup including both frequency quintupling and frequency stabilization subsystems [67]. The magenta arrow shows the optical path in the frequency quintupling subsystem. Optical path in the enhancement cavity is not shown. A fiber collimator (FC) outcouples the pump laser, and then its second and third harmonics are generated in the PPLN and PPSLT crystals, respectively. A dichroic mirror (DM1) splits the pump laser and reflects the second and third harmonics to the enhancement cavity, where the 313 nm radiation (blue arrow) is generated inside a BBO crystal. A dichroic mirror (DM2) splits the cavity reflection, where the second harmonic is sent to a photodetector (PD1) for the enhancement cavity stabilization. The third harmonic reflected from the DM2 is used for frequency stabilization of the cooling laser. The dashed green arrow indicates the optical path. The double pass AOM (AOM1) is used to fine tune the cooling laser frequency and the AOM2 provides the pump and probe beams for saturation spectroscopy of molecular iodine gas.

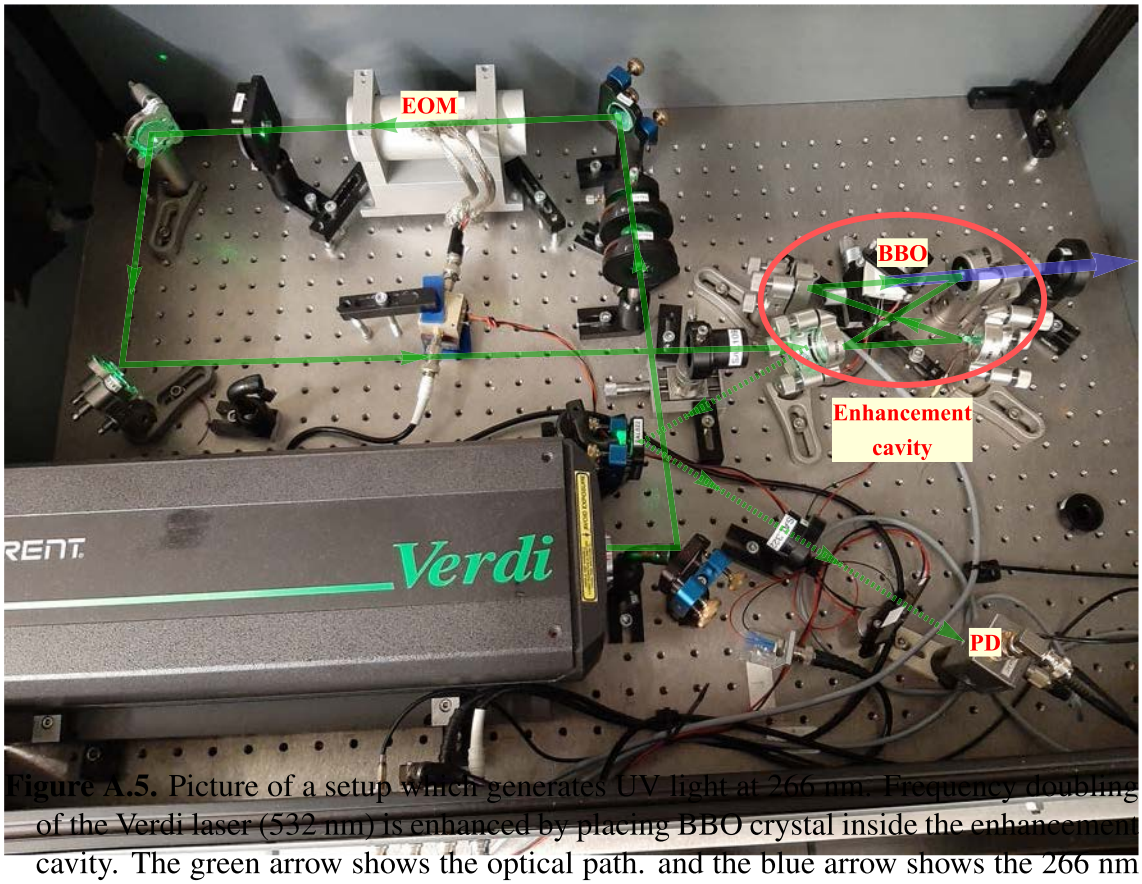

Figure A.5. Picture of a setup which generates UV light at 266 nm. Frequency doubling of the Verdi laser (532 nm) is enhanced by placing BBO crystal inside the enhancement cavity. The green arrow shows the optical path. and the blue arrow shows the 266 nm laser.

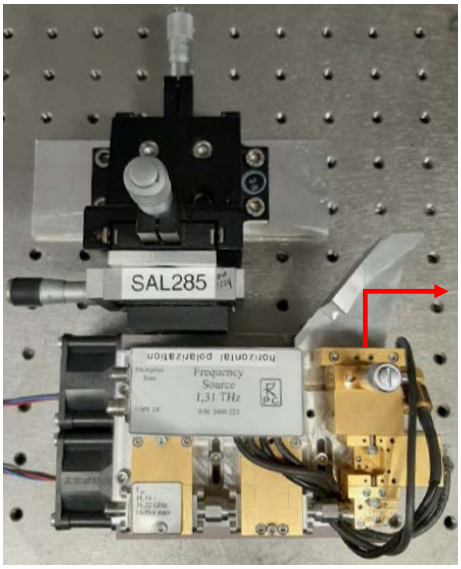

Figure A.6. THz source used for high precision rotational spectroscopy of HD^+ [76].

Acknowledgments

I would like first to thank my supervisor, Prof. Stephan Schiller, for allowing me to work on this rewarding project. It is through his vision and effort that this project reached the state that it is currently at. He has been generous with his willingness to discuss results, and advice on the path forward. I am grateful for the opportunity to learn from him.

I am honored to present results of a measurement which has been under development for almost two decades, benefiting from the dedication of many who worked on this project before me.

I am thankful to Dr. Alexander Nevsky for walking me through the laboratory work at early stage of my carrier, and continued helping and advising me during this work.

I have truly enjoyed working with many graduate students and postdocs throughout my carrier. I am thankful to Michael G. Hansen for valuable help with the project. Dr. Gouri Shankar Giri and Dr. Florin L. Constantin were great help in doing long and complicated experiments. I enjoyed discussing the results and plans for the next steps of experiment with them. I acknowledge all of my colleagues: Christian Wellers, Ivan Kortunov, Prof. Kenneth R. Brown (Duke University), Chang Jian Kwong, Evangelos Magoulakis, René Oswald, Eugen Wiens, Dr. Wu Bian, Magnus Schenkel, Viktor Vogt, Claire-Denise Frese, Mysore Srinivas Pramod, and Stefano Origlia. Each has helped this work in his or her own way, whether helping with laboratory works and duties, letting me borrow laboratory tools, or simply discussing physics.

Developing and maintaining a complicated experimental apparatus became possible with great help of our creative technicians: Ulrich Rosowski, Dmitri Iwaschko, Rita Gusek, and Peter Dutkiewicz.

I am thankful to Beate Rödding for handling the administrative tasks.

I had a pleasure having three undergraduates around the laboratory, who contributed in development of part of the setup: Maxim Lipkin, Jana Scheuer, and Mario Meltzer.

I am grateful to Prof. Michael Schmitt and Prof. Stephan Schlemmer (Universität zu Köln) for careful reviewing of this dissertation.

Of course, I greatly appreciate my parents and family. Without their love and support I could not have made it this far.

My special thanks to my wife, Dr. Soudeh Jahanshahi, for providing the inspiration and being particularly supportive and patient.

Bibliography

[1] Aznabayev, D.T., Bekbaev, A.K., and Korobov, V.I., *Leading-order relativistic corrections to the rovibrational spectrum of* $H_2{}^+$ *and* HD^+ *molecular ions*, Phys. Rev. A **99**, 012501 (2019), doi: 10.1103/PhysRevA.99.012501.

[2] Biesheuvel, J. et al., *Probing QED and fundamental constants through laser spectroscopy of vibrational transitions in* HD^+, Nat. Commun. **7**, 10385 (2016), doi: 10.1038/ncomms10385.

[3] Patra, S. et al., *Proton–electron mass ratio from* HD^+ *revisited*, J. Phys. B **51**, 2, 024003 (2017), doi: 10.1088/1361-6455/aa9b92.

[4] Tanabashi, M. et al., *Review of particle physics: Particle Data Group*, Phys. Rev. D **98**, 030001 (2018), doi: 10.1103/PhysRevD.98.030001.

[5] Andreev, V. et al., *Improved limit on the electric dipole moment of the electron*, Nature **562**, 355–360 (2018), doi: 10.1038/s41586-018-0599-8.

[6] Uzan, J.P., *Varying constants, gravitation and cosmology*, Living Rev. Relativ. **14**, 2 (2011), doi: 10.12942/lrr-2011-2.

[7] Uzan, J.P., *The stability of fundamental constants*, C. R. Phys. **16**, 576–585 (2015), doi: 10.1016/j.crhy.2015.03.007.

[8] Mohr, P.J., Newell, D.B., and Taylor, B.N., *CODATA recommended values of the fundamental physical constants: 2014*, Rev. Mod. Phys. **88**, 035009 (2016), doi: 10.1103/RevModPhys.88.035009.

[9] Stock, M. et al., *The revision of the SI—the result of three decades of progress in metrology*, Metrologia **56**, 022001 (2019), doi: 10.1088/1681-7575/ab0013.

[10] Weyers, S. et al., *Advances in the accuracy, stability, and reliability of the PTB primary fountain clocks*, Metrologia **55**, 789–805 (2018), doi: 10.1088/1681-7575/aae008.

[11] Lamb, W.E. and Retherford, R.C., *Fine structure of the hydrogen atom by a microwave method*, Phys. Rev. **72**, 241–243 (1947), doi: 10.1103/PhysRev.72.241.

[12] Nafe, J., Nelson, E., and Rabi, I., *The hyperfine structure of atomic hydrogen and deuterium*, Phys. Rev. **71**, 914–915 (1947), doi: 10.1103/PhysRev.71.914.

[13] Brewer, S.M. et al., $^{27}Al^{+}$ *quantum-logic clock with a systematic uncertainty below* 10^{-18}, Phys. Rev. Lett. **123**, 033201 (2019), doi: 10.1103/PhysRevLett.123.033201.

[14] Godun, R.M. et al., *Frequency ratio of two optical clock transitions in* $^{171}Yb^{+}$ *and constraints on the time variation of fundamental constants*, Phys. Rev. Lett. **113**, 210801 (2014), doi: 10.1103/PhysRevLett.113.210801.

[15] Huntemann, N. et al., *Improved limit on a temporal variation of* m_p/m_e *from comparisons of* Yb^{+} *and Cs atomic clocks*, Phys. Rev. Lett. **113**, 210802 (2014), doi: 10.1103/PhysRevLett.113.210802.

[16] Cairncross, W. and Ye, J., *Atoms and molecules in the search for time-reversal symmetry violation*, Nat. Rev. Phys. **1**, 510–521 (2019), doi: 10.1038/s42254-019-0080-0.

[17] Wood, C.S. et al., *Measurement of parity nonconservation and an anapole moment in cesium*, Science **275**, 1759–1763 (1997), doi: 10.1126/science.275.5307.1759.

[18] Feynman, R., *Quantum Electrodynamics*, Frontiers in Physics, Taylor & Francis Group, LLC (1998), ISBN 9780201360752.

[19] Karshenboim, S.G., *Precision physics of simple atoms: QED tests, nuclear structure and fundamental constants*, Phys. Rep. **422**, 1–63 (2005), doi: 10.1016/j.physrep.2005.08.008.

[20] Arrington, J. and Sick, I., *Evaluation of the proton charge radius from electron-proton scattering*, J. Phys. Chem. Ref. Data **44**, 031204 (2015), doi: 10.1063/1.4921430.

[21] Pohl, R. et al., *The size of the proton*, Nature **466**, 213–216 (2010), doi: 10.1038/nature09250.

[22] Beyer, A. et al., *The Rydberg constant and proton size from atomic hydrogen*, Science **358**, 79–85 (2017), doi: 10.1126/science.aah6677.

[23] Bezginov, N. et al., *A measurement of the atomic hydrogen lamb shift and the proton charge radius*, Science **365**, 1007–1012 (2019), doi: 10.1126/science.aau7807.

[24] Fleurbaey, H. et al., *New measurement of the* $1s-3s$ *transition frequency of hydrogen: Contribution to the proton charge radius puzzle*, Phys. Rev. Lett. **120**, 183001 (2018), doi: 10.1103/PhysRevLett.120.183001.

[25] Schiller, S., Bakalov, D., and Korobov, V.I., *Simplest molecules as candidates for precise optical clocks*, Phys. Rev. Lett. **113**, 023004 (2014), doi: 10.1103/PhysRevLett.113.023004.

[26] Kunz, J., *On Bohr's atom and magnetism*, Phys. Rev. **12**, 59–69 (1918), doi: 10.1103/PhysRev.12.59.

[27] Pauli jr, W., *Über das Modell des Wasserstoffmolekülions*, Ann. Phys. **373**, 177–240 (1922), doi: 10.1002/andp.19223731102.

[28] Burrau, Ø., *Berechnung des Energiewertes des Wasserstoffmolekel-ions* H_2^+ *im Normalzustand*, Naturwissenschaften **15**, 16–17 (1927), doi: 10.1007/BF01504875.

[29] Born, M. and Oppenheimer, R., *Zur Quantentheorie der Molekeln*, Ann. Phys. **389**, 457–484 (1927), doi: 10.1002/andp.19273892002.

[30] Jaffé, G., *Zur Theorie des Wasserstoffmolekülions*, Z. Phys. **87**, 535–544 (1934), doi: 10.1007/BF01333263.

[31] Baber, W.G. and Hassé, H.R., *The two centre problem in wave mechanics*, Math. Proc. Camb. Phil. Soc. **31**, 564–581 (1935), doi: 10.1017/S0305004100013566.

[32] Born, M. and Huang, K., *Dynamical Theory of Crystal Lattices*, Oxford classic texts in the physical sciences, Clarendon Press (1988), ISBN 9780198503699.

[33] Hunter, G., Yau, A.W., and Pritchard, H.O., *Rotation-vibration level energies of the hydrogen and deuterium molecule-ions*, Atom. Data Nucl. Data **14**, 11–20 (1974), doi: 10.1016/S0092-640X(74)80027-6.

[34] Moss, R. and Sadler, I., *Transformed hamiltonian theory for* HD^+, Mol. Phys. **66**, 591–603 (1989), doi: 10.1080/00268978900100351.

[35] Hylleraas, E.A., *Über die Elektronenterme des Wasserstoffmoleküls*, Z. Phys. **71**, 739–763 (1931), doi: 10.1007/BF01344443.

[36] Bishop, D.M. and Cheung, L.M., *Calculation of transition frequencies for* H_2^+ *and its isotopes to spectroscopic accuracy*, Phys. Rev. A **16**, 640–645 (1977), doi: 10.1103/PhysRevA.16.640.

[37] Korobov, V.I., *Coulomb three-body bound-state problem: Variational calculations of nonrelativistic energies*, Phys. Rev. A **61**, 064503 (2000), doi: 10.1103/PhysRevA.61.064503.

[38] Schiller, S., *Private communication*.

[39] Hunter, G. and Pritchard, H.O., *Born-Oppenheimer separation for three-particle systems. III. Applications*, J. Chem. Phys. **46**, 2153–2158 (1967), doi: 10.1063/1.1841017.

[40] Moss, R. and Sadler, I., *Variational calculations for high J, low v levels of* HD^+, Mol. Phys. **68**, 1015–1031 (1989), doi: 10.1080/00268978900102711.

[41] Balint-Kurti, G.G. et al., *Calculations of vibration-rotation energy levels of* HD^+, Phys. Rev. A **41**, 4913–4921 (1990), doi: 10.1103/PhysRevA.41.4913.

[42] Moss, R., *Non-adiabatic effects on properties of the hydrogen molecular cation and its isotopomers*, Mol. Phys. **97**, 3–9 (1999), doi: 10.1080/00268979909482804.

[43] Schiller, S. and Korobov, V., *Tests of time independence of the electron and nuclear masses with ultracold molecules*, Phys. Rev. A **71**, 032505 (2005), doi: 10.1103/PhysRevA.71.032505.

[44] Korobov, V.I., *Leading-order relativistic and radiative corrections to the rovibrational spectrum of* H_2^+ *and* HD^+ *molecular ions*, Phys. Rev. A **74**, 052506 (2006), doi: 10.1103/PhysRevA.74.052506.

[45] Karr, J.P. and Hilico, L., *High accuracy results for the energy levels of the molecular ions* H_2^+, D_2^+ *and* HD^+, *up to* $J = 2$, J. Phys. B-At. Mol. Opt. **39**, 2095–2105 (2006), doi: 10.1088/0953-4075/39/8/024.

[46] Tang, L.Y. et al., *High-precision nonadiabatic calculations of dynamic polarizabilities and hyperpolarizabilities for low-lying vibrational-rotational states of hydrogen molecular ions*, Phys. Rev. A **90**, 012524 (2014), doi: 10.1103/PhysRevA.90.012524.

[47] Moss, R., *Calculations for vibration-rotation levels of* HD^+, *in particular for high* N, Mol. Phys. **78**, 371–405 (1993), doi: 10.1080/00268979300100291.

[48] Caswell, W. and Lepage, G., *Effective lagrangians for bound state problems in QED, QCD, and other field theories*, Phys. Lett. B **167**, 437–442 (1986), doi: 10.1016/0370-2693(86)91297-9.

[49] Korobov, V.I., *Relativistic corrections of* $m\alpha^6$ *order to the rovibrational spectrum of* $H_2{}^+$ *and* HD^+ *molecular ions*, Phys. Rev. A **77**, 022509 (2008), doi: 10.1103/PhysRevA.77.022509.

[50] Bakalov, D., Korobov, V.I., and Schiller, S., *High-precision calculation of the hyperfine structure of the* HD^+ *ion*, Phys. Rev. Lett. **97**, 243001 (2006), doi: 10.1103/PhysRevLett.97.243001.

[51] Gan, H.C.J. et al., *Oscillating-magnetic-field effects in high-precision metrology*, Phys. Rev. A **98**, 032514 (2018), doi: 10.1103/PhysRevA.98.032514.

[52] Bakalov, D., Korobov, V.I., and Schiller, S., *Magnetic field effects in the transitions of the* HD^+ *molecular ion and precision spectroscopy*, J. Phys. B-At. Mol. Opt. **44**, 025003 (2011), doi: 10.1088/0953-4075/44/2/025003.

[53] Schiller, S. et al., *Static and dynamic polarizability and the Stark and blackbody-radiation frequency shifts of the molecular hydrogen ions* $H_2{}^+$, HD^+, *and* $D_2{}^+$, Phys. Rev. A **89**, 052521 (2014), doi: 10.1103/PhysRevA.89.052521.

[54] Birge, R.T., *The quantum levels and resulting constants of the hydrogen molecule*, Proc. Natl. Acad. Sci. **14**, 12–19 (1927), doi: 10.1073/pnas.14.1.12.

[55] Richardson, C.B., Jefferts, K.B., and Dehmelt, H.G., *Alignment of the* H_2^+ *molecular ion by selective photodissociation. II. experiments on the radio-frequency spectrum*, Phys. Rev. **165**, 80–87 (1968), doi: 10.1103/PhysRev.165.80.

[56] Jefferts, K.B., *Hyperfine structure in the molecular ion* H_2^+, Phys. Rev. Lett. **23**, 1476–1478 (1969), doi: 10.1103/PhysRevLett.23.1476.

[57] Wing, W.H. et al., *Observation of the infrared spectrum of the hydrogen molecular ion* HD^+, Phys. Rev. Lett. **36**, 1488–1491 (1976), doi: 10.1103/PhysRevLett.36.1488.

[58] Roth, B. et al., *Rovibrational spectroscopy of trapped molecular hydrogen ions at millikelvin temperatures*, Phys. Rev. A **74**, 040501 (2006), doi: 10.1103/PhysRevA.74.040501.

[59] Dicke, R.H., *The effect of collisions upon the Doppler width of spectral lines*, Phys. Rev. **89**, 472–473 (1953), doi: 10.1103/PhysRev.89.472.

[60] Jefferts, S.R. et al., *Coaxial-resonator-driven rf (Paul) trap for strong confinement*, Phys. Rev. A **51**, 3112–3116 (1995), doi: 10.1103/PhysRevA.51.3112.

[61] Peik, E. et al., *Sideband cooling of ions in radio-frequency traps*, Phys. Rev. A **60**, 439–449 (1999), doi: 10.1103/PhysRevA.60.439.

[62] Larson, D.J. et al., *Sympathetic cooling of trapped ions: A laser-cooled two-species nonneutral ion plasma*, Phys. Rev. Lett. **57**, 70–73 (1986), doi: 10.1103/PhysRevLett.57.70.

[63] Wolf, F. et al., *Non-destructive state detection for quantum logic spectroscopy of molecular ions*, Nature **530**, 457–460 (2016), doi: 10.1038/nature16513.

[64] Chou, C.W. et al., *Preparation and coherent manipulation of pure quantum states of a single molecular ion*, Nature **545**, 203–207 (2017), doi: 10.1038/nature22338.

[65] Fröhlich, U., Roth, B., and Schiller, S., *Ellipsoidal Coulomb crystals in a linear radio-frequency trap*, Phys. Plasmas **12**, 073506 (2005), doi: 10.1063/1.1976605.

[66] Blythe, P. et al., *Production of ultracold trapped molecular hydrogen ions*, Phys. Rev. Lett. **95**, 183002 (2005), doi: 10.1103/PhysRevLett.95.183002.

[67] Vasilyev, S. et al., *Compact all-solid-state continuous-wave single-frequency UV source with frequency stabilization for laser cooling of* Be^+ *ions*, Appl. Phys. B **103**, 27–33 (2011), doi: 10.1007/s00340-011-4435-1.

[68] Zhang, C.B. et al., *Molecular-dynamics simulations of cold single-species and multispecies ion ensembles in a linear Paul trap*, Phys. Rev. A **76**, 012719 (2007), doi: 10.1103/PhysRevA.76.012719.

[69] Fröhlich, U., *Coulomb crystal studies, sympathetic cooling, and mass spectrometry using laser-cooled* Be^+ *ions*, Ph.D. thesis, Heinrich-Heine-Universität Düsseldorf (2008).

[70] Schnitzler, H., *Development of an experiment for trapping, cooling, and spectroscopy of molecular hydrogen ions*, Ph.D. thesis, Universität Konstanz (2001).

[71] Drever, R.W.P. et al., *Laser phase and frequency stabilization using an optical resonator*, Appl. Phys. B **31**, 97–105 (1983), doi: 10.1007/BF00702605.

[72] Scheuer, J., *Computergesteuerte Reinigung eines gespeicherten Beryllium-Ionenclusters*, Bachelor thesis (2017).

[73] Zhang, C., *Production and Sympathetic Cooling of Complex Molecular Ions*, Ph.D. thesis, Heinrich-Heine-Universität Düsseldorf (2008).

[74] Korobov, V.I. et al., *Laser-stimulated electric quadrupole transitions in the molecular hydrogen ion* H_2^+, Phys. Rev. A **97**, 032505 (2018), doi: 10.1103/PhysRevA.97.032505.

[75] Germann, M., Tong, X., and Willitsch, S., *Observation of electric-dipole-forbidden infrared transitions in cold molecular ions*, Nat. Phys. **10**, 820–824 (2014), doi: 10.1038/nphys3085.

[76] Schiller, S. et al., *Ultra-narrow-linewidth continuous-wave THz sources based on multiplier chains*, Appl. Phys. B **95**, 55–61 (2009), doi: 10.1007/s00340-008-3279-9.